Catching Some Sun

the interaction between
comets and the solar wind

RuG | Dennis Bodewits | 2003

Cover Background:
Reproduction from ancient Chinese astrological handbook, ca. 168 AD. Each of the drawings represents a type of comet and is linked to a specific omen.

Cover Center:
‘Adorazioni di Magi’ - Giotto di Bondone, ca. 1305. Inspired by the apparition of comet Halley in October 1301, Giotto painted a fresco with comet Halley as the star of Bethlehem. ESA named the probe that would visit comet Halley after him.

Catching Some Sun

the interaction between comets and the solar wind

Master Thesis
Dennis Bodewits

Supervisors:

Ronnie Hoekstra	KVI Atomic Physics
Xander Tielens	Kapteyn Institute

May 2003

Dramatis Personae

- **The Sun** Center of the Solar System.
- **Halley** First periodic comet discovered. The comet returns every 75-80 years and ancient observations of comet Halley are known back to 240 B.C. In 1986, six different spacecraft flew though its coma and most of the current knowledge on comets comes from these missions. In this report, Halley is therefore used as the standard comet.
- **Hale-Bopp** Comet C/1995 O1 (Hale-Bopp) is one of the brightest comets of the last two centuries. It is a long period comet from the Oort cloud and its next appearance will be in about 2380 years. The comet reached its closest point to the Sun (perihelion) on April 1, 1997.
- **Hyakutake** Comet C/1996 B2 (Hyakutake) is often referred to as 'The Comet of the 20th Century'. Although it was not as big as comet Hale-Bopp, it came much closer to Earth: at March 25, it was only 0.1 A.U. from Earth, or approximately fifty times the distance between the Earth and the Moon.
- **McNaught-Hartley**(C/1999 T1) is an Oort-cloud comet with a orbital period of approximately 580,000 years. The comet reached its perihelion in December, 2000.
- **Encke**. At the end of this year, comet 2P/Encke will make its 59th predicted return. Its orbit is quite stable, and with a period of 3.3 years apparitions repeat on a 10-year cycle.
- **C/Linear S4** was a modestly bright comet that was disintegrated in the summer of 2000.
- **Alpha particles, highly charged ions, photons and various molecules and atoms**

Contents

Chapter 1

Introduction

In 1996, bright X-Ray emission was discovered from comet Hyakutake [1]. This was unexpected: comets were known to be cold objects while X-Ray emission requires high energy processes. In the following years, it became clear that X-Ray emission is a common property of comets and it was first suggested by Cravens [2] that this emission was due to interaction between comets and the solar wind, or to be more precise, charge exchange between cometary neutral molecules and highly charged ions from the solar wind.

Since these early observations, the field of X-Ray astronomy went to nothing less than a revolution culminating in the 2002 Nobelprize for X-Ray pioneer Giaconni. It was his work that led to the launch of the Chandra and XMM X-Ray telescopes (1999) and several new X-Ray observatories have already been planned for the next years.

With this new generation of high-energy observatories, the observational sensitivity and resolution increased enormously. In the case of comets, this lead to the observation of line spectra allowing for the identification of various solar wind species [3, 4]. Even more, several other solar system objects were discovered to radiate in X-Ray, such as Mars, Venus and the Jovian system [5, 6, 7]. Not all of these objects radiate because of charge exchange, but it is clear that charge exchange by solar wind ions is one of the most important sources of X-Ray radiation in the solar system.

The interaction between comets and the solar wind is a very complex problem. Not only charge exchange processes are involved, but also magneto-hydrodynamics and a number of physical and/or chemical effects play a critical role into the cometary environment. A small insight in the complexity of this system was given by the different space probes that crossed with comet Halley in 1986.

In this thesis, experimental data from various charge exchange reactions is used to probe the interaction between comets and the solar wind. It is shown

that cometary X-Ray and Far UV spectra contain a wealth of information on both the solar wind and the cometary environment it reacts with.
Once the cometary emission mechanism is understood well, it will be possible to use comets to probe the solar wind over a large range of distances that is not easily covered by man-made space probes and to extend our knowledge of space weather.

1.1 Outline

The outline of this work is the following:

- Chapter 2 contains a general introduction to comets, solar wind and their interaction;
- In Chapter 3 a general introduction is given to the process of charge exchange. The experimental technique that is used at the KVI to measure velocity dependent state selective cross sections is presented, together with results obtained with this set up;
- In Chapter 4 a model is presented that describes how the solar wind helium ions are neutralized by charge exchange with cometary neutrals. This model is compared with different observations.
- In Chapter 5, the heavy ion content of the solar wind is considered. A model is presented for the X-Ray spectra emission following capture into the excited states of the various ions and the results of this model are compared with recent observations.
- In Chapter 6, the conclusions of this work are summarized and combined with suggestions for future experiments and observations.

Chapter 2

Comets and the Solar Wind

A comet is essentially a cold, dusty ice ball that moves through the solar system in a parabolic or elliptical orbit (Figure 2.1). When a comet approaches the Sun at a distance of approximately 5 A.U.[1] (Jupiter's orbit), it will slowly change from a cold dusty snowball into the fiery objects we know. Heated by the Sun, the layers just beneath the surface of the cometary nucleus will start to sublimate and a cloud of mainly gas and dust will start to form. This cloud is called the coma.

When the comet is close enough to the Sun, the characteristic tails will form. Typically there are two tails; one consists of dust, the other of ions (Figure 2.2). When dust is released from the nuclear surface, it will be dragged along with the expanding gas. Once the particles reach the tail region, their behaviour is determined by solar gravity and radiation pressure. The dust tail is therefore a strongly curved tail in the direction opposite to the orbital motion of the comet. The second tail is the ionic tail. Its properties have long been a problem for physics because radiation pressure failed to explain the observed acceleration of ionized molecules in cometary tails. The research of processes that drive the ionic tail led to the discovery of the solar wind in the 1950s. Because of its dynamics, the ionic tail always points away from the sun.

2.1 Comets and the Sun

The structure of a comet is determined by the interaction of the cometary gas with light and particles from the Sun. This work focusses on their interaction with the coma. Within the coma, a distinction can be made between dif-

---

[1] Astronomical Units; 1 A.U. corresponds to the average distance between the Earth and the Sun; $149.6 \cdot 10^6$ km

Figure 2.1: Comet Borrelly's nucleus, as seen with the probe Deep Space 1 in 2001. The nucleus has a size of circa 8 km.

Figure 2.2: Tails of comet Hale-Bopp: the ionic tail glows blue due to fluoresence of CO^+ and OH^+, the dust tail appears white due to reflection of sunlight.

ferent regions, each of which is dominated by different processes. Although individual comets show great differences, their global structure is more or less the same. This structure is summarized in Figure 2.4. The structure of comets can be considered to scale with the amount of gas that streams out of the nucleus, the gas production rate Q. Because gas is produced by heating of the cometary surface by sunlight, Q will be strongly dependent on the distance between the comet and the Sun. At a heliocentric distance of 1 A.U., typical gas production values are in the order of 1000-10000 kg s^{-1} or . As the gas production is related to the amount of Sun light received, the sunward side of the comet will produce more gas than the backside. The nucleus will therefore start to rotate with a period of approximately a day.

The chemical composition of the coma differs greatly from the composition of the nucleus and both the density and the composition depend strongly on the distance to the sun. The temperature at the surface will rapidly increase when the comet approaches the Sun. Species with relatively low sublimation temperature such as CO, CO_2 and volatile hydrocarbons will dominate the coma when the comet is still far away from the Sun [8]. At a distance of typically 3 A.U. the temperature rises enough to start the sublimation of water ice, which leads to a strong increase of the brightness of the comet.

The mass of the comet is much too small to bind the out flowing gas gravitationally; the size of the coma is therefore only limited by the outflow velocity of the gas and the rate at which it is destroyed by solar light and particles. To illustrate this, we will consider a comet at a distance of 1 A.U. of the Sun. The gas streaming out of the nucleus will be water with 5% – 20% CO and 5% CO_2; a fraction up to some 5% may consist of molecules such as CH_4, N_2, NH_3 [9]. Molecules that are produced directly by evaporation from the nucleus are called parent molecules, in contrast to daughter molecules which are formed from the parent molecules by all sorts of physical and/or chemical reactions.

The density in the coma can be approximated by a $1/r^2$ decrement, combined with an exponential term that describes additional decrement of the number density due to photo dissociation processes:

$$\rho_{comet} = \frac{Q_{comet}}{4\pi R_{comet}^2 v_{gas}} \cdot \exp\left[-R_{comet}/h\right] \tag{2.1}$$

Here Q is the gas production rate (molecules s^{-1}), R_{comet} is the extent of the coma (km), v_{gas} is the velocity (km/s) of the escaping gas and h is the scale length of the destruction of the molecules in kilometers (the scale length is defined as the distance at which the original population is reduced by a factor 1/e).

Table 2.1 summarizes the scale lengths of the most important cometary species when exposed to sunlight at 1 A.U. The scale lengths are calculated using photo dissociation and photo ionization rates given by Huebner *et al.* [10] and by assuming that all molecules have an outflow velocity of 1 km/s. Water, carbon monoxide and carbon dioxide are parent molecules, while OH, O and H are mainly produced by dissociation of water molecules. From the table it is readily seen that water and hydroxyl molecules are easier dissociated than ionized. For carbon monoxide on the other hand, the dissociation scale and ionization scale are approximately the same. The CO molecules

Species	Dissociation Scale (10^4 km)	Ionization Scale (10^4 km)
H_2O	8.58	302
OH	>5.0	408
CO	317	263
CO_2	108	153
H	-	662
C	-	9.62
O	-	198

Table 2.1: Photo ionization and dissociation scale length of different molecules at a heliocentric distance of 1 A.U. from Huebner *et al.* [10]

will thus have longer lifetimes and travel further than the water and hydroxyl molecules when exposed to sunlight [10, 11, 12, 13]. This effect is shown in more detail in Figure (2.3), which is taken from Ip *et al.* [13]. In this figure, the composition of a the coma of a Halley-like comet that interacts with both sunlight and solar wind has been modelled. [2]

The water population can be seen to decrease very rapidly due to the short scale length of water molecules. In the outer regions of the coma, all the water is consumed by a variety of destructive processes and the gas consists mainly of O, H, CO and a minor fraction of CO_2 and C.

2.2 Structure of the Coma

The coma is divided in several regions which differ greatly in their physical characteristics. These regions are formed by the interaction of comets with the Sun, either with light or with the solar wind. The solar wind (which will be treated in more detail in Section 2.3) is essentially a highly supersonic, collisionless plasma that carries a magnetic field within. When solar wind ions hit the outskirts of the cometary coma, the solar wind ions will pick up cometary ions with its magnetic field. Conservation of momentum requires that the addition of mass in the form of heavy cometary molecules leads to a deceleration of the solar wind velocity. From the geometry of the pick up process, it follows that near the comet-solar wind axis the pick up process occurs the most. The wind is therefore more strongly decelerated around this axis than at larger distances of this axis and the net effect is that the magnetic field lines, rigidly carried within the solar wind plasma are folded around the comet [16].

The deceleration by the pick up process causes the solar wind flow to make a transition from supersonic to subsonic, creating the outer bow shock. This typically occurs at about a million kilometers from the comet's nucleus. The bow shock is a very weak collisionless shock. The sudden deceleration compresses the solar wind while increasing the particle density and the electron temperature. Magnetohydrodynamic models therefore predict that in the shock region, the ionization of the cometary neutrals is dominated by electron impact and proton-molecule charge exchange [17].

The solar wind ions continue their way through the bow shock and the outer coma while its bulk velocity decreases further by the ongoing pick up process. A transition occurs between the collisionless, mass loaded solar wind plasma flow and a region dominated by collisions between the solar wind flow and

---

[2] Note that in this model, a rather high abundance of CO (15%) and CO_2 (15%) which was not confirmed by observations.

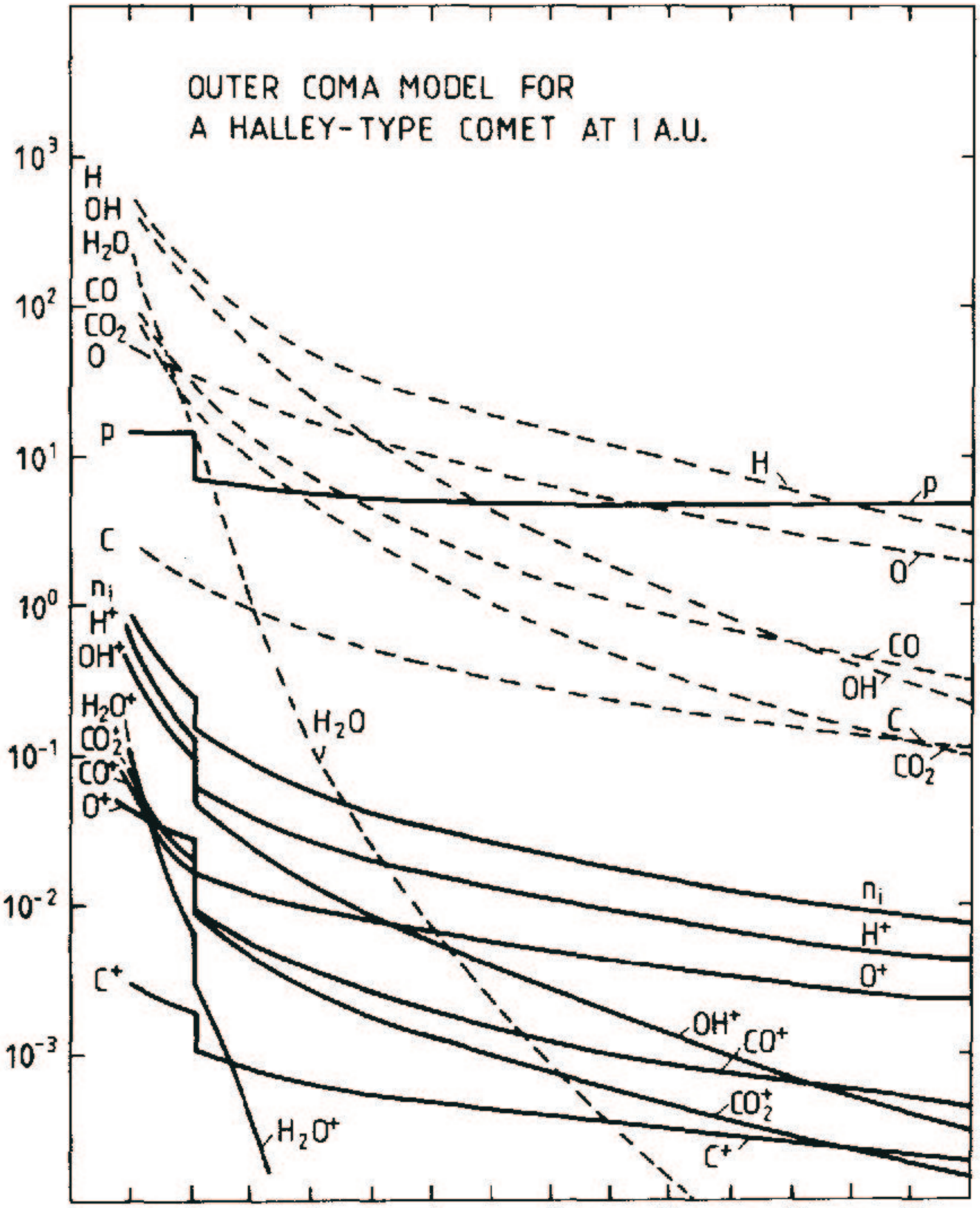

Figure 2.3: Abundance profile in the outer regions of the coma for a Halley-type comet with a gas production rate of $Q = 10^{30}$ s^{-1} at a heliocentric distance of 1 A.U., taken from Ip *et al.* [14].

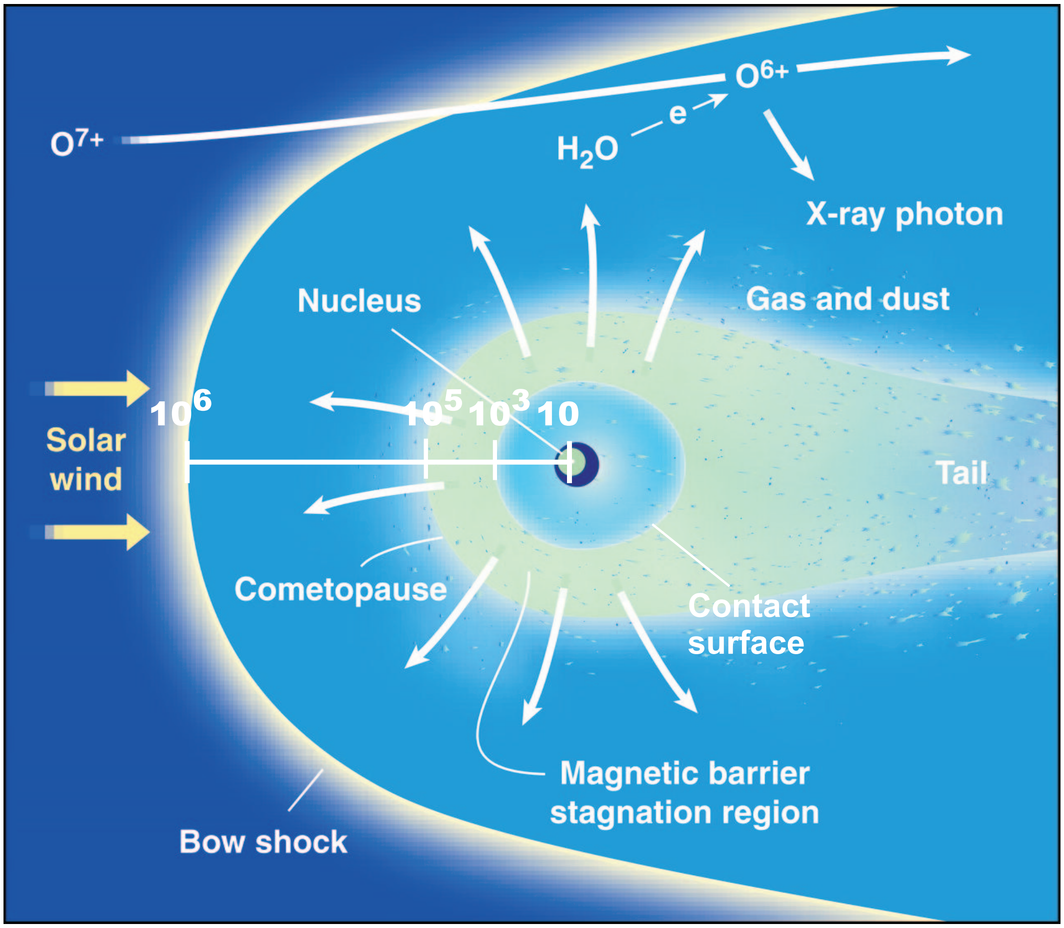

Figure 2.4: Schematic figure of the interaction between cometary gas and the solar wind (not to scale). To indicate the typical extent of a comet, distances from the cometary nucleus are drawn in in kilometers. The layer in between the cometopause and the nucleus is the contact surface. Picture adapted from Cravens [15].

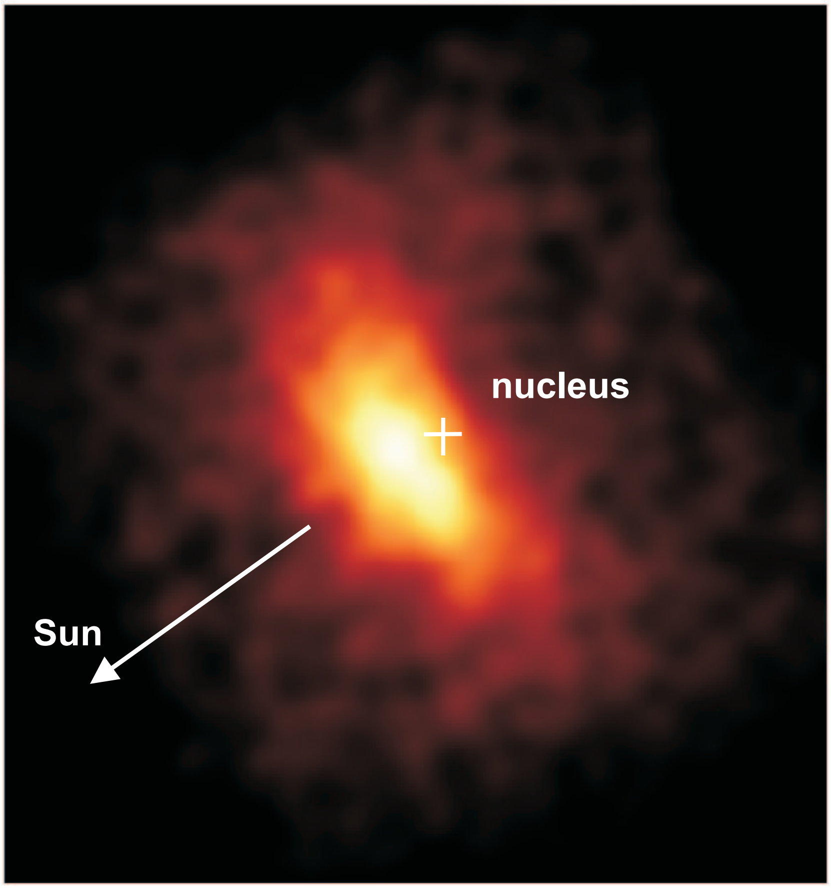

Figure 2.5: Chandra image of comet Linear S4 at 0.2-0.8 keV. The crescent shape is symmetric around the comet-Sun axis. Image adapted from Lisse *et al*[3].

the out flowing cometary gas. This jump was measured in comet Halley at a distance of some 10^5 kilometers from the nucleus, both in the form of a change in chemical composition from mainly solar wind protons to mainly ionized cometary molecules (using VEGA, [18]) and in the form of an abrupt increase in the ratio He^+/He^{2+} (using Giotto, [19]). This jump region is often referred to as the *cometopause*. Ionization here is dominated by charge exchange by protons and heavy ions [20].

Once the cometopause-barrier is crossed, ions are in the pile up region. In this region, the cometary density increases rapidly due to cometary molecules which are mostly ionized by electron impact and photo-ionization. In this region, the X-Ray and Far UV emission is formed. Observations show a clear hemispherical shape, Figure 2.5. When all the solar wind ions are neutralized, no more charge exchange reactions will take place and no more photons are

Figure 2.6: The corona, source of the solar wind, has traditionally been observed during solar eclipse, when it is revealed by the Moon.

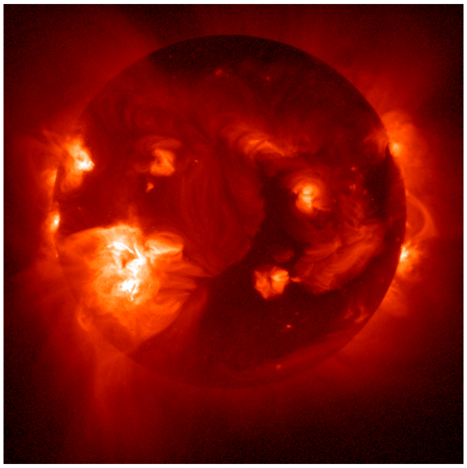

Figure 2.7: X-Ray observations of the Sun by the Japanese Yohkoh-spacecraft. Coronal holes can clearly be seen as large, dark spots.

emitted. Because the cometary density drops with the distance from the nucleus as $1/r^2$, this depletion occurs first along the comet-Sun axis.

Finally, 1000 km away from the nucleus, the ions will find a barrier that they cannot cross. The pressure balance of the outwardly streaming gas and the flow of the solar wind and magnetic field give rise to the *contact surface* or magnetic cavity. The contact surface separates purely cometary plasmas from the solar wind plasma. Gas properties within the contact surface are collision dominated due to high densities [21]. The resulting thermal energy is too low to allow collisional ionization to be an important ionization factor so photo-ionization is by far the most important ionization process in the magnetic cavity.

The ions produced in the coma will be picked up by the solar wind plasma that streams around the contact surface. By the pick up process, the ions will be accelerated away from the Sun and therefore the ionic tail always points in the anti-solar direction. The tail easily exceeds 10^7 kilometers, has a width of some 10^5 kilometers and is highly structured with knots and clouds. It was the study of these structures that lead to the modern ideas concerning the solar wind.

2.3 Solar Wind

In the previous section it was mentioned that comets not only interact with sunlight, but also with a plasma streaming out of the Sun: the solar wind. The solar wind originates from coronal holes, large cells of unipolar magnetic fields on the Sun's surface. Coronal holes can be seen as large, dark spots when observing the Sun in the X-Ray spectral range (Figure 2.7). Their open field lines allow a continuous outflow of solar wind, accelerating solar wind particles away from the Sun. Especially near the Sun, the precise form of the plasma flow is extremely complicated because the magnetic field within the plasma is twisted into an Archimedean spiral. At a distance of a few solar radii, the solar wind can be considered to expand radially. Its density therefore approximately scales with $1/r^2$. At the distance of the Earth, typical densities are 5-10 protons cm^{-3}.

Solar wind properties are highly variable on a short time scale. The wind consists of an equal amount of protons and electrons, some 5% helium and a small fraction of heavy ions (oxygen, carbon, nitrogen, etc). Due to the high temperatures in the corona -over 10^6 K- all ions in the solar wind are highly ionized. Because the solar wind carries a magnetic field within and because of its low densities, the ions in the solar wind do not collide with each other and both the velocity and charge state composition remain nearly the same when the solar wind flows out into the solar system [16]. The solar wind velocities of heavy ions and protons are equal, which implies that heavy ions have more kinetic energy [22].

A rough distinction can be made, separating two types of solar wind: the *fast* solar wind with velocities around 1000 km/s from large, deep polar coronal holes and the *slow* solar wind with velocities up to 400 km/s, originating from smaller coronal holes which are within 20 degrees of the equator [23, 24]. The properties of these winds are summarized in Table 2.2. Each high- or low speed stream generally lasts for several days to two weeks, but many smaller scale fluctuations are affecting the precise properties of the solar wind. Spaceborn observations indicate that these two types of wind show clear differences in their elemental and charge state distribution [25, 26, 27, 28]. This effect is only partly understood but is often expressed in terms of freeze-in temperatures: because ionization rate constants are very electron-temperature

	Slow Wind	Fast Wind
Density (protons/cm^3)	5-8	8-12
Velocity (km/s)	200-400	500-1100

Table 2.2: Properties of the solar wind at 1 A.U.

Element	Fast	Slow	Element	Fast	Slow	Element	Fast	Slow
H^+	1550	1780	Mg $^{10+}$	0.029	0.098	S $^{10+}$	0.008	0.005
He^{2+}	68 ± 3	78 ± 4	Mg $^{9+}$	0.044	0.052	S $^{9+}$	0.027	0.016
C $^{6+}$	0.085	0.318	Mg $^{8+}$	0.028	0.041	S $^{8+}$	0.023	0.019
C $^{5+}$	0.440	0.210	Mg $^{7+}$	0.007	0.017	S $^{7+}$	0.005	0.006
N $^{7+}$	0.000	0.006	Mg $^{6+}$	0.003	0.009	S $^{6+}$	0.001	0.002
N $^{6+}$	0.011	0.058	Mg $^{5+}$	0.000	0.000	S $^{5+}$	0.000	0.000
N $^{5+}$	0.127	0.065	Mg $^{4+}$	0.000	0.000	Fe $^{13+}$	0.005	0.002
O $^{8+}$	0.000	0.070	Mg $^{3+}$	0.000	0.000	Fe $^{12+}$	0.017	0.007
O $^{7+}$	0.030	0.200	Si $^{10+}$	0.024	0.021	Fe $^{11+}$	0.025	0.023
O $^{6+}$	0.970	0.730	Si $^{9+}$	0.045	0.049	Fe $^{10+}$	0.025	0.031
O $^{5+}$	0.000	0.000	Si $^{8+}$	0.022	0.057	Fe $^{9+}$	0.015	0.041
Ne $^{8+}$	0.102	0.084	Si $^{7+}$	0.002	0.000	Fe $^{8+}$	0.005	0.034
Ne $^{7+}$	0.005	0.004	Si $^{6+}$	0.000	0.000	Fe $^{7+}$	0.001	0.007
Ne $^{6+}$	0.000	0.000	Si $^{5+}$	0.000	0.000			

Table 2.3: Heavy element abundances scaled to the normalized total oxygen abundance $\Sigma_q O^{q+}$. Composition observations from Ulysses spacecraft by [25]

dependent, freeze-in temperatures determined from the ratio between the abundances of two ion species give information on the electron temperature at the place of origin of the ions. Typical abundance-charge state distribution (as shown in Table 2.3) correspond to freeze-in temperatures of about 1.0 to 1.5 million degrees [23].

2.4 Cometary X-Ray radiation

In 1996, comet Hyakutake was observed in X-Ray. This was a big surprise for comets were always considered to be cold, dusty snowballs from which one would not expect X-ray emission, which is typically associated with high energy processes. The observations, done with the Röntgen X-Ray Satellite (ROSAT) show a crescent shaped emission region centered at some 18000 kilometers in front of the nucleus. The emission was symmetric with respect to the comet-Sun axis and its intensity was variable on a time scale of only one or two hours [1]. A more recent X-Ray image of comet Linear S4 is shown in Figure 2.5. Since the first observation of Hyakutake, almost 20 comets have been observed in X-Ray or FUV.

A number of theories has been developed to explain the observed cometary X-Ray emission [29, 15]. Any suggestion however, should account for its primary features: morphology, temporal variability and spectrum, which limited the range of possible explanations.

In the Far-Ultraviolet regime, several emission lines were identified using spectra of the (late) EUVE satellite. Detailed FUV spectra were acquired for comet Hale-Bopp and Hyakutake [30, 31].

It has only recently become possible to achieve an observational resolution in X-Ray that allows for the distinction between continuum- and line-emission spectra. Using the Chandra X-Ray Observatory, the presence of several lines in the spectrum of Linear S4 and McNaught-Hartley has been shown [3, 4]. It is to be expected that future comet observations using the X-ray Multi-Mirror Mission (XMM-Newton) will also provide high resolution X-Ray spectra [3]

The presence of multiple emission lines in the X-Ray and FUV spectra proves that charge exchange is the process that accounts for the observed spectra. The solar wind contains a minor fraction of highly ionized atoms. When these ions collide with the neutral cometary molecules, 'charge' in the form of an electron will be transferred from the molecules to the ions. The electron will typically be captured in an excited state and its relaxation results in the emission of one or several X-Ray photons. The charge exchange process will be discussed in more detail in the next chapters.

In order to understand the observed X-Ray spectra better, several models have been made that simulate the charge exchange emission of comets. These models are either *macroscopic* or *microscopic*. Macroscopic models [32, 33, 25] consider the comet as a detailed, physical entity and use simplified atomic physics. Their goal is to model the global morphological characteristics of the solar wind-coma interaction and derive the structure of the region as parameters of the flux and the physical properties of the coma. The interaction between a comet and the solar wind is simulated using magneto-hydrodynamic plasma models (MHD). The resulting models confirm the observations of a shell-shaped morphology in front of the nucleus, perpendicular to the comet-sun axis.

Microscopic models [34, 35] on the other hand use detailed atomic processes but simplify the environment in which these processes occur. Their goal is to understand in detail the microscopic processes characterizing the interaction between solar wind atoms and coma species. X-Ray spectra are simulated by simulating the relaxation cascade through the atomic transition schemes. The result is a more reliable spectral prediction but comparison with observations have thus far been hard due to low observational resolutions.

---

[3] Comet Linear WM1 and C/2002 C1 Ikeya-Zhang have already been observed in X-Ray, but these results are not yet available

2.5 Probing the Interaction

Understanding the interaction between comets and the solar wind could provide us with a new tool to study space weather. Comets could be used to probe the solar wind up to a distance of 3 A.U. from the Sun [36], allowing for direct determination of solar wind properties such as its composition and flow structure.

Several attempts have been made to use the cometary X-Ray emission as a diagnostic tool. The general procedure in this is to use an existing interaction model and to fit the solar wind parameters in this model to the observed emission.

Regarding the interaction between comets and the solar wind, the most important feature of the solar wind is the interrelationship of composition and charge state distribution on the (initial) wind velocity (Section 2.3, [35, 25]). This dependency results in large differences between the expected emission spectra of the slow and fast solar wind, especially at photon energies above 450 eV. Amongst the brightest lines are some spin-forbidden transitions of oxygen and carbon; these forbidden lines might provide a unique diagnostic probe. This method has been applied on the comets Hale-Bopp, Levy and Encke, but its predictive qualities are limited by the resolution of available spectra. The spectrum of comet McNaught-Hartley has been used by Kharchenko *et al* to predict the relative abundance of highly ionized oxygen in the solar wind [37].

Although the existing microscopic models use detailed experimental atomic data, the velocity dependency of charge exchange processes is not taken into account. Laboratory measurements show that slower solar wind ions result in a 'harder' K-shell spectrum and Beiersdorfer [38] predicted that the ratio of high-to-low energy of the K-shell emission could be used as a probe to determine the velocity of solar wind ions interacting with molecules in the coma. This method has not been applied to any comet.

Chapter 3

The Process of Charge Exchange

Charge exchange is the process in which one or more electrons are transferred from one particle to another. The net reaction is:

$$A^{q+} + B \to A^{(q-s)+} + B^{s+} \tag{3.1}$$

Here A is an ion with charge q and B an initially neutral molecule or atom that is left with charge s after the capture process. The probability P that charge exchange occurs is generally expressed in terms of the cross section σ:

$$P = \int dr \sigma \rho(r) \tag{3.2}$$

where the integral is taken along the path of the ion through a gas with number density $\rho(r)$. The cross section has units of cm^2.

3.1 Classical Over the Barrier Model

The Classical Over-the-Barrier model (COB) is a simple approximation for collisions between ions and neutrals and allows for an estimate of the principal quantum number n into which the electron is captured [39]. Although the COB model is not related to the collision velocity, it generally only applies for energies in the range of some 100 eV/amu up to 10 keV/amu; exactly the range of solar wind velocities. According to the Classical Over-the-Barrier model, the reaction can be divided in several steps, which can be summarized with the following reaction scheme:

$$A^{q+} + B \to (AB)^{q+} \tag{3.3}$$

$$(AB)^{q+} \to A^{(q-1)+*} + B^{+*} + \Delta E \tag{3.4}$$

$$A^{(q-1)+*} + B^{+*} + \Delta E \to A^{(q-1)+} + B^{+} + \Delta E + h\nu \tag{3.5}$$

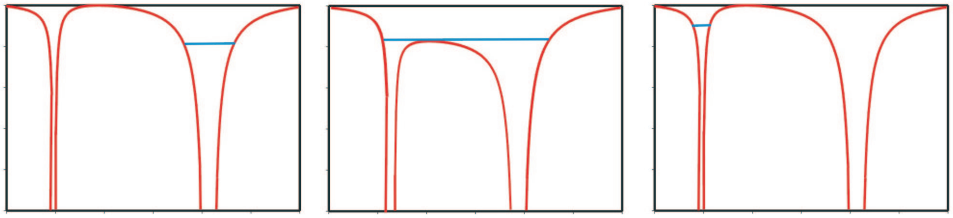

Figure 3.1: The Over the Barrier model for an ion colliding on a neutral target. On the left, the ion approaches the target. In the middle, the two particles are in a molecular state as the electron can move freely between the two nuclei and at the right, the ion leaves the target again with the captured electron. Picture provided by Steven Knoop.

where $(AB)^{q+}$ is the collision complex and the excited ions $A^{(q-1)+*}$ and B^+ decay radiatively to their ground states.

We will consider here the case in which an ion A captures one electron from a neutral particle B. The nuclei of the two particles are separated by an internuclear distance R. The molecule's least bound electron has a (negative) binding energy I_b and it can be considered being trapped in a potential well. Because the approaching ion also has such a potential well, it can be seen from Figure 3.1 that there is a 'barrier' in between the potential wells of the ion and the target molecule. The full potential experienced by an electron at a distance r of its parental nucleus is the sum of the potential of the ion and that of the target:

$$V(r) = -\frac{q}{|R-r|} - \frac{1}{|r|} \qquad \text{for} \qquad 0 < r < R \tag{3.6}$$

This barrier will reach its maximum value for exactly that r where the derivative of this equation equals zero:

$$\frac{dV(r)}{dr} = \frac{-q}{(R-r)^2} + \frac{1}{r^2} = 0 \tag{3.7}$$

Solving this equation, one finds an r_{max} at which the potential barrier obtains its maximum value V_{max}.

$$r_{max} = \frac{R}{\sqrt{q}+1} \tag{3.8}$$

$$V_{max} = -\frac{q}{R} - \frac{1+2\sqrt{q}}{R} = -\frac{(\sqrt{q}+1)^2}{R} \tag{3.9}$$

Meanwhile, the electron 'hides deeper' in the target's potential well; the approaching ion's Coulomb field causes a Stark shift to increase the electron's binding energy:

$$I_b(R) = I_b - \frac{q}{R} \tag{3.10}$$

where I_b is the absolute binding energy at infinite separation, the initial binding energy without Stark shift. Electron transfer can occur if the height of the potential barrier V_{max} drops below the shifted binding energy I_b:

$$-\frac{q}{R} - \frac{1+2\sqrt{q}}{R} = I_b - \frac{q}{R} \tag{3.11}$$

Solving this equation yields a critical distance R_{crit} between the two nuclei that has to be reached in order to allow for charge exchange.

$$R_{crit} = \frac{2\sqrt{q}+1}{-I_b} \tag{3.12}$$

From this distance, the cross section for the one electron capture process can be determined by assuming that if ions pass the neutral at a distance smaller than this critical distance R_{crit}, the electron is captured with unit probability. In this so called 'absorbing sphere approximation' the cross section is simply given by the geometrical cross section:

$$\sigma = \pi R_{crit}^2 = \pi \left(\frac{2\sqrt{q}+1}{I_b}\right)^2 \tag{3.13}$$

In practice, the classical Over-the-Barrier model tends to overestimate cross sections by a at least factor of two [40].
Once the two particles are (infinitely) separated again, the electron is left behind in the ion which was originally denoted as 'A'. For resonant charge exchange, the binding energy of the electron will again be the sum of the binding energy at R_{crit} and the Stark shift.

$$I_f = I_b(R_{crit}) + \frac{1}{R_{crit}} = I_b - \frac{q+1}{R_{crit}} \tag{3.14}$$

This approximation can be used to predict the state n that the electron will be captured in. This can be done by converting the binding energy I_f into a 'classical' energy level n_{cl} by the hydrogenic approximation

$$n_{cl} = \frac{Z}{\sqrt{|2I_f|}} \tag{3.15}$$

charge q →		1	2	3	4	5	6	7
Target	$\lvert I_b \rvert$ (eV)	Cross Section σ (10^{-15} cm^2)						
O,H	13.6	3.17	5.16	7.02	8.80	10.5	12.3	13.9
O_2	12.4	3.81	6.21	8.44	10.6	12.7	14.7	16.8
H_2O	12.6	3.69	6.01	8.17	10.3	12.3	14.3	16.2
CH_4	12.6	3.69	6.01	8.17	10.3	12.3	14.3	16.2
CO_2	13.8	3.09	5.03	6.85	8.59	10.3	12.0	13.6
CO	13.7	3.12	5.09	6.91	8.67	10.4	12.1	13.7
H_2	16.1	2.26	3.68	5.01	6.28	7.52	8.74	9.95

Target	$\lvert I_b \rvert$ (eV)	Classical principal quantum number n_{cl}						
O,H	13.6	0.8	1.5	2.3	3.1	3.9	4.6	5.4
O_2	12.4	0.8	1.6	2.4	3.2	4.1	4.9	5.7
H_2O	12.6	0.8	1.6	2.4	3.2	4.0	4.8	5.6
CH_4	12.6	0.8	1.6	2.4	3.2	4.0	4.8	5.6
CO_2	13.8	0.8	1.5	2.3	3.1	3.8	4.6	5.4
CO	13.7	0.8	1.5	2.3	3.1	3.8	4.6	5.4
H_2	16.1	0.7	1.4	2.1	2.8	3.6	4.3	5.0

Table 3.1: Classical Over-the-Barrier predictions for ions with different charges colliding on different target atoms and molecules.

For several cometary molecules, both the charge exchange cross section and the state in which the captured electron is left have been approximated this way, see Table 3.1. One will notice, that the values for n are not integers, for example, charge exchange between water and a twofold charged ion yields n of 1.6. This indicates that some electrons will be left in the ground state $n = 1$, others in the first excited state $n = 2$. Although the Classical Over-the-Barrier model does not give an exact distribution over these two states, the availability of states near the predicted binding energies may give information on the effectiveness of certain electron capture processes. It is of note that if the decimal fraction of n_{cl} is between 0.5 - 0.8 the actual n distribution strongly depends on the collision energy.

For a specific projectile, the cross section and the shell where the electron is captured in mainly depend on the binding energy of the target. Most molecules that are typical for a cometary environment have similar binding energies and therefore, it is safe to assume one generic molecule in our discussion of charge exchange in the coma.

3.2 Extended Over-the-Barrier Model

In the previous section, it was shown that the classical Over-the-Barrier model predicts the binding energies of captured electrons in collisions between ions and molecules and that these energies depend only on the target electron binding energies I_b and the charge state q of the projectile. It was assumed that only one electron was involved in the charge exchange process.

In the Extended Over-the-Barrier Model [41, 42, 43], more than one electron can be transferred in collisions between molecules and ions. This can result in the transfer of one electron, as was the case in the previous section, or in the transfer of two or even more electrons.

For us, the most important feature of the Extended Over-the-Barrier Model is the inclusion of the collision velocity; the velocity of the projectile determines how fast the potential barrier will increase and the finite time available for the electron transfer process leads to a probability distribution for the final binding energies rather than a single value.

First we will rewrite the set of equations (3.3-3.5) to allow for multiple electron capture:

$$A^{q+} + B \rightarrow (AB)^{q+} \tag{3.16}$$

$$(AB)^{q+} \rightarrow A^{(q-s)+*} + B^{s+*} + \Delta E \tag{3.17}$$

$$A^{(q-s)+*} + B^{s+*} + \Delta E \rightarrow A^{(q-s)+} + B^{s+} + \Delta E + h\nu \tag{3.18}$$

In the Extended Over-the-Barrier Model, it is important to distinguish between processes that occur on the way in, when the projectile approaches the target and the way out, when projectile moves away again. The target B has m electrons, denoted with an index i. The least bound electron (or in classical terms, the 'outer' electron) has the index $i = 1$, the next one has $i = 2$ and so on. As the ion approaches the target, the potential barrier of all of the individual electrons of B change, as was in the case of the simpler model: the potential experienced by the electron i depends on the number of electrons that is already captured by the projectile c:

$$I_{f,i} = \frac{q-c}{|R-r|} - \frac{i+c}{|r|} \tag{3.19}$$

With decreasing internuclear distance R, the potential barrier will become less effective until some critical distance is reached:

$$R^{in}_{crit,i} = \frac{i + 2\sqrt{iq}}{-I_{b,i}} \tag{3.20}$$

Once the critical distance is crossed, the electron involved will become molecular: it moves in the combined potential well of target and ion. The closest approach (also called *impact parameter*) determines how many electrons will reach the molecular state.

On the way out, the distance between the two nuclei starts to increase again and one by one the electrons will leave the quasi-molecular state in reverse order of appearance (that is, the most inner electron is released first). Every electron i has to 'choose' between capture by the ion or recapture by the target at the distance:

$$R_i^{out} = R_i^{in} \cdot \Big(\frac{\sqrt{q-c_i}+\sqrt{i+c_i}}{\sqrt{q}+\sqrt{i}}\Big)^2 \tag{3.21}$$

It follows that for the most inner electron, R^{out} is equal to R_{in} which means that capture on the way out occurs at the same distance as where it was captured on the way in.

From the position of R^{out}, it is possible to calculate the binding energy the captured electrons will have once the two nuclei are separated again by an infinite large distance:

$$I_i^{out} = I_{b,i} - \frac{q}{R_i^{in}} + \frac{i+c_i}{R_i^{out}} \tag{3.22}$$

The electrons might also be recaptured by the target:

$$I_i'^{out} = I_{b,i} - \frac{q}{R_i^{in}} + \frac{q-c_i}{R_i^{out}} \tag{3.23}$$

3.2.1 Reaction Window

The discussion above assumes that an electron is captured resonantly; the detailed inner structure of the projectile is considered to match the binding energy of the electron(s) from the target perfectly. In practice, this is not the case.

There is an uncertainty in the binding energy due to the finite time an electron needs to cross the potential barrier. In that way, the Extended Over-the-Barrier Model predicts a Gaussian distribution of binding energies around the most probable final binding energy, called the *reaction window.*

The velocity of the projectile v_{rad} determines how fast the potential barrier will raise. The finite time it takes an electron to cross the barrier results in an uncertainty in the barrier height, which can be expressed as:

$$\Delta V = \frac{dV}{dt}\Delta t = \frac{dV}{dR}\frac{dR}{dt}\Delta t = \frac{dV}{dR} \cdot v_{rad} \cdot \Delta t \tag{3.24}$$

where dV/dR is the change of barrier height with internuclear distance as expressed in equation 2.8. Now the assumption is made that this classical uncertainty in the barrier height is equal to the quantum mechanical uncertainty $\Delta V \Delta t \sim 1$ so that a minimum uncertainty is given by:

$$(\Delta V)^2 = \frac{dV}{dR} \cdot v_{rad} \tag{3.25}$$

Both on the way in and on the way out, there was an internuclear distance R at which the height of the potential barrier was equal to the shifted binding energy. Substitution of these distances gives:

$$\left.\frac{dV_1^{in}}{dR}\right|_{R_1^{in}} = \left(\frac{\sqrt{q}+1}{R_1^{in}}\right)^2 \tag{3.26}$$

$$\left.\frac{dV_1^{out}}{dR}\right|_{R_1^{out}} = \left(\frac{\sqrt{q-1}+\sqrt{2}}{R_1^{out}}\right)^2 \tag{3.27}$$

$$\left.\frac{dV_2^{in}}{dR}\right|_{R_2^{in}} = \left(\frac{\sqrt{q}+\sqrt{2}}{R_2^{in}}\right)^2 \tag{3.28}$$

The radial velocity v_{rad} is related to the initial velocity v_0 and the impact parameter b by:

$$v_{rad} = v_0 \cdot \sqrt{1 - \left(\frac{b}{R_i}\right)^2} \tag{3.29}$$

For the calculation of the reaction window, we need the radial velocity averaged over all internuclear distances for which the potential barrier can be crossed. In that way the average velocity at R_1^{in}, R_1^{out} and R_2^{in} is found to be:

$$\bar{v}_{rad,1}^{in} = v_0 \frac{2}{3} \frac{R_1^{in}}{R_2^{in}} \left\{1 - \left(1 - \left(\frac{R_2^{in}}{R_1^{in}}\right)^2\right)^{\frac{3}{2}}\right\} \tag{3.30}$$

$$\bar{v}_{rad,1}^{out} = v_0 \frac{2}{3} \frac{R_1^{out}}{R_2^{in}} \left\{1 - \left(1 - \left(\frac{R_2^{in}}{R_1^{out}}\right)^2\right)^{\frac{3}{2}}\right\} \tag{3.31}$$

$$\bar{v}_{rad,2} = \frac{2}{3} v_0 \tag{3.32}$$

The distribution around the most probably populated level n for an electron i is assumed to be a Gaussian distribution with a standard deviation given by:

$$(\Delta E_i)^2 = (\Delta V_i^{in})^2 + (\Delta V_i^{out})^2 \tag{3.33}$$

If more electrons are captured their ΔE should also be quadratically added. The reaction window can now be expressed as:

$$\Delta W(E) = \frac{1}{\sqrt{2\pi} \cdot \Delta E} \exp\left(- \frac{1}{2}\left(\frac{E - I_i}{\sqrt{2}\Delta E}\right)^2\right) \tag{3.34}$$

Way in		Way out				
R_1^{in}	R_2^{in}	R_2^{out}	R_1^{out}	$I_{f,2}^{out}$	$I_{f,1}^{out}$	$I'^{out}_{f,1}$
6.48	4.71	4.71	6.48	-34.7	-24.5	-20.3

Table 3.2: Over-the-Barrier model for HeIII + H_2, capture distances (atomic units) and binding energies (eV).

The reaction window can be used to roughly predict the final state of the ion by considering the overlap between the reaction window and the binding energies of the final ionic states. It widens as the velocity increases with a $v^{1/2}$ dependence and it can be seen from Figure 3.2 that for larger velocities, more states can be populated.

Like the classical model, the extended Over-the-Barrier model tends to overestimate the cross section. More accurate models, such as the multi channel Landau-Zener model [44], include more of the molecular structure. Although these models do give a more accurate description of the total cross section, they fail to predict the exact (n, l) distribution [45].

3.2.2 HeIII + H_2

To demonstrate the model, we will discuss the example of charge exchange between molecular hydrogen and fully stripped helium here.

First consider single electron capture, Figure 3.2. The projectile can capture either the inner or the outer electron. The reaction window for capture of the outer electron mainly overlaps with the $(2l)$ state, but it can be seen that the higher excited states are also within reach of the reaction window.

The reaction window of capture of the inner electron falls in between the ground state and the first excited level of the helium ion and is therefore less favourable.

The width of the reaction window strongly depends on the projectile velocity as is shown in Figure 3.3. This means that with an increasing velocity, more channels open and electrons will be captured into higher excited states. From the figure it also becomes clear that for lower velocities, the reaction window overlaps less with the $(2l)$ state. Single electron capture into the HeII$(2l)$ state will therefore be strongly dependent on the velocity.

Now consider double electron capture, Figure 3.4. The model presented in the previous sections predicts that the electron is captured into $(1l)$ as the reaction window coincides with the position of the ground state. This treatment assumes completely independent capture of the two electrons.

From experiments however, it is known that electrons are captured into the HeI$(1s2p)$ state. This can be understood by introducing an extension to

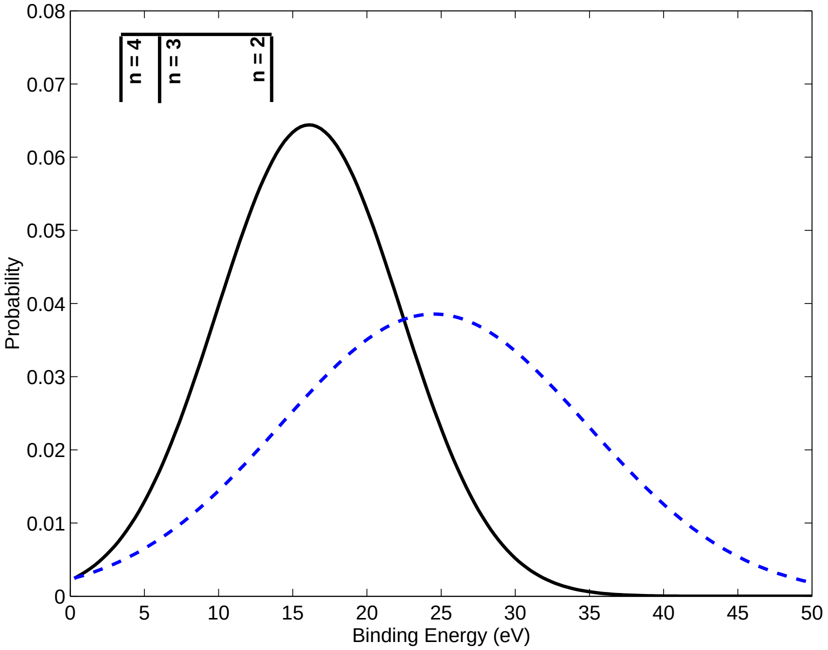

Figure 3.2: Reaction window for single Electron Capture by He^{2+} from H_2 with v = 2.25 keV/amu. Black line: capture of the outer electron. Blue dashed line: capture of the inner electron. The position of the He^{+} excited states are indicated.

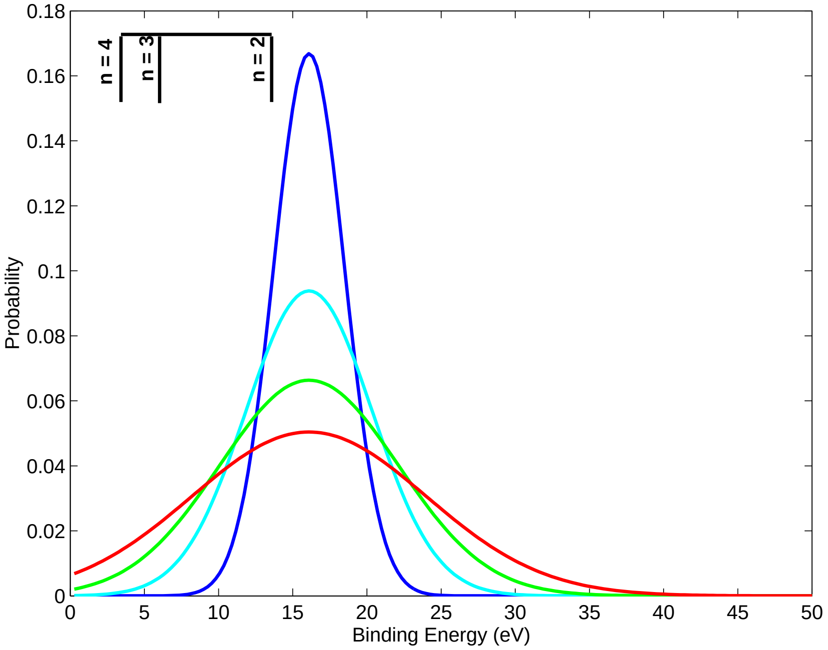

Figure 3.3: Widening of the reaction window for single electron capture by He^{2+} from H_2 for different solar wind velocities. Blue: 0.05 keV/amu, cyan: 0.5 keV/amu, green: 2 keV/amu and red: 6 keV/amu.

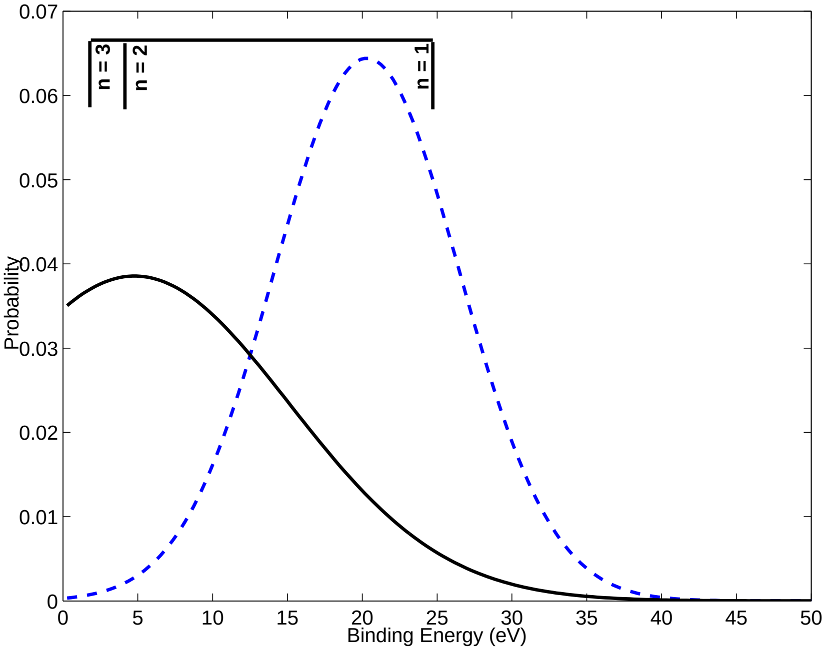

Figure 3.4: Reaction window for double Electron Capture by He^{2+} from H_2 with v = 2.25 keV/amu. Blue dashed line: independent capture of the two electrons. Black line: capture with energy transfer from the inner to the outer electron. The position of the He states are indicated.

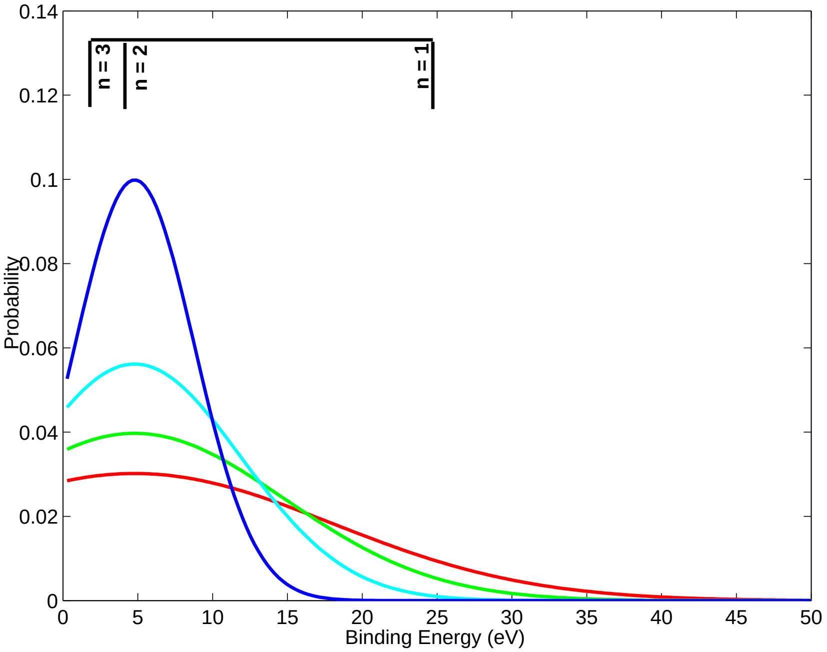

Figure 3.5: Widening of the reaction window for double electron capture by He^{2+} from H_2 for different solar wind velocities in the case of auto-excitation. Blue: 0.05 keV/amu, cyan: 0.5 keV/amu, green: 2 keV/amu and red: 6 keV/amu.

the model that assumes that the total binding energy of the system is the relevant quantity.
When leaving the quasi-molecular state, assume that the inner electron is captured into the HeII ground state. This ground state has a binding energy of -54.4 eV; the final binding energy of the inner electron in the quasi-molecular system was -34.7 eV, *cf.* Table 3.2. This means that 19.7 eV 'becomes available' for the outer electron. During the molecular state, this electron had a binding energy of -24.5 eV. Transfer of the released energy results in a new binding energy of -4.79 eV for the outer electron.
This process is thus an auto-excitation process and the reaction window is shown in Figure 3.3. Clearly, the preferred shells have an $n \geq 2$.
As with single electron capture, the reaction window for double electron capture was calculated at different velocities typical for the solar wind, Figure 3.5. It can be seen that because capture into the first excited state of HeI is almost resonant, the cross section of this process will not vary much with the collisional velocity.

3.3 Measuring Cross Sections

Electron capture processes can be studied by different techniques, each of which has particular advantages. A rough distinction between applied methods would be:

- **Photon Emission Spectroscopy (PES)** is the method used at the KVI. It allows for the measurement of state selective cross sections by detection of the photons that are emitted in the charge exchange reaction [46, 47, 48];

- **Translational Energy Spectroscopy (TES)** is a method that uses the kinetic energy that the projectile gains or looses during the charge exchange reaction. Within the limitations of the available energy resolution, the TES technique allows to distinguish different reaction channels such as dissociative and non-dissociative electron capture [49, 50].

- **Recoil Ion Momentum Spectroscopy (RIMS)** is based on measurement of the momenta of the reaction products. With this technique the collision dynamics of collision systems can be completely resolved so that differential cross sections can be obtained. At the KVI, this technique is used in combination with a magneto-optical trap [51, 52].

Other methods that are used to study charge exchange collisions are **Auger electron spectroscopy** [53] where the momenta of electrons that are released during the process are measured and the **retarding field** technique [54, 55] in which the number of projectile ions before and after the collision is compared.

3.3.1 Experiment

At the KVI Atomic Physics Facility heavy ions can be produced using an Electron Cyclotron Resonance Ion Source (ECRIS, [56]). In an ECRIS, a plasma is confined by a magnetic trap. Electrons will gyrate around the magnetic field lines with a cyclotron frequency ω_c and they can be heated up by applying a resonant radio frequency field, approximately 14 GHZ. Electron impact is used to ionize the atoms in the ECRIS and subsequent charge states can be achieved by repeated electron collisions. The range of charge states is limited by the increasing amount of energy required to strip ions any further and recombination processes like electron capture. After the ions are extracted from the source they are selected by a 110° bending magnet according to their mass per charge ratio m/q. The selected ions then enter the beam line, where the ion beam is focussed by means of three sets of quadrupole triplet magnets. Another magnet is used to bend it into the experimental set up.

When the ions leave the ECRIS, they have a kinetic energy of

$$E = q \cdot V_{ECR} \tag{3.35}$$

where V_{ECR} is the potential of the ion source, typically 3.5 kV. The ions can be decelerated with the use of an octopole ion beam guide so the setup allows for the use of ions in a wide range of astrophysically relevant velocities (0.01 - 10 keV/amu).

Figure 3.6 gives a schematic drawing of the setup. The ions coming from the beam line are first collimated and focussed by an electrostatic lens system [45]. This lens system consists of three lens elements and three diaphragms, and the potential on each of these components has to be carefully tuned to optimize the shape and trajectory of the beam as the ions are decelerated. The retarded ions then enter the main part of the setup, a vacuum chamber with the octopole ion trap (Figure 3.7) at its center.

The octopole is based on the technique of Radio Frequency multipole ion guiding. With eight stainless steel 'wedges of pie', an electric field gradient in radial direction with respect to the ion beam is created. An RF voltage is applied on the bars such that between neighboring bars, there is a phase difference of 180°. The resulting field confines the decelerated ions very effectively in the radial direction, as the effective potential V_{eff} in the octopole

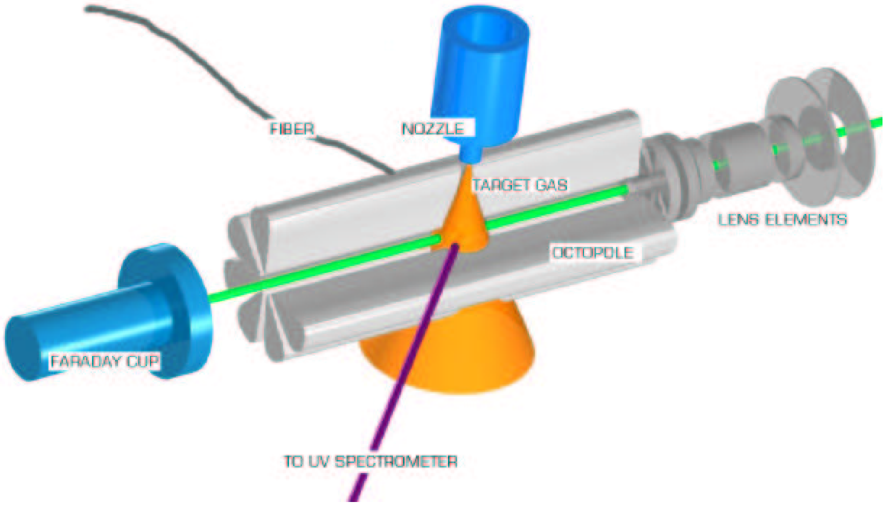

Figure 3.6: Artistic impression of the AGORA set up. The ion beam enters the lens system from the right and crosses the target at the center of the octopole.

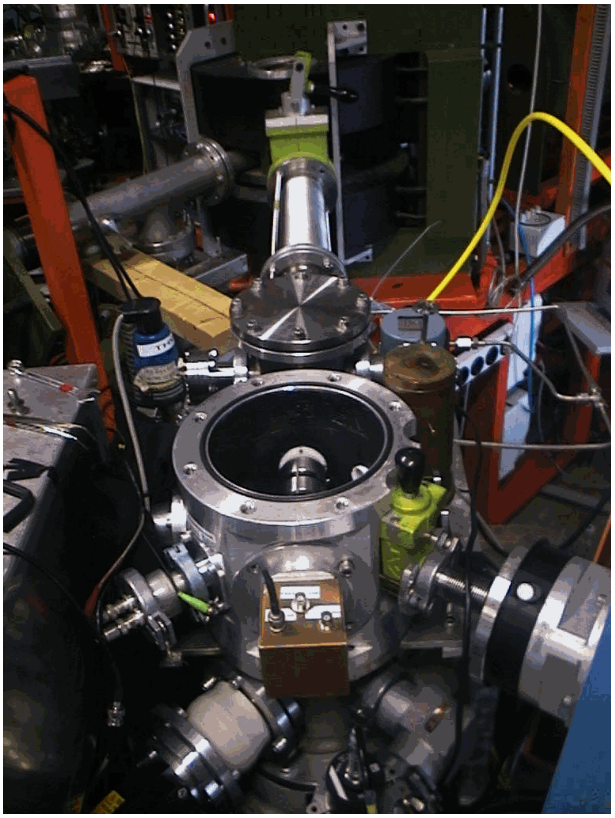

Figure 3.7: Photograph of AGORA where the top flange that closes the reaction chamber is removed. The ions come in from the above. The lens system is placed underneath the blind flange and in the opened reaction chamber, the octopole can be seen. At the right, the VUV spectrometer is placed; at the left, a metal box can be seen which contains the optical spectrometer. The copper box at the center encloses the Faraday cup.

becomes very steep with respect to the position r in the octopole [57]:

$$V_{eff} \propto r^6 \tag{3.36}$$

The target gas enters the setup through a nozzle which fits into the octopole. The use of a nozzle has the advantage that the target is a gas beam so that the density in the gas beam can be relatively high while single collision conditions are maintained. The space between the different bars allows light to escape, which is essential to do photon emission spectroscopy by means of both a vacuum ultraviolet spectrometer (8-80 nm) and an optical spectrometer (300-600 nm). The VUV spectrometer is connected directly to the setup; an optical fiber is used to guide visible light into the optical spectrometer (Figures 3.6 and 3.7).

3.3.2 Cross Sections

The experimental technique of Photon Emission Spectroscopy can be used to study state selective electron capture by means of the photons that are emitted in this process.

Consider again Figure 3.6, where the ion beam collides on the target beam in the center of the octopole. Photons can thus originate from a region with length L along the ion beam but their detection is limited by the solid angle of observation ω and the quantum efficiency $K(\lambda)$ of the detector used. The relation between the emission cross section $\sigma_{em}(i \rightarrow f)$ and the photon count S in a period T is given by [48]:

$$\sigma_{em}(i \rightarrow f) = S \cdot \frac{4\pi}{\Omega K(\lambda)} \frac{qe}{NQ} \frac{1}{\int_L n(z)dz} \tag{3.37}$$

where N ions with charge q collide on a target beam with density $\int_L n(z)dz$ along the position on the ion beam z; e denotes the elementary charge constant and Q is the accumulated ion charge.

In photon emission spectroscopy, it is important to distinguish between different cross sections. What is measured in the setup is the emission cross section $\sigma_{em}(i \rightarrow f)$ for a transition from state i to the state f; what we are looking for is the state selective cross section $\sigma(i)$. The relation between these two cross sections can be understood by looking at a transition scheme, see Figure 3.8. In the case of single electron capture, the number of photons that are emitted at 30.4 nm is measured and from the equation 2.39, the emission cross section for the transition $(2p \rightarrow 1s)$ can be determined. From the quantum mechanical 'selection rules' it follows that this transition is the only path by which electrons in the $(2p)$ state can relax so the branching

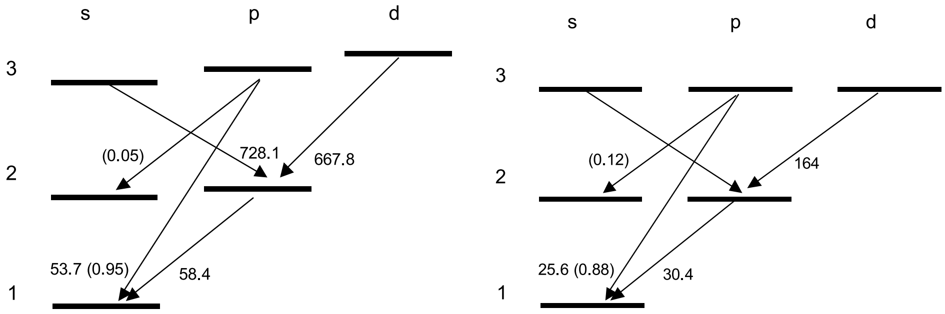

Figure 3.8: Transition schemes for neutral He (left) and ionized He^+ (right). The wavelengths (in nm) and branching ratios (between brackets) are indicated.

ratio is equal to 1. The branching ratio B_{if} for the transition from i to f is defined as the relative transition probability through a certain channel:

$$B_{if} = \frac{A_{if}}{\sum_j A_{ij}} \tag{3.38}$$

with A_{if} the transition probability for the transition $(i \rightarrow f)$ and $\sum_j A_{ij}$ the sum of the transition probabilities of all possible transitions from the state (i). The sum of all transition probabilities is equal to the inverse of the lifetime of the state concerned:

$$\sum_j A_{ij} = \tau^{-1} \tag{3.39}$$

We return to the example of the 30.4 nm line resulting from single electron capture by fully stripped helium into the $(2p)$ state. Electrons might also be captured in higher excited states such as the $(3s)$ state. Relaxation of this state would lead to an increase of the population of the $2p$ state so that the photons arising from the $(2p \rightarrow 1s)$ transition contain information about both direct capture in the $(2p)$ state and capture in the $(3s)$ state.

If there is a significant cascade contribution $(k \rightarrow i \rightarrow f)$ to the population of a state i, the state selective cross section $\sigma(i)$ can be corrected for this effect:

$$\sigma(i) = \frac{\sigma_{em}(i \rightarrow f)}{B_{if}} - \sum_k B_{ki}\sigma(k) \tag{3.40}$$

where the last term describes electrons captured in a state (k). This excited state has a state selective cross section $\sigma(k)$ and transitions to the state i have a branching ratio B_{ki}.

3.4 Helium Electron Capture

Helium (from '$\eta\lambda\iota o\varsigma$ - the Sun) is the second most abundant element in the solar wind (Section 2.3). It was already mentioned before that all solar wind helium is fully stripped and therefore, collision processes with He^{2+} and molecules that are typical for the cometary environment will be discussed here. First, collisions with carbon monoxide will be studied:

$$\mathrm{He}^{2+} + \mathrm{CO} \rightarrow \begin{cases} \mathrm{He}^{+} + \mathrm{CO}^{+} & \mathrm{SEC} \\ \mathrm{He} + \mathrm{CO}^{2+} & \mathrm{DEC} \end{cases} \tag{3.41}$$

where the abbreviations SEC and DEC denote single- and double electron capture respectively. For the technique of photo electron spectroscopy, that uses individual transition lines, *state selective* cross sections are of relevance. The excited states studied here are $\mathrm{He}(1s2p)$ and $\mathrm{He}^{+}(2p)$. Relaxation of the SEC $\mathrm{He}^{+}(2p)$ system to the ground state $\mathrm{He}^{+}(1s)$ results in an emission line at 30.4 nm; the DEC $\mathrm{He}(1s2p) \rightarrow \mathrm{He}(1s^2)$ yields a line at 58.4 nm, see also the transition schemes in Figure 3.8.

3.4.1 Single electron capture

Using the AGORA set up, single electron capture from neutral CO by fully stripped helium ions was studied. Figure 3.9 compares total cross sections with state selective cross sections for electron capture into the (2p) state. Obviously, the emission cross section should always be smaller than (or equal to) the total cross section. Below 10 keV/amu, the total cross section of one electron capture decreases by approximately one order of magnitude; the same occurs for velocities above 10 keV/amu. However, the cross section of capture in the $(2p)$ state falls much faster; at high energies, its cross section is about the same as the total cross section but at energies as low as 0.2 keV/amu, capture in this excited state accounts for less than 10% of the total cross section.

Comparison with other measurements [50, 53] shows that at energies below 1 keV/amu most electron capture occurs through dissociative channels where the CO is 'broken up in pieces' and the helium is left in its ground state. At higher energies, the $\mathrm{He}^{+}(2p)$ channel 'opens' (it falls well within the reaction window) and the relative importance of capture into the $(2p)$ state will increase.

At energies higher than 0.5 keV/amu, some capture into the $(n = 3)$ state has been measured by Kearns *et al.* [50]. However, capture into this state is a factor of 25 rarer than capture into the $(n = 2)$ state.

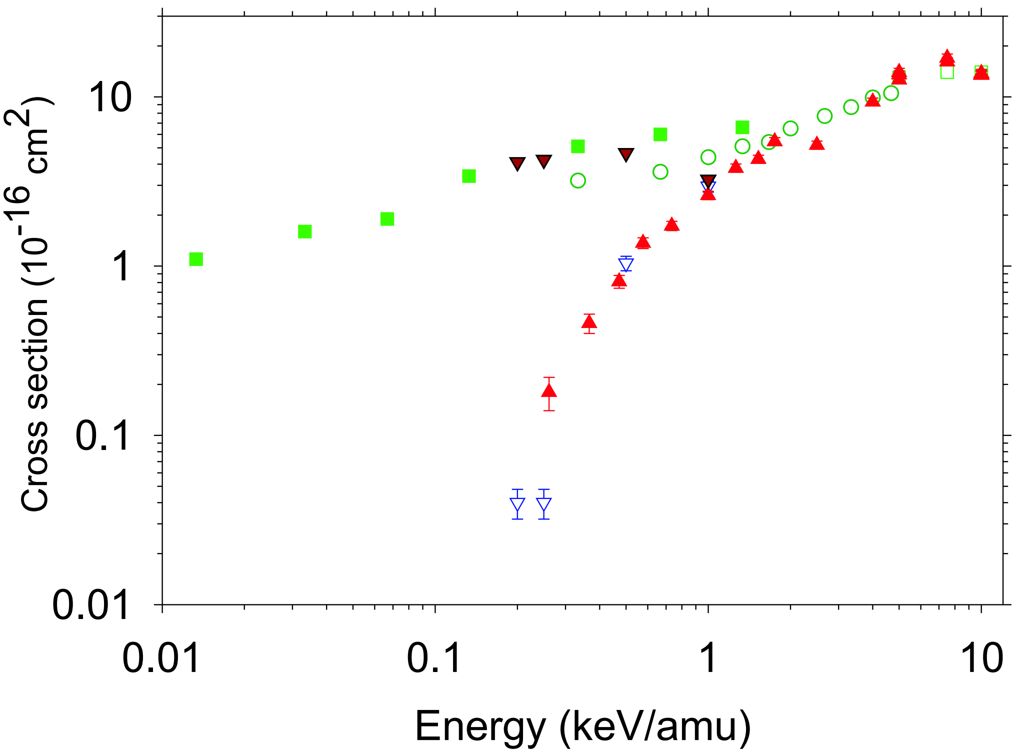

Figure 3.9: Cross sections for single electron capture by He^{2+} from CO at different projectile velocities. Total cross sections: filled green squares (Ishii *et al.* [58]), open green squares (Rudd *et al.* [59]) and open green circles (Čadež *et al.* [55]). Capture into the ground state (Kearns *et al.* [50]) is indicated by reverse brown triangles; capture into $(2l)$ is indicated by reverse open blue triangles (Kearns *et al.* [50]); red triangles, capture into $(2p)$, this work.

3.4.2 Double electron capture

Double electron capture is a more complex process than single electron capture because it involves both inner and outer electrons. A discussion in terms of the reaction window for DEC was done by Folkerts *et al.* [60] for an energy of 4 keV/amu. It was concluded that capture of the two outer electrons of CO is unlikely as the reaction window for this process falls exactly in between the He$(1s2l)$ and the He$(2l2l')$ states. Because for the inner electrons the reaction window overlaps exactly with the He$(1s2l)$ states, inner electrons rather than the outer electrons will be captured, resulting in a more complex capture process.

In the energy range 0.1-10 keV, the total DEC cross section decreases by approximately an order of magnitude [59, 58, 55]. The state selective cross section for the He$(1s2p)$ state is more or less constant within this region and

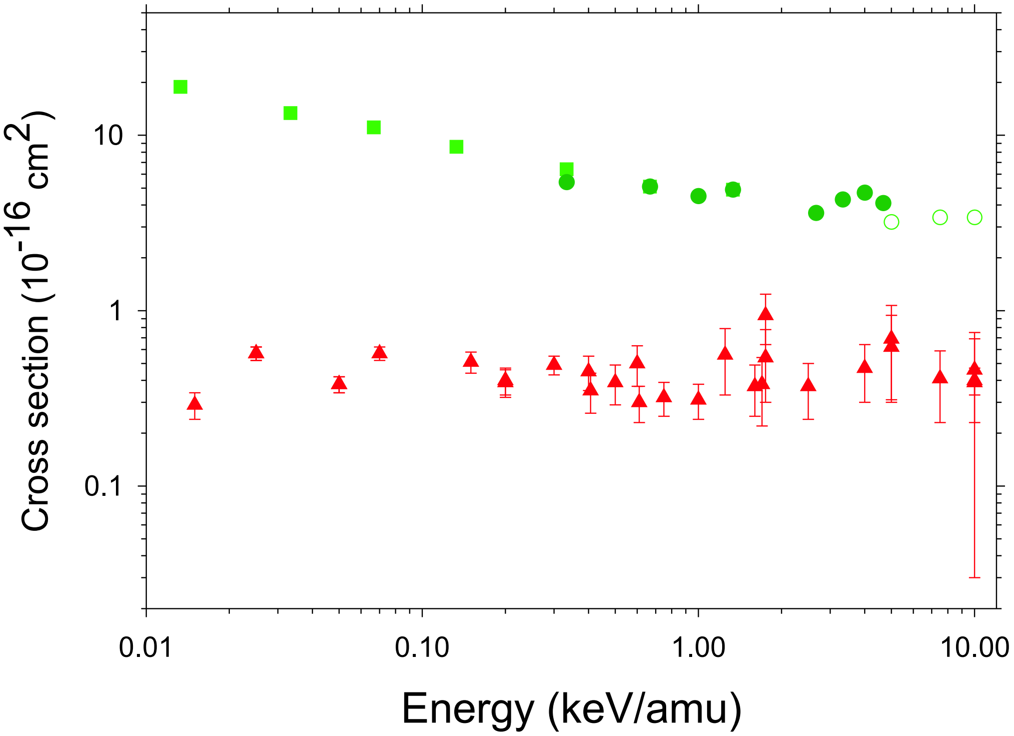

Figure 3.10: Cross sections for double electron capture by He^{2+} from CO at different projectile velocities. Total cross sections DEC: filled green squares (Ishii *et al.* [58]), open green circles (Rudd *et al.* [59]) and filled green circles (Čadež *et al.* [55]). DEC into the $(1s2p)$ state: red triangles, this work.

it accounts for a relatively small part of the total cross section. This effect might be explained by the reaction window mentioned above: as the capture is resonant with the He$(1s2l)$ states, narrowing of the reaction window by decreasing the velocity does not affect the state selective cross section much. These results can also be understood in terms of the influence of the molecular structure of CO on state selective capture; double capture involves both inner and outer electrons so that much more reaction channels are available [53]. Many of those reaction channels lead to dissociation of the CO molecule and the neutral helium is left in its ground state.

3.4.3 Competition between SEC and DEC

At low energies, helium-carbon monoxide collisions are dominated by double electron capture; at high energies, this is just the other way around. This is illustrated in Figure 3.11 where the ratio of state selective single electron

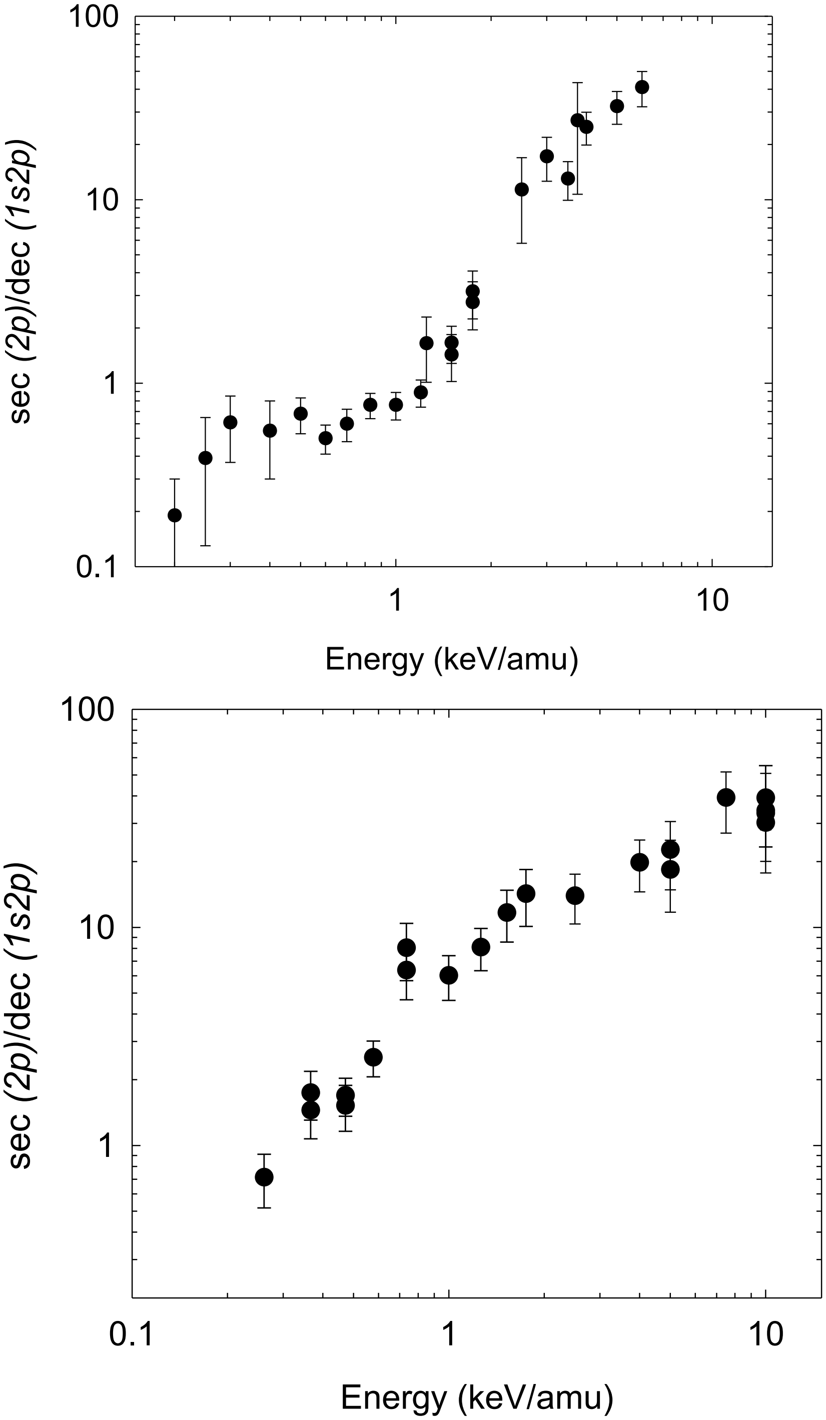

Figure 3.11: Velocity dependence of the ratio between single- and double electron capture for He^{2+} with CO (upper part) and He^{2+} with H_2 (lower part).

capture in the ($2p$) state and state selective double electron capture in the ($1s2p$) state is plotted versus the projectile velocity. This ratio will be denoted as SEC/DEC; although this abbreviation is not accurate (because no distinction is made between total and state selective capture), it does make life a little easier.

The relation between the ratio of state selective single- and double electron capture and the projectile velocity can be understood in terms of the extended Over-the-Barrier model, *cf.* Section 3.2.2. Double electron capture into the HeI($1s2p$) state is an almost resonant process which therefore is almost not affected by widening the reaction window; the reaction window of single electron capture however overlapped less with the HeII($2p$) state so that this process is much more dependent on the collisional velocity.

The SEC/DEC ratio is also shown for collisions of He^{2+} with molecular hydrogen [46]. It clearly follows the same trend as the SEC/DEC ratio for CO, although the two plots show differences at specific velocities.

3.4.4 Single electron capture by HeII

In our setup, the use of a target jet has to assure that only one charge transfer reaction takes place. In a cometary environment, this might not be the case (Section 4.1). This would mean that an He^{2+} ion that has already captured an electron captures another electron in a subsequent collision with a neutral molecule:

$$\mathrm{He}^{2+} + \mathrm{CO} \rightarrow \mathrm{He}^{+} + \mathrm{CO}^{+} \tag{3.42}$$

$$\mathrm{He}^{+} + \mathrm{CO} \rightarrow \mathrm{He}(1s2p) + \mathrm{CO}^{+} \tag{3.43}$$

It is already suggested by the notation that this process, called *sequential* electron capture (SEQ) also leads to emission at 58.4 nm because of electron capture into the excited state ($1s2p$). Figure 3.12 shows the state selective cross section for electron capture by HeII into this state.

From our classical Over-the-Barrier predictions (Table 3.1) it is to be expected that most of the sequential electron capture occurs in the ground state of the neutral helium. HeII electron capture into ($1s2p$) indeed has a relatively small cross section at low velocities. For projectile energies larger than 2 keV/amu however, the state selective cross sections for HeII capture and DEC are comparable. This might be explained in terms of a widening reaction window for HeII capture into ($1s2p$) with increasing velocity, as was the case for SEC into ($2p$), while the double electron capture is forced to occur into the ground state due to the increasing amount of molecular reaction channels that were mentioned before. Single HeII electron capture does

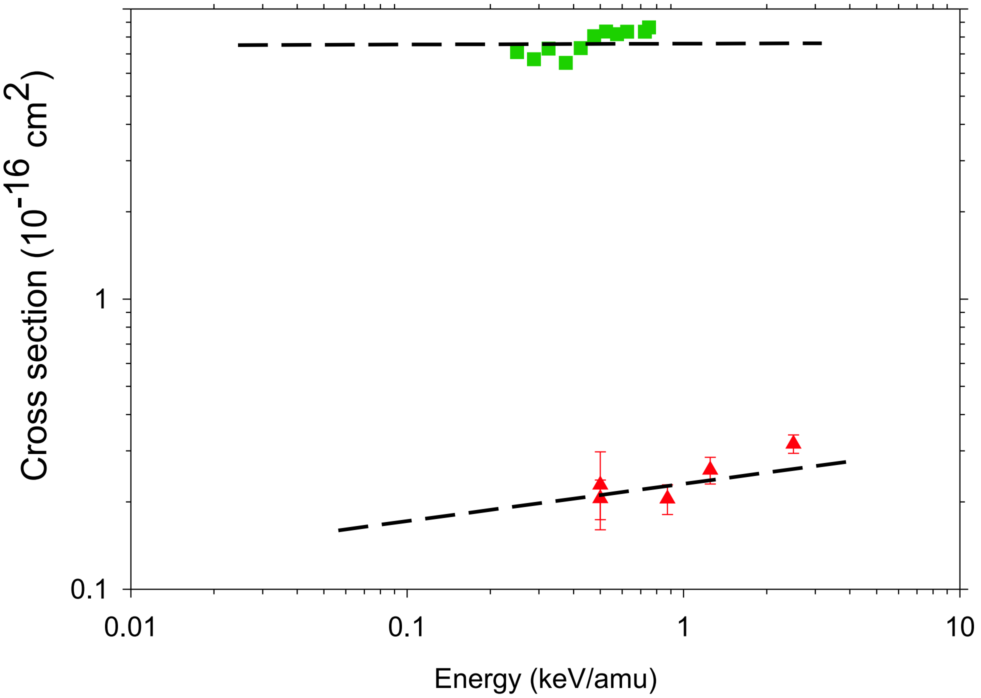

Figure 3.12: Cross sections for single electron capture by He^+ from CO at different projectile velocities. Total cross sections SEC: dark green squares (Moran *et al.* [61]). SEC into the $(1s2p)$ state: red triangles, this work.

not suffer from these molecular effects because only one (outer) electron is captured.

Chapter 4

Collisions in the Coma

In the previous section, it was shown that state selective single- and double electron capture are strongly dependent on the velocity of the projectile. However, because the cometary situation is rather different from the laboratory, it is not possible to use the ratio between state selective single- and double electron capture directly as a diagnostic tool.

In this chapter, a simple two dimensional cometary model is developed that can be used as a diagnostic tool to study the interaction between comets and the solar wind. This model is summarized in Figure 4.1. The cometary nucleus continuously produces neutral water and CO, which flows into space until it is ionized or destroyed by sun light. The flow of solar wind ions therefore encounters a mixture of the original molecules and their dissociation products, mainly atomic oxygen and hydrogen. Charge exchange reactions will now neutralize the helium ions; either directly by double electron capture, or by the consecutive capture of two electrons (sequential electron capture). The model presented here consists of two parts; first, it predicts the charge state distribution of the solar wind helium that flies through the coma and this model is used to understand in situ measurements by the Giotto spacecraft of the helium charge state distribution within comet Halley.

Second, the photon emission resulting from the charge exchange reactions in a cometary environment is modelled. The results of this emission model are compared to FUV observations of both Hale-Bopp and Hyakutake.

4.1 Cometary Model

In the solar wind, all helium is fully stripped. When helium ions fly through a cometary gas, the charge state distribution of the helium ions will change. Single charge exchange will then populate the HeII state and double charge

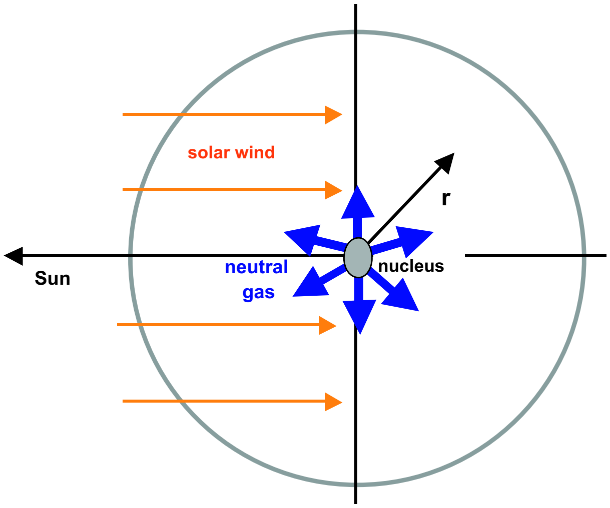

Figure 4.1: Model overview: solar wind helium ions (orange ions) fly into a cometary environment that is created by continuous sublimation of gas from the nucleus (blue arrows). By introducing a spherically symmetric density distribution dependent on the distance to the nucleus r, the charge state distribution of solar wind helium can be modelled.

exchange populates the neutral HeI state. Because the density increases rapidly when the cometary nucleus is approached, the charge state distribution varies along the ion's path through the coma.
Consider a helium ion that moves along a straight line r on the comet-Sun axis. The cometary nucleus is located at $r = 0$, the Sun is located at $r = -\infty$, so r has only negative values. There are three possible charge states (HeIII, HeII an HeI) and three processes that connect these states (SEC, DEC and SEQ). The charge state distribution can now be written as a set of differential equations:

$$\frac{dN_{III}(r)}{dr} = -\frac{dN_{sec}}{dr} - \frac{dN_{dec}(r)}{dr} \tag{4.1}$$

$$\frac{dN_{II}(r)}{dr} = \frac{dN_{sec}(r)}{dr} - \frac{dN_{seq}(r)}{dr} \tag{4.2}$$

$$\frac{dN_{I}(r)}{dr} = \frac{dN_{dec}(r)}{dr} + \frac{dN_{seq}(r)}{dr} \tag{4.3}$$

Here, $N_{III}(r)$ denotes the HeIII density, $N_{II}(r)$ is for HeII and $N_I(r)$ is the density of neutral helium atoms. The number of single electron capture reactions is denoted by $N_{sec}(r)$; $N_{dec}(r)$ is the number of double electron captures and $N_{seq}(r)$ denotes the number of reactions where one electron is

captured by a HeII ion.
The variation of the number of electron captures of each of the three processes depends on the density of molecules and atoms in the coma. Here, we have to distinguish between hydrogen atoms, which can only donate one electron and the other neutrals, from which one or two electrons can be taken. The model treats all the particles from the latter group as one effective species:

$$\begin{aligned}
\frac{dN_{sec}(r)}{dr} &= N_{III}(r)\cdot\Big(\rho_m(r)\sigma_{sec}+\rho_H(r)\varsigma_{sec}\Big) && (4.4)\\
\frac{dN_{dec}(r)}{dr} &= N_{III}(r)\cdot\rho_m(r)\sigma_{dec} && (4.5)\\
\frac{dN_{seq}(r)}{dr} &= N_{II}(r)\cdot\Big(\rho_m(r)\sigma_{seq}+\rho_H(r)\varsigma_{seq}\Big) && (4.6)
\end{aligned}$$

Here, $\sigma_{sec}, \sigma_{dec}$ and σ_{seq} denote the total cross sections for electron capture in collisions between helium and molecules; ς_{sec} and ς_{seq} are the total single- and sequential electron capture cross section for collisions between helium and atomic hydrogen. The number density of hydrogen atoms is denoted by $\rho_H(r)$; the molecular number density by $\rho_m(r)$. From equation 2.1, a general relation for the number density of a specific species i is given by:

$$\rho_i = \frac{Q_i}{4\pi r^2 v_{gas}}\cdot\exp\left[-r/h\right] \qquad (4.7)$$

where Q_i is the comet's production rate of the species i and where h_i is the scale length of this species.
When water molecules are dissociated by sunlight, a neutral hydroxyl atom and a hydrogen atom are formed [10]:

$$\mathrm{H_2O}+\nu\rightarrow\mathrm{OH}+\mathrm{H} \qquad (4.8)$$

Dissociation of these hydroxyl molecules produces one hydrogen and one oxygen atom.

$$\mathrm{OH}+\nu\rightarrow\mathrm{H}+\mathrm{O} \qquad (4.9)$$

The atomic oxygen itself is photo ionized with a scale length of $h_O \approx 2{\cdot}10^6 km$, after which it is picked up by the solar wind. Like water and hydroxyl, atomic oxygen allows for both single- and double electron capture [63]. Therefore, the number of collision partners that can participate in all the electron capture processes is not affected by the dissociation processes 4.8 and 4.9 but only by the scale length of photo ionization of atomic oxygen. Including oxygen, the molecular density is described by:

$$\rho_m = \frac{1}{4\pi r^2 v_{gas}}\cdot\Big(Q_{H_2O}\cdot\exp\left[-r/h_O\right]+Q_{CO}\cdot\exp\left[-r/h_{CO}\right]\Big) \qquad (4.10)$$

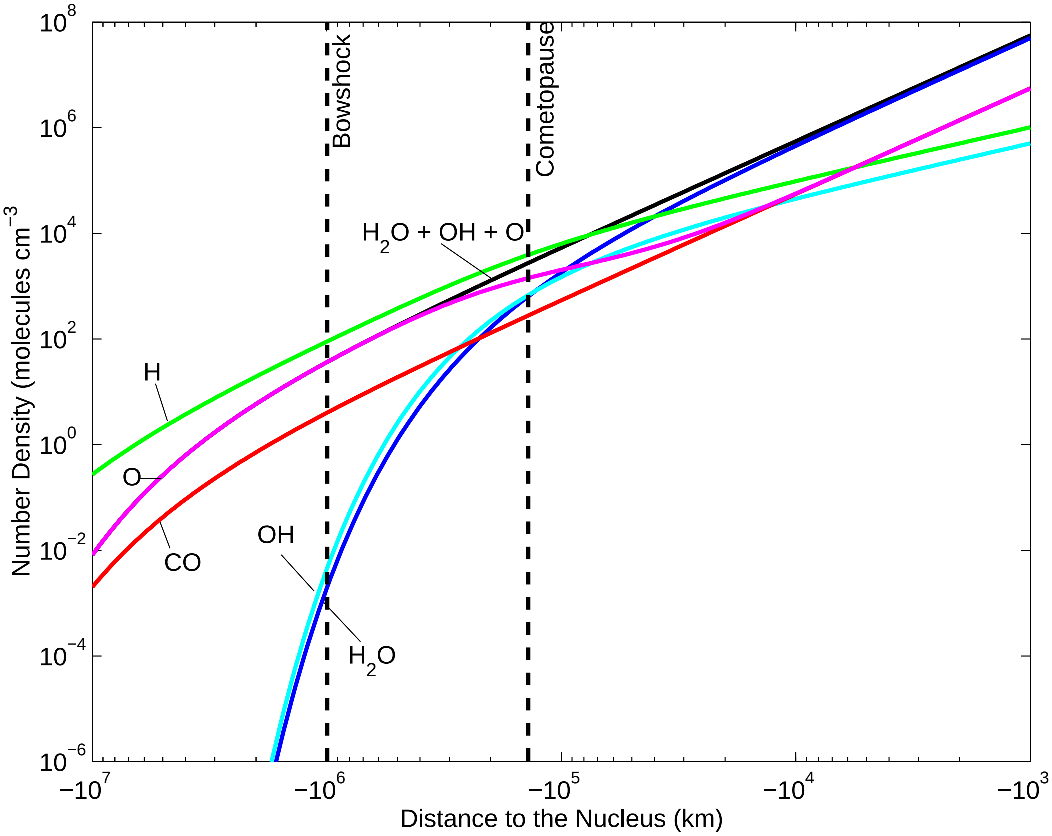

Figure 4.2: Density model for a Halley-like comet at 1 A.U. from the Sun. Black is the combined H_2O, OH and O number density; blue is for water, cyan for OH, green is for atomic hydrogen, red for CO and magenta for atomic O. Both the bowshock and the cometopause are indicated, distances taken from Ip *et al.* [62]

were Q_{H2O} and Q_{CO} are the water and carbon monoxide production rates, h_O is the ionization scale length for atomic oxygen and h_{CO} is the ionization scale length for CO. For every water or hydroxyl molecule that is dissociated, a hydrogen atom is formed. The hydrogen number density can therefore be expressed as [64]:

$$\rho_H(r) = 2 \cdot \frac{Q_{H2O}}{4\pi r^2 v_{gas}} \cdot \frac{h_H}{h_H - h_{H2O}} \cdot \Big(\exp\left[-r/h_H\right] - \exp\left[-r/h_{H_2O}\right] \Big) \quad (4.11)$$

where the factor 2 is included because both the dissociation of water and the dissociation of OH produce a hydrogen atom.

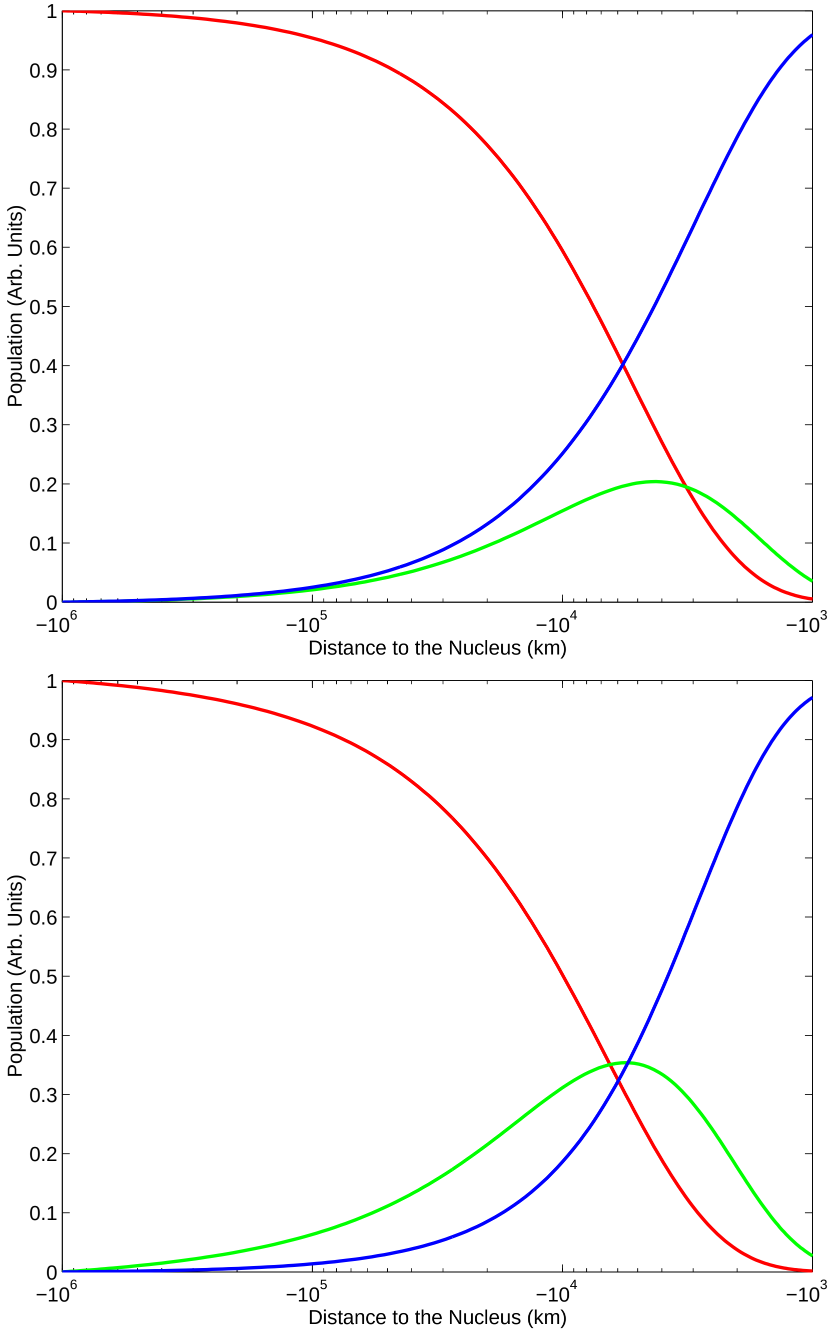

Figure 4.3: Charge state distribution for helium ions flying through a Halley-like comet at a heliocentric distance of 1 A.U. Upper figure: slow wind (0.25 keV/amu). Lower figure: fast wind (6.0 keV/amu). HeIII: red, HeII: green and HeI: blue.

4.1.1 Cometary Density

A model for a Halley-like comet at 1 A.U. from the Sun is shown in Figure 4.2. Here, a gas production rate of $Q = 7 \cdot 10^{29}$ s^{-1}, a gas velocity of 1 km/s and a CO abundance of 10% were used. Near the nucleus, water (and then CO) are the dominant gas phase species. The water is rapidly converted first into OH and H (around 10^5 km) and then almost simultaneously into O + H (+ H). In contrast, CO which has a very small photo ionization and dissociation cross section stays abundant until the bowshock. Therefore, at large distances CO is the most abundant molecular species but the coma is dominated by atomic hydrogen and oxygen.

4.1.2 Charge State Distribution

The cross section of helium colliding on CO was used for the molecular part of the cometary gas. Total charge exchange cross sections for helium colliding with CO were taken from the experimental work reported in the previous section. For collisions between helium ions and atomic hydrogen, a mix between theoretical and experimental data was used (Appendix A).

Using the constraints that initially there is no HeII nor HeI state, the set of differential equations can now be solved numerically. Matlab was used to solve this set of differential equations from a distance of 10^6 to a 1000 km from the nucleus. The results show it can be seen that solar wind helium ions can fly through the coma relatively unhindered up to a distance of 10^5 kilometers from the nucleus -the hydrogen dominated zone- and the original charge state distribution is retained.

At 10^4 km from the nucleus, the density becomes high enough for larger numbers of collisions to take place. Because the single electron capture cross section increases with velocity, the HeII abundance accounts for a larger fraction of the total population in case of a fast wind than in the slow wind. The slow wind on the other hand has a larger neutral fraction because of the larger DEC cross section.

When the gas production rate Q is lowered, the number of collisions decreases dramatically: in the case of an Encke-like comet ($Q = 10^{27}$ s^{-1} at 1 A.U.), the helium ions easily reach the contact surface without collision induced changes of the distribution.

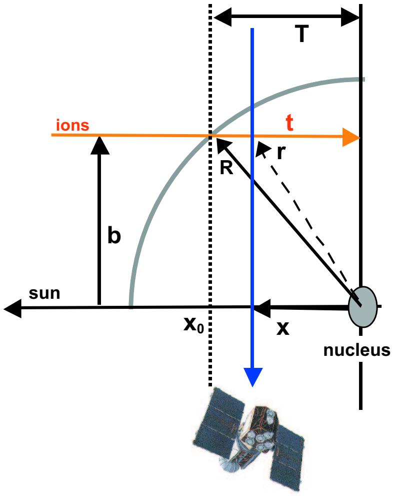

Figure 4.4: Schematic view of the geometry of the observation. Ions flying along a trajectory (orange arrow) will capture an electron and emit a photon depending on the local density of the comet. An observer (EUVE) moving along the comet-Sun axis sees the sum of the light that comes from all the different (parallel) trajectories, blue arrow.

4.2 Intensity Model

4.2.1 Geometry

Once the helium charge state distribution is known, it is possible to calculate the comet's luminosity in both the 30.4 and the 58.4 nm lines. To do this, a closer look at the geometry of the cometary system is to be introduced.

Consider a plane through the comet-Sun axis. This plane is shown from above in Figure 4.4. If an observer would travel along the comet-Sun axis, looking into a direction perpendicular to this axis, he would see the source function resulting from all the electron capture reactions that occurred at each point.

A solar wind ion travelling along a trajectory parallel to the comet-Sun axis approaches the nucleus up to a distance b, the impact parameter. It enters the coma at the point x_0 and it has to travel a distance T before it reaches the point of closest approach. This T is given by the sum of the squares of the trajectory's impact parameter b and the radius of the coma R:

$$T^2 = R^2 - b^2 \tag{4.12}$$

The density along the trajectory is a function of r, the distance to the nucleus:

$$r^2 = x^2 + b^2 \tag{4.13}$$

where x, the distance from the nucleus along the ionic trajectory is defined by difference of the path length T and the distance t the ion has already travelled since it reached x_0:

$$x = T - t \tag{4.14}$$

By substitution of these relationships in the relations of the previous section it is possible to find the charge state state distribution along different trajectories parallel to the comet-Sun axis. When the charge state distribution is known, the number of photons emitted along these trajectories can be calculated:

$$S_{30.4}(x) = N_{III}(x) \cdot \left(\rho_m(x)\sigma_{2p} + \rho_H(x)\varsigma_{2p}\right) \tag{4.15}$$

$$S_{58.4}(x) = N_{III}(x)\rho_m(a)\sigma_{1s2p} + N_{II}(x) \cdot \left(\rho_m(x)\sigma_{1s2p} + \rho_H(x)\varsigma_{1s2p}\right) \tag{4.16}$$

where all the cross sections are state selective cross sections and where the parameter used is x (the distance from the comet along the ionic trajectory) in order to simplify comparison between the different trajectories.

We now return to the observer travelling parallel to the comet-Sun axis. The observed intensity of the two emission lines can now be found by integrating these source functions over the line of sight. Because the observed plane is symmetric with respect to the comet-Sun axis, multiplication with a factor of two is required.

$$I_a = 2 \cdot \int_0^R S_a(l)dl \tag{4.17}$$

4.2.2 Computer Model

In order to calculate the helium line emission for different comets, a computer program was written in MatLab. The program consists of four parts:

1. The first part contains the differential equations with the cometary density;
2. The second part solves these equations and gives the charge state distribution for a given impact parameter b;
3. The third part then calculates the source function using the relations given above;
4. The last step is to do this for all possible impact parameters b and to perform the radiative transfer integration along the line of sight.

Because of the numerical approach, the integration along the line of sight (equation 4.17) boils down to a summation:

$$I_a = 2 \cdot \sum_{i}^{R} S_{a,i} \Delta b_i \tag{4.18}$$

where Δb is the size of the iteration step between two successive impact parameter. This summation was computed using the trapezoidal routines provided by MatLab.

The model is tested by assuming a uniform density in the coma. In that case, the set of differential equation resulting can be solved analytically. Because the rate of decay is now constant along the ionic trajectory, the problem is now similar to radiative decay chains from nuclear physics:

$$N_{III}(t) = \exp\left[-n\sigma_{sec}t\right] \tag{4.19}$$

$$N_{II}(t) = \frac{\sigma_{sec} \cdot \left(\exp\left[-n(\sigma_{sec} + \sigma_{dec})t\right] - \exp\left[-n\sigma_{seq}t\right]\right)}{\sigma_{seq} - \sigma_{dec} - \sigma_{sec}} \tag{4.20}$$

In order to test the accuracy of the summation, the ionic column densities will first be calculated analytically and then numerically. The analytic solution of the He^{2+} and He^{+} column densities can be found by integrating over the comet-Sun axis:

$$C_{III}(T) = 2 \cdot \int_0^{|x_0|} N_{III}(t)dt \tag{4.21}$$

It is found that in both cases the summation is within 0.5% of the analytic solution so that it can be concluded that the routine is very accurate.

4.3 Model Results

4.3.1 Halley Model

In order to demonstrate the working of the model, comet Halley will be used to fix the parameters of a standard cometary model. At the time of the Giotto encounter (next section), Halley was approximately 1 A.U. from the Sun and the comet had a gas production rate of $Q = 10^{29}\mathrm{s}^{-1}$ of which 10% CO. The velocity of the solar wind ions as measured by the Giotto probe was ca. 300 km/s [65]. Figure 4.5 shows the density for a Halley-like comet along ionic trajectories with different impact parameters. Shown are the distribution of molecules and atomic oxygen and the distribution of hydrogen atoms. Comparing the lines at the bottom of the figure, it can be seen that ions moving through the outer parts of the comet see an almost

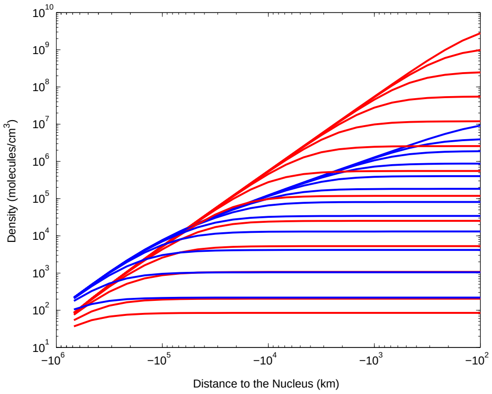

Figure 4.5: Density along ionic trajectories for different impact parameters between 10^2-10^6 km. Red is the number density of molecules and oxygen atoms, blue lines are for the number density of atomic hydrogen.

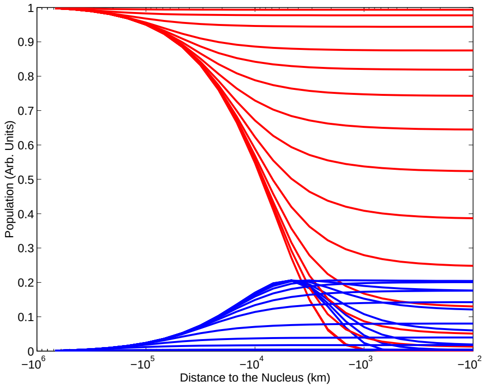

Figure 4.6: Calculated charge state distribution for different ionic trajectories. Red lines are for He^{2+} and blue lines are for He^{+}.

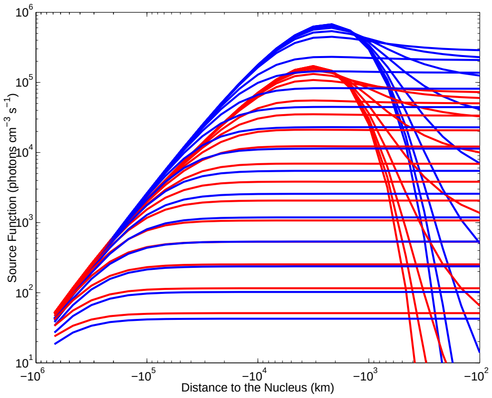

Figure 4.7: Source functions for different ionic trajectories. Red is for the 30.4 nm line due to SEC; blue is for the 58.4 nm line due to SEQ and DEC.

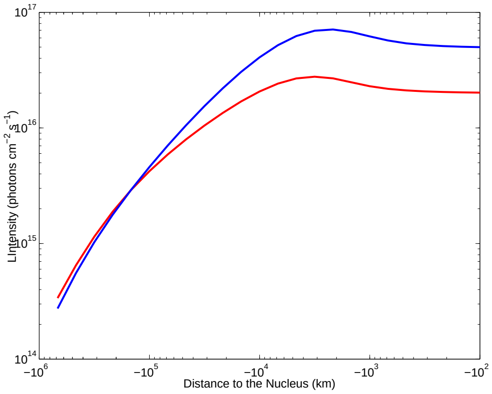

Figure 4.8: Intensity resulting from integration along the line of sight. Again, red is for the 30.4 nm and blue for the 58.4 nm emission.

constant distribution of mainly atomic hydrogen. Ions that move along a trajectory with a small impact parameter quickly pass through the atomic hydrogen zone and will encounter a rapidly increasing number of molecules. The second program calculates the charge state distribution of the helium as a function of the impact parameter. Resulting HeIII and HeII populations are shown in Figure 4.6. Only at small impact parameters, the density is high enough to neutralize all helium ions; the HeII population can be seen to rise and fall again (due to charge transfer to HeI). It can also be seen from the figure that ionic trajectories with very large impact parameters only skim the coma and almost all of the helium remains fully stripped.

The third step was then to calculate the source function, which is the product of the charge state distribution and the density. It is shown in Figure 4.7 for the emission at both 30.4 and 58.4 nm. Notice that for ions flying along trajectories near the cometary nucleus, the source function reaches a maximum and then falls down rapidly because of the depletion of the population involved. Once again, at larger distances from the nucleus much less reactions take place and the source function is much less variable.

The final step is the numerical integration over the line of sight: the resulting luminosity profile along the comet-Sun axis is shown in Figure 4.8. The area under the graph determines the total (2D) luminosity; in this case, the luminosities of the 30.4 and 58.4 nm emission would be $1.73 \cdot 10^{21}$ and $2.36 \cdot 10^{21}$ respectively, so that the line emission ratio is 0.73.

4.3.2 Emission from Different Comets

In the previous sections, comet Halley was used to illustrate the characteristics of the charge exchange model. The model contains a number of parameters; some of them describe the solar wind, such as the composition, charge state distribution and velocity. In this section the influence of the comet's characteristics to the helium line emission will be explored.

In the model, comets can be distinguished by three different free parameters:

- **Heliocentric Distance** D The distance to the Sun has a twofold effect on the emission; the closer a comet comes to the Sun, the smaller the scale lengths of the different cometary molecules will be as the flux of solar UV photons increases with the square of the distance to the Sun. At the same time, this quadratic relation also holds for the solar wind flux. In the model, D is varied from 0.5 and 5 A.U.

- **Gas production rate** Q The number of molecules sublimating from the nuclear surface strongly depends on the heliocentric distance, but

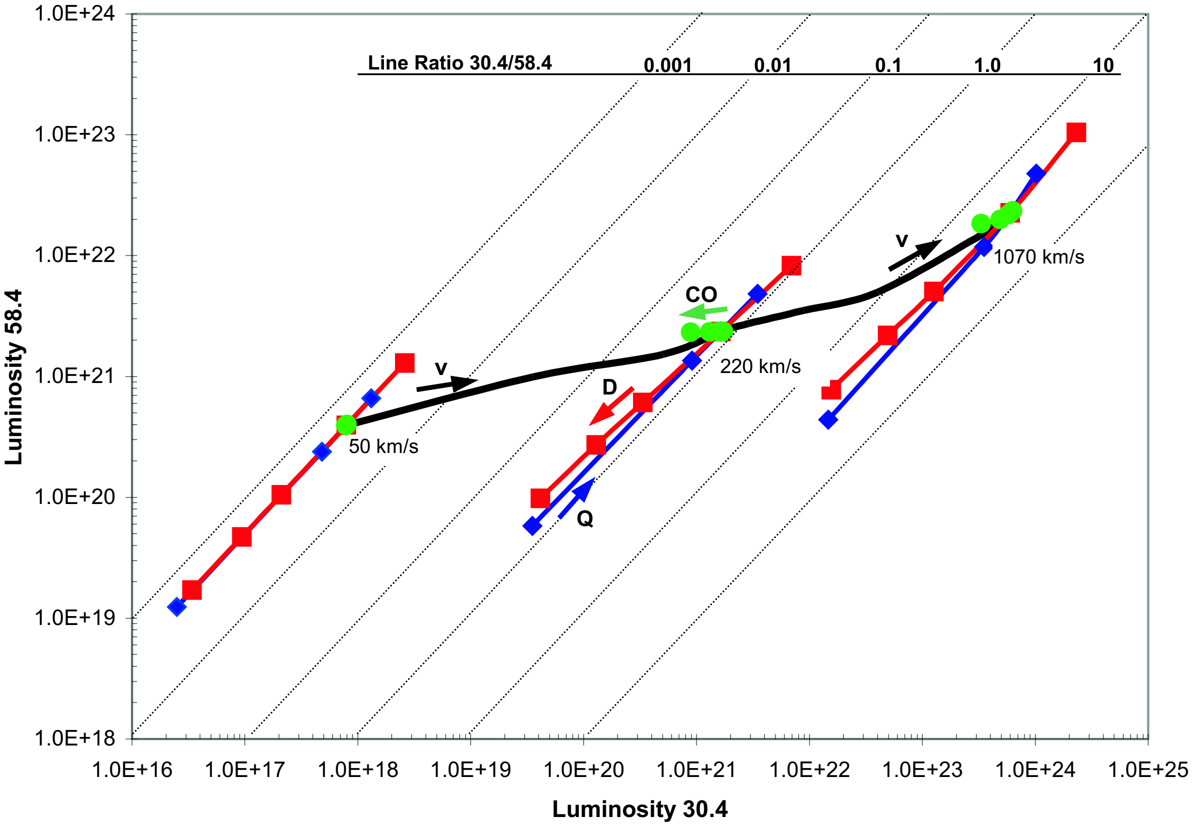

Figure 4.9: The contribution of the gas production rate Q (blue diamonds), the heliocentric distance D (red squares) and the percentage CO (green circles) on the line emission for different ionic velocities. The diagonals indicate different line emission ratios and the parameter variability is shown for three different ionic velocities. The black solid line indicates the velocity dependence of the line ratio for Halley. Luminosity is given in photons cm^{-3} s^{-1}.

it also varies strongly amongst different comets. For comets within 3 A.U. of the Sun, the total gas production rate is typically of the order $10^{28} - 10^{31}\mathrm{s}^{-1}$.

- **Composition** The exact composition is different for every comet. For the model, it is only important to distinguish between collision partners that support both single and double electron capture ('molecules') or just single electron capture (atomic H). The destruction of water produces H; CO molecules have a much larger scale length so they can reach the outer regions of the coma intact. In the model, the relative abundance of CO in the coma is one of the free parameters (0-100%).

The contribution of each of these three parameters, compared to the contribution of the solar wind velocity is summarized in Figure 4.9. The central black line shows the effect of increasing the ionic velocity from 50 km/s to 1070 km/s. Over this velocity range, the luminosity of the 30.4 nm line changes with six orders of magnitude while the luminosity of the neutral helium line changes only with two orders of magnitude. The velocity line can be seen to cross several of the diagonal lines, that indicate different line ratio values. It can therefore be concluded that the line ratio is strongly dependent on the velocity and that this dependence mainly is an effect of the HeII 30.4 nm line.

Red and blue lines show the effect of changing the heliocentric distance or the gas production rate, respectively. It can be seen that changing these parameters mainly effects the absolute luminosity, but as these lines are almost parallel to the diagonals it can also be seen that the line ratio is not affected. With increasing gas production rate Q, the density of the cometary gas increases and hence the size of the interaction region of the solar wind with the coma increases. However, both lines are affected similarly; they both scale linearly with Q.

The effect of changing the distance to the Sun is more complex, as it contained two components, the increasing solar wind flux but also the more rapid destruction of molecules. The increase in the solar wind flux affects both lines by the same amount. The molecular scale lengths have only a small effect and change the line ratios slightly.

Finally, the effect of the composition (green lines) has a negligible effect on the luminosities. However, increasing the CO abundance decreases the line ratio almost along the velocity axis; it is suggested by the figure that underestimating the long-lasting molecular content leads to only a small underestimation of the velocity.

It can thus be concluded that the line ratio 30.4/58.4 nm is determined mainly by the velocity of the helium ions with a small dependence on the

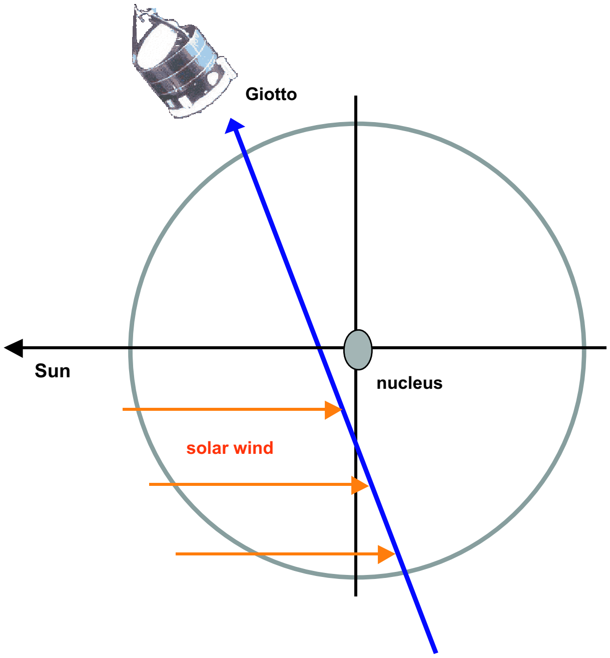

Figure 4.10: Schematic view of Giotto's path through comet Halley. The probe's trajectory is indicated by a blue arrow. Solar wind trajectories are indicated by orange lines.

composition and that the luminosity of the emission is determined by Q and D. Hence, the 2-D model is expected to work well for line emission ratios but not for absolute luminosities. Currently, the model can be used to derive velocities from line ratios.

4.4 Giotto Measurements

In March 1986, six spacecraft flew through comet Halley. The closest approach was made by the Giotto probe, which passed Halley's nucleus at a distance of 536 km. From observations by the Ion Mass Spectrometer on board Giotto, the distribution of HeIII and HeII along the satellite's trajectory is known.

In the original articles by Shelley *et al.* [66] and Fuselier *et al.* [19], an attempt was made to interpret the observations by means of a model that included only single electron capture by HeIII. The percentage 'charge exchanged helium', which is the ratio of number of HeII ions to the sum of both HeII and HeIII ions was used as a probe to determine the number of charge exchange reactions in the coma. The predicted ionic concentrations however were not in agreement with the observations as the predicted increase of charge exchanged helium is much smaller than the observed increase.

These models included only one single electron capture by HeIII. It was already shown before that single electron capture from molecular targets is not the only process that is relevant to the fractions of HeIII and HeII. Double- and sequential capture from both molecular and atomic targets will probably have an important role in the charge state distribution.

In order to investigate the effect of the different electron capture processes on the charge state distribution, one should bear in mind that the geometry of the measurements done by Giotto is rather different from the geometry used in the sections before. In the previous sections, ions were followed while approaching the nucleus along the comet-Sun axis. The trajectory of Giotto however has an angle of 73° with this axis. A global picture of the situation is shown in Figure 4.10.

From the picture, it can be seen that solar wind ions have already travelled a long way through the coma before they are picked up by Giotto. The number of possible collision partners met by an ion at a certain distance r from the nucleus is therefore much larger along the Giotto trajectory than the number of particles along the comet-Sun axis. A goniometric approximation to this problem is given in Appendix B.

The results of the model are shown in Figure 4.11. For comparison, the results of the earlier model are also shown. The percentage charge exchanged helium was calculated for a constant ionic velocity (0.5 keV/amu or 300 km/s) which corresponds to the ionic velocity that was measured with Giotto by Goldstein *et al.* [65]. The model does not take into account that the ions are decelerated along their path.

Up to a distance of $2 \cdot 10^5$ km, both models accurately describe the charge state distribution. This can be easily understood: the outer region of the comet consists of mainly atomic hydrogen and its density is far too low to allow for sequential capture. From the observations, a sudden jump in the ratio occurs at $2 \cdot 10^5$ km which is due to a magnetic pile up boundary. Even without the inclusion of detailed plasma physics, the model already predicts a rapid increase of the percentage charge exchanged helium as the cometary density increases rapidly in this region.

4.5 Helium Line Observations in Comets

For a small number of comets, FUV spectra are available from the EUVE satellite, which was switched off early 2001. Helium line emission was observed in the comets Hale-Bopp and Hyakutake. A summary of the observa-

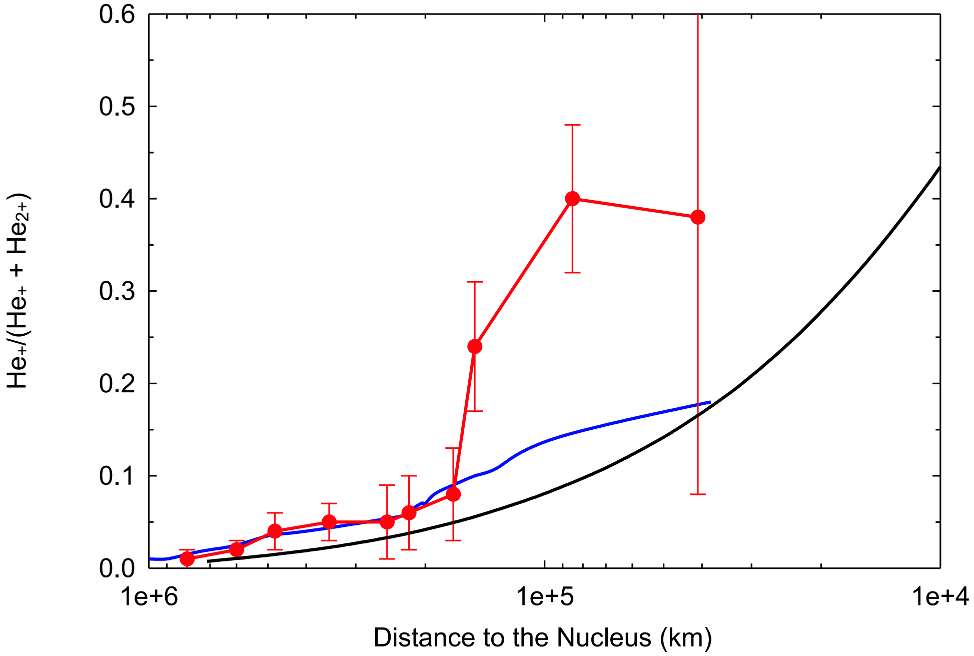

Figure 4.11: Percentage charge exchanged helium as a function of the distance of the measurement probe to the nucleus. The model was calculated with a constant velocity of 0.5 keV/amu. Red dots are the Giotto measurements from Shelley *et al.* [66]; the blue line is for the cometary model by Fuselier *et al.* [19]

tions can be found in Table 4.1.

4.5.1 Hale-Bopp

Spectral observations of comet Hale-Bopp were done by Krasnopolsky *et al.* [30]. Hale-Bopp was observed using EUVE from 14 to 19 September 1996 when it was still far away from the Sun (3 A.U.). At this distance, CO makes up for an important part of the gas produced. The properties and observations of Hale-Bopp are summarized in Table 4.1. In order to reproduce the observation as accurate as possible, the line ratio was calculated for the region within the given aperture of $2.5 \cdot 10^5$ km centered at the cometary nucleus.

Two helium lines were observed: the HeI (1s2p-1s^2) line at 58.4 nm and the HeI (1s3p-1s^2) line at 53.7 nm. For the 30.4 nm line by HeII (2p-1s), an 2σ upper limit was determined. The ratio between the luminosity at 30.4 and 58.4 nm is ≤ 0.58.

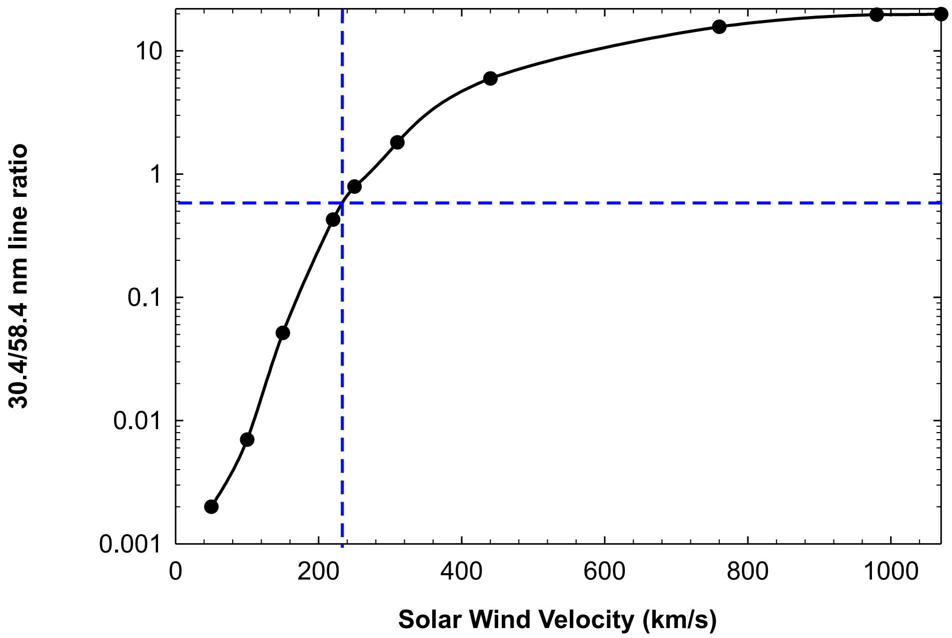

Figure 4.12: Hale-Bopp, line emission ratio for different solar wind velocities. The observed line emission ratio of 0.58 is indicated. The line is drawn to guide the eye.

The results of the model for Hale-Bopp are shown in Figure 4.12. The line emission ratio has been calculated for constant velocities between 50 and 1070 km/s. Assuming a constant velocity throughout the coma, a velocity of ca. 220 km/s is found for the helium ions.

In the real comet, the velocity of the incoming ions will not be constant but the ions will be decelerated. Looking again at Figure 4.12, it can be seen that lowering the velocity pulls the ratio down. This implies that the velocity derived from the model must be a minimum initial velocity.

				Luminosity (photons s^{-1})		
Comet	Q (s^{-1})	D(A.U.)	CO (%)	30.4 nm	58.4 nm	53.7 nm
Hale-Bopp	$6 \cdot 10^{29}$	3.07	30	$\leq 7 \cdot 10^{25}$	$1.2 \cdot 10^{26}$	$2.1 \cdot 10^{25}$
Hyakutake	$2 \cdot 10^{29}$	1.07	5	$7.3 \cdot 10^{24}$	$\leq 10^{24}$	

Table 4.1: Helium line emission in comets. Observational details and cometary characteristics during the observations for Hale-Bopp (Krasnopolsky *et al.* [30],Biver *et al.* [8]) and Hyakutake (Krasnopolsky *et al.* [31]).

Unfortunately, the current model only predicts the luminosity from the plane through the comet-Sun axis. It is therefore not possible to compare the predicted luminosity with the observed luminosity. For the 2D situation, the model predicts luminosities of $7.80 \cdot 10^{19}$ photons s^{-1} at 30.4 nm and $1.82 \cdot 10^{20}$ photons s^{-1} at 58.4 nm.

Another interesting feature is the emission at 53.7 nm. The observed flux is a blend of O^+ and HeI emission and it was estimated by Krasnopolsky **??** that 60% of the flux was due to oxygen. The rest of the flux was attributed to the HeI $(1s3p - 1s^2)$ transition, Table 4.1.

In collisions between HeII and atomic hydrogen or molecules, the $(2p)$ state is the highest level populated. Although theory predicts capture into the $(3l)$ states, experiments with HeIII colliding on CO or H_2 show no population of the HeI $(1s3p)$ state [46].

Although this is a rough observation, it is possible to reverse the argument, estimating the cross section for double electron capture from a molecular target required to produce the observed flux at 53.7 nm. From Figure 3.10, the cross section for double electron capture into the $(1s2p)$ state is more or less constant at $0.5 \cdot 10^{-16}$ cm^2. From the ration between the luminosities, a maximum for the cross section for state selective electron capture into the $(1s3p)$ state is then $2.1 \cdot 10^{25}/1.2 \cdot 10^{26}$ or 18% of the cross section for double capture into the HeI$(1s2p)$ state. This yields a cross section of $9 \cdot 10^{-18}$ cm^2 at a velocity of approximately 0.25 keV/amu.

Looking again at the experiments, this small cross section explains the absence of emission at 53.7 nm in our experimental spectra. The number of photons emitted at 53.7 nm is approximately 18% of the emission at 58.4 nm. This implies that the intensity of the 53.7 nm line is too low to be seen in the spectra currently obtained in the experiments.

4.5.2 Hyakutake

Hyakutake was observed by Krasnopolsky *et al.* [31] using the EUVE observatory between March 21 and March 25 1996. During the observations, the main difference with comet Halley was its lower gas production rate [31, 67]. The instrument aperture was $1 \cdot 10^5$ km, centered on the cometary nucleus.

The helium line at 30.4 nm was observed with a luminosity of $7.3 \cdot 10^{24}$ photons s^{-1}, much smaller than the upper limit observed in Hale-Bopp. No line emission was detected at 58.4 nm and an 1σ upper limit of 10^{24} photons/s was acquired from the spectrum given in the article.

The non-detection of the 58.4 nm suggests that the helium ions were initially part of a fast solar wind stream, as is shown in Figure 4.13. From the figure, it can be seen that in order to produce a luminosity at 30.4 nm that is three

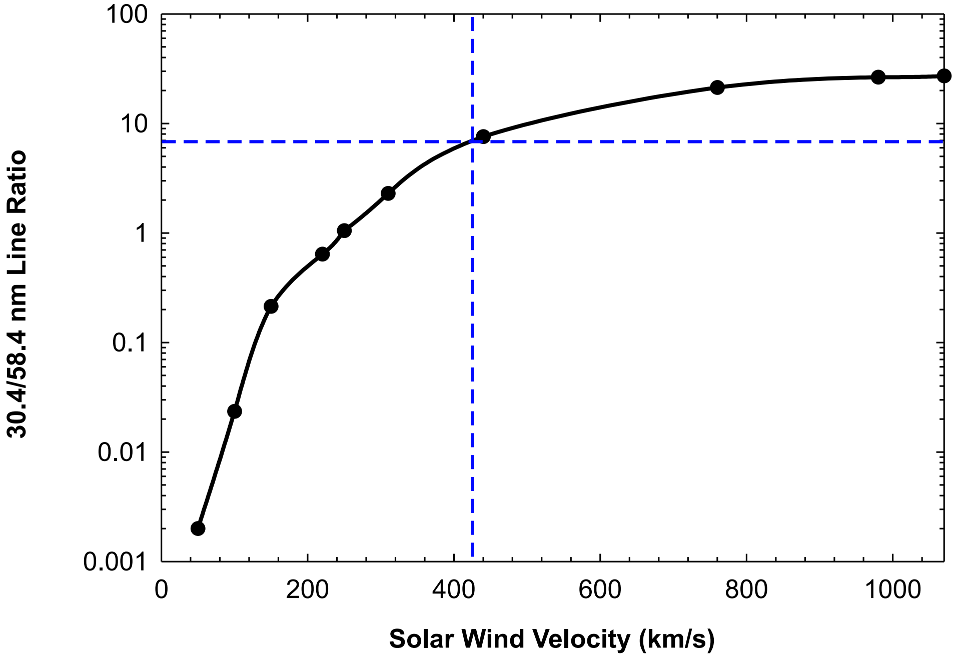

Figure 4.13: Hyakutake, line emission ratio for different solar wind velocities. The observed line emission ratio of 7.0 is indicated. The line is drawn to guide the eye.

times higher than the luminosity at 58.4 nm, a velocity of 0.5 keV/amu is already required. Following the argumentation for comet Hale-Bopp, the velocity at 10^5 km from the nucleus (the size of the aperture) must be lower than the initial velocity of the ions. This results in a line ratio of 7, which corresponds to a velocity of 425 km/s.

4.6 Discussion

The first test of the model was the comparison with in situ measurements by the Giotto probe of the charge state distribution inside comet Halley. The predicted charge state distribution agreed well with the measurements, although it should be taken into account that the complexity of the plasma physics involved does not allow for a detailed comparison of the inner regions of the comet.

A second test is the comparison with FUV observations. Recalling Table 4.1, the detected He^+ luminosity measured in Hyakutake is smaller by one order of magnitude than the He^+ luminosity measured in Hale-Bopp. From the

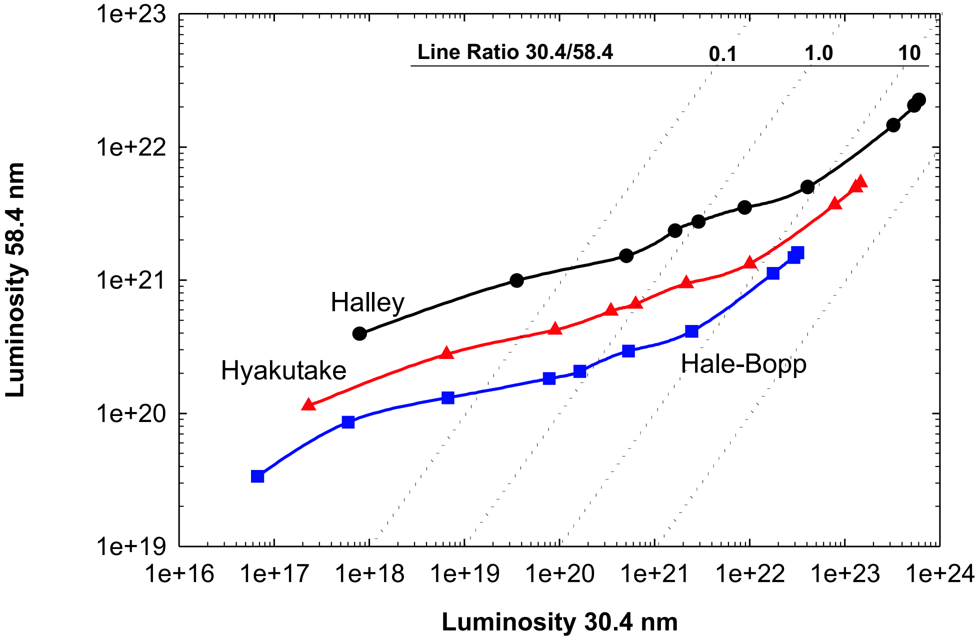

Figure 4.14: Luminosity plot for different comets assuming different solar wind velocities. The parameters given in Table 4.1 are used; comet Halley (black dots), Hale-Bopp (blue squares) and Hyakutake (red triangles). The lines are drawn to guide the eye.

luminosity plot in Figure 4.14, this is not expected. The model predicts that this is only possible if the ions interacting with Hyakutake were much slower than the solar wind interacting with Hale-Bopp. This is contrary to the expectation of a line ratio larger than one, suggested by the none detection of the neutral helium line as this would lead to a luminosity higher than the luminosity observed for Hale-Bopp.

In the same observations, Krasnopolsky also measured the soft X-Ray luminosity. For the photons with energies between 97 and 165 eV, the luminosities of Hale-Bopp and Hyakutake were $8 \pm 2 \cdot 10^{24}$ and $1 \pm 0.2 \cdot 10^{25}$, respectively. This confirms the results of the model: Hyakutake produces more X-Ray photons than Hale-Bopp.

In the model, the comet was assumed to be optically thin so that all the light produced contributes directly to the luminosity. This is true for X-Ray photons, but not for EUV photons that can be absorbed by various molecular dissociation and ionization processes. When the observational geometry is taken into account, the lower observed FUV luminosity of Hyakutake can be

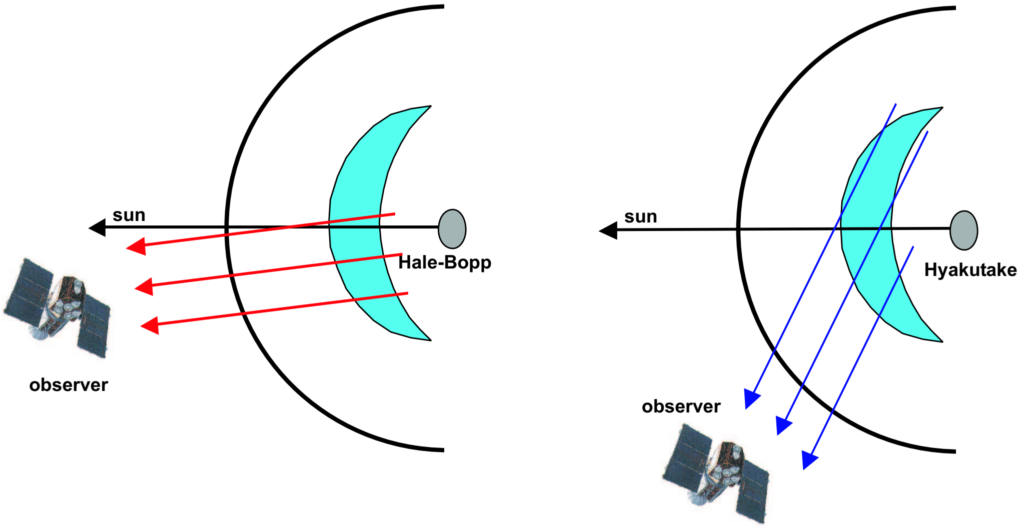

Figure 4.15: Observational geometry. Hale-Bopp was observed almost up front; Hyakutake was observed under a much larger angle.

understood.
The geometry was rather different for the two comets, see Figure 4.15. Hale-Bopp was observed from with a phase angle of 19°; in the case of Hyakutake, the phase angle was 50°. Photons observed under a large phase angle will have to travel through regions with higher molecular densities than photons observed with a small phase angle. Using the photo destruction data for water by Huebner *et al.* [10], it can be estimated that the process of absorbtion of a photon from one of the helium transitions by a water molecule has a cross section of approximately $\sigma = 10^{-16}$ cm^2. It can therefore be expected that the dense region within the crescent shape has a significant effect on the optical depth. This effect will be studied in more detail once the model can be used to calculate absolute intensities.

Chapter 5

Cometary Charge Exchange Spectra

The study of state selective electron capture by heavy ions has a rich history at the KVI as the institute was the first to have an ECR ion source facility. The work of several Ph.D. students over the last twenty years has yielded a wealth of data regarding the velocity dependence of state selective charge exchange in a large variety of collision systems [45, 57, 46].

The launch of the Chandra and XMM observatories made it possible to obtain cometary X-Ray emission with a resolution high enough to identify different spectral lines. It has already been shown how electron capture by helium ions leads to emission in the ultraviolet regime. In this chapter, a model is presented that predicts the X-Ray emission from charge exchange by the heavier ions that are present in the solar wind.

Unlike the helium model, the cometary environment is left behind in the heavy ion model. Similar work was done by both Kharchenko and Dalgarno *et al.* [34, 35] and Schwadron and Cravens *et al.* [25] have made detailed predictions of cometary X-Ray spectra. A dependence on the solar wind type was introduced by means of the solar wind composition. Both use velocity independent cross section data and statistical (n, l) distributions. The model by Kharchenko and Dalgarno focusses at the atomic model, whereas the model by Schwadron and Cravens uses simplified atomic physics.

In the model presented here, the dependency of state selective cross sections on the projectile velocity is combined with compositional changes of the solar wind as a function of velocity.

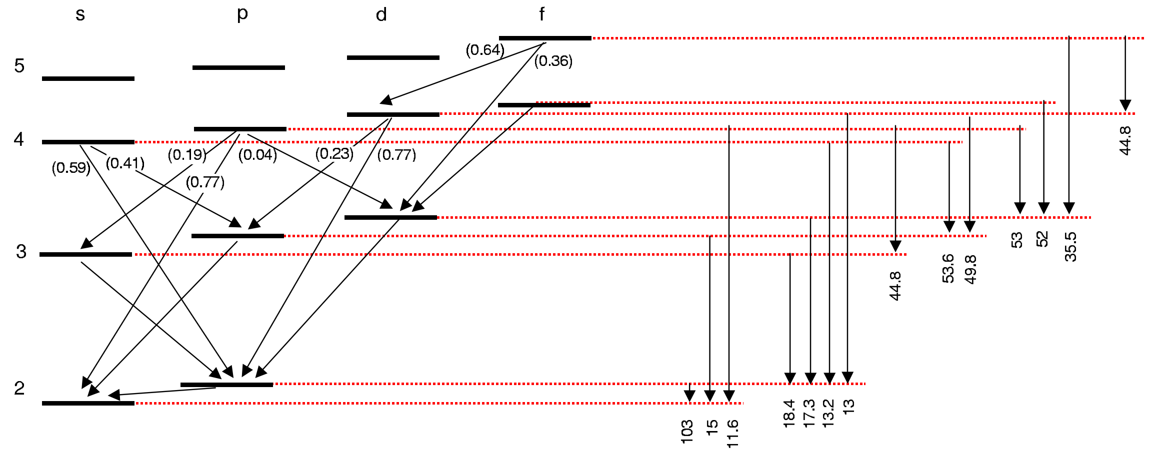

Figure 5.1: Transition scheme of OVI with the most relevant transitions indicated. The left part of the figure gives the branching ratios; the right part gives the transition wavelengths in nm. Data taken from [68, 69].

5.1 Electron Capture by Heavy Ions

In low energy collisions between multiply charged ions and neutral targets single electron capture dominates in most systems over other possible processes such as double electron capture or ionization. As was discussed for helium before, SEC might leave the electron in an excited state. When the ion relaxes, this leads to emission of one or more photons. In the case of highly charged ions, these photons typically have energies in the Far UV or X-Ray regime. This will be illustrated by the following example[1]:

$$O^{6+} + H_2 \rightarrow O^{5+}(nl) + H_2^+ \tag{5.1}$$

Collisions with O^{6+} are very important in the context of comets and the solar wind; O^{6+} is the most abundant heavy ion in the solar wind. The capture of an electron turns it into OVI, which has three electrons and therefore has a lithium-like electron configuration with ground state ($1s^2 2s$). The transition scheme of OVI is shown in Figure 5.1. From the transition scheme, it can be seen that relaxation of excited states occurs in the Far Ultraviolet or soft X-Ray regime[2].

State selective cross sections for collisions between O^{6+} and molecular hydrogen have been measured by Dijkkamp *et al.* [40] and Lubinski *et al.* [46].

---

[1] In an attempt to avoid confusion, the superscript notation O^{7+} is used for the initial ions and the spectroscopic notation OVIII is used for reaction products

[2] X-Ray wavelengths are between 0.01-10 nm; UV wavelengths are between 10-400 nm

The results of these experiments roughly confirm the predictions by the extended Over-the-Barrier model as capture mainly occurs in the $(4l)$ states. From the reaction window, it is to be expected that the $(4f)$ state should be the most popular state; this effect should even get stronger at low velocities. The measurements show that this applies at 6 keV/amu, but that at low velocities this is not the case because the $(4s)$ and $(4p)$ states are populated the most. Although the Over-the-Barrier model is a good tool for understanding electron capture processes, it cannot be used to reliably predict the ionic (nl) distribution.

We will now go back to the solar wind and follow an O^{6+} ion as it collides with a molecule in the cometary coma. To investigate the role of the ionic velocities, we will consider the two extremes of solar wind velocity and give the ion an initial velocity of either $\sim$ 200 km/s (slow wind) or $\sim$ 1070 km/s (fast wind) or equivalently 0.2 respectively 6.0 keV/amu. Lower velocities that may be caused by deceleration in the coma are not considered here, as only very limited experimental or theoretical data is available for those velocities.

Table 5.1 gives the state selective cross sections measured at those velocities and from these figures, the probability that an electron is captured in a certain (nl) state is known. Suppose our oxygen ion is fast; it will probably capture an electron in the $(4f)$ state. In this case, the quantum mechanical selection rule $\Delta l = \pm 1$ allows only one relaxation path to the ground state $(2s)$:

$$(4f) \rightarrow (3d) + 52 \text{ nm} \rightarrow (2p) + 17.3 \text{ nm} \rightarrow (2s) + 103 \text{ nm} \tag{5.2}$$

Electron capture into the $(4f)$ state thus leads to the emission of three photons, of which two are emitted within the wavelengths of our interest. If the electrons were captured into the $(4s)$ state, which is typical for slow wind,

	Slow wind		Fast wind	
(nl)	$\sigma(\text{cm}^2)$	%	$\sigma(\text{cm}^2)$	%
4s	1.32E-15	36	2.80E-16	11
4p	1.50E-15	41	5.10E-16	20
4d	3.09E-16	8	6.00E-16	24
4f	5.29E-16	14	1.05E-15	42
5f	-	-	6.00E-17	0.02

Table 5.1: tate selective cross sections for SEC by O^{6+} colliding on H_2. Cross sections for slow wind (0.25 keV/amu) are taken from Lubinski *et al.* [46], the data for fast wind (6.0 keV/amu) is taken from Dijkkamp *et al.* [40]

two cascades are possible:

$$(4s) \rightarrow \begin{cases} (3p) + 53.8 \text{ nm} \rightarrow & (2s) + 15 \text{ nm} \\ (2p) + 13.2 \text{ nm} \rightarrow & (2s) + 103 \text{ nm} \end{cases} \tag{5.3}$$

Here, 41% of the decay occurs along the first track; 59% along the second one. A third route through the relaxation scheme does exist; from the selection rules, a transition from the $(3p)$ to the $(3s)$ state is allowed. This transition however has a branching ratio of 0.002 and can therefore be neglected.

In both the slow and the fast solar wind, electrons will be captured in any of the $(4l)$ angular momentum states. Emission lines from the two cascades in equation 5.2 and 5.3 will follow the presence of O^{6+} in the solar wind, regardless its velocity. The intensity of these lines however is coupled to the velocity of the solar wind.

5.1.1 Multiple Electron Capture

Like helium, heavy ions can capture more than one electron from collisions with molecular targets. However, dominance of double electron capture over single electron capture is very rare.

Multiple electron capture is often followed by auto ionization or the emission of an Auger electron. The electrons are captured in an energy level that is generally lower than those resulting from SEC. Typically, multi electron capture results in a significant contribution of the Ly-α line.

In the model presented here, multiple electron capture by heavy ions is not included.

5.1.2 Singlet and Triplet Population

In the case of electron capture by O^{6+}, the OVI ion will always end up in the doublet spin state, because the ground state of O^{6+} is $^1S_0$.

However, if we would consider electron capture by for example O^{7+} (one electron), the resulting OVII ion (two electrons) could end up either in the singlet or in the triplet configuration. In the case of the solar wind, this concerns electron capture by O^{7+}, N^{6+} and C^{5+}.

It is often assumed that the distribution over singlet and triplet states after single electron capture is statistical. AGORA measurements by Lubinski *et al.* [46] suggest that this singlet to triplet ratio is velocity dependent. For simplicity, the statistical ratio of 1:3 is assumed in this work.

	1s	**2s**	**2p**	**3s**	**3p**	**3d**	**4s**	**4p**	**4d**	**4f**	**5s**	**5p**	**5d**	**5f**	**5g**
1s	0	0	0	0	0	0	0	0	0	0	0	0	0	0	0
2s	0	1	1	0	1	0	0	0.77	0	0	0	0	0	0	0
2p	0	0	0	1	0	1	0.59	0	0.77	0	0	0	0	0	0
3s	0	0	0	0	0	0	0	0.19	0	0	0	0	0	0	0
3p	0	0	0	0	0	0	0.41	0	0.23	0	0	0	0	0	0
3d	0	0	0	0	0	0	0	0.04	0	1	0	0	0	0.64	0
4s	0	0	0	0	0	0	0	0	0	0	0	0	0	0	0
4p	0	0	0	0	0	0	0	0	0	0	0	0	0	0	0
4d	0	0	0	0	0	0	0	0	0	0	0	0	0	0.36	0
4f	0	0	0	0	0	0	0	0	0	0	0	0	0	0	0
5s	0	0	0	0	0	0	0	0	0	0	0	0	0	0	0
5p	0	0	0	0	0	0	0	0	0	0	0	0	0	0	0
5d	0	0	0	0	0	0	0	0	0	0	0	0	0	0	0
5f	0	0	0	0	0	0	0	0	0	0	0	0	0	0	0
5g	0	0	0	0	0	0	0	0	0	0	0	0	0	0	0

Table 5.2: Transition matrix for OVI. Columns indicate initial state (nl); rows give the final state after emission of one photon.

5.2 Model

The interaction of comets and the solar wind leads to distinct spectra by the process of charge exchange, as was outlined in the previous chapter. The intensity of the emitted light depends on the solar wind ion flux and on the cometary density; the spectral distribution is determined by the composition of the solar wind and by the state selective electron capture cross sections. The state selective cross sections determine what lines are formed and what their strengths will be. The resulting spectrum thus depends on the solar wind velocity by means of its composition and by means of the velocity dependent state selective cross sections.

In order to investigate the dependence of charge exchange spectra on the solar wind velocity, a MatLab model was created that calculates emission cross sections of the photons that are emitted when the ion cascades from its excited state to the ground state. To do this, we will first introduce a matrix notation for the transition scheme, which again is illustrated by the case of electron capture by an O^{6+} ion in Table 5.2.

For each of the transitions allowed by the quantum mechanical selection rules, the branching ratio is indicated on a position $\hat{B}_{fi}$ in the transition matrix $\hat{B}$ where i and f are the initial respectively the final state of the transition. In exactly the same way, the transition wavelengths can be represented in a matrix (Appendix C). Stable states are given the value of one; transitions that are not allowed are indicated with a zero. It shall be shown that it is

essential that the matrices are square matrices; the dimensions of the matrices are determined by the highest state involved.
The state selective cross sections are represented by a column vector $\hat{C}$. This is done creating a column $[\sigma(1s), \sigma(2s), \ldots, \sigma(nl)]$ for both the slow and the fast solar wind. An example of this notation in the case of single electron capture by slow O^{6+} ions would be:

$$C = [0, 0, 0, 0, 0, 0, 1.32 \cdot 10^{-15}, 1.50 \cdot 10^{-15}, 3.09 \cdot 10^{-16}, 5.29 \cdot 10^{-16}, 0, 0, 0, 0, 0]$$

The first figure is for capture into the $(1s)$ state, the second for the $(2s)$, and so on. Note that for typographical reasons, the transpose of the column vector is shown. The cross section vector $\hat{C}$ is normalized by dividing each of the state selective cross sections by the sum of all state selective cross sections.
The initial state population is now given by the vector $\hat{C}$. The matrix $\hat{L}$ containing the number of emitted photons per transition is found by creating a diagonal matrix $\hat{E}$ from the population vector $\hat{C}$ and multiplying this matrix with the transition matrix $\hat{B}$:

$$\hat{L} = \hat{B} \times \hat{E} \tag{5.4}$$

After the emission of one photon per ion, the new population $\hat{C'}$ is given by the product of the transition matrix and the cross section matrix:

$$\hat{C'} = \hat{B} \times \hat{C} \tag{5.5}$$

Allowing for another photon to be emitted, the population will be given by $\hat{B} \times (\hat{B} \times \hat{C})$ and so on until all ions have reached a stable state and no more new photons are emitted. For each of those steps, the amount of emitted photons $\hat{L'}$ can be calculated by the product of the diagonal population matrix $\hat{E'}$ and the transition matrix $\hat{B}$ as was done in equation 5.4. The normalized sum of all emission matrices $\hat{L_n}$ over n steps yields the electron capture spectrum by one specific ion; this spectrum is expressed in units of emission cross sections by multiplication with the initial state selective cross sections.

5.3 Results

X-Ray spectra for two different wind velocities were modelled: slow wind (300 eV/amu or 240 km/s) and fast wind (6 keV/amu or 1075 km/s). A third possibility, where an initially fast wind is decelerated to slow velocities, is also explored.

In order to produce actual interaction spectra, some assumptions have to be made about the comet and the solar wind. The velocity dependent abundances of He, C, N and O in the solar wind are given in Table 2.3. O^{8+} and N^{7+} were not included in the model because their abundances are too low; ionic neon was not included because no experimental data was available to the author. For each of the solar wind ions involved, state selective cross sections for collisions with molecular hydrogen were used because for this molecule, a lot of state selective cross sections are available. From chapter 3 it is not to be expected that this affects the results as most of the cometary collision partners have similar ionization potentials. For simplicity, only one electron capture process is allowed for, so that sequential capture is excluded from the model. A more detailed overview of the ionic data used in the model can be found in Appendix C.

Electron capture spectra are shown in Figures (5.2-5.5) by means of the emission cross section, using a normalized proton flux. The number of emitted photons per unit wavelength can therefore be found by multiplication with both the solar wind flux and the cometary density. Figure (5.2) and (5.4) show spectra with observational resolutions comparable to ROSAT ($\Delta E > 25$eV) and CHANDRA ($\Delta E \approx 10$eV).

In both the slow and the fast spectrum, some distinct features are visible. The first is strong emission in the 0-150 eV region. This region contains emission lines of all ions that are included in the model. Most emission lines in this region are due to the 'small steps' through the transition scheme, typically between states where the initial and final principle quantum number $n \geq 3$. A very important feature is the presence of various forbidden lines by CV, NVI and OVII (Table 5.3) . This can be understood in terms of the transition schemes: most lines present in this spectral region are due to transitions from the lowest excited states to the ground state. The transition scheme than works as a bottleneck as all ions in the triplet state have to pass these low lying transitions to reach the ground state.

The spectral intensity decreases strongly at photon energies above 600 eV. There are only few ions that can produce emission at these wavelengths by transitions directly to the ground state, for example OVII and OVIII but also NeIX and MgXI, which have only low abundances.

Another interesting common property of the spectra is the gap between 150-300 eV. Because the energies involved are low, it is to be expected that in real cometary spectra this window is (partly) filled by emission by highly charged ions with small abundances, that are not included in this model such as Ne, Mg, Si and Fe ions.

In order to compare the role of state selective electron capture in cometary X-Ray spectra, it is interesting to consider another spectrum which will be

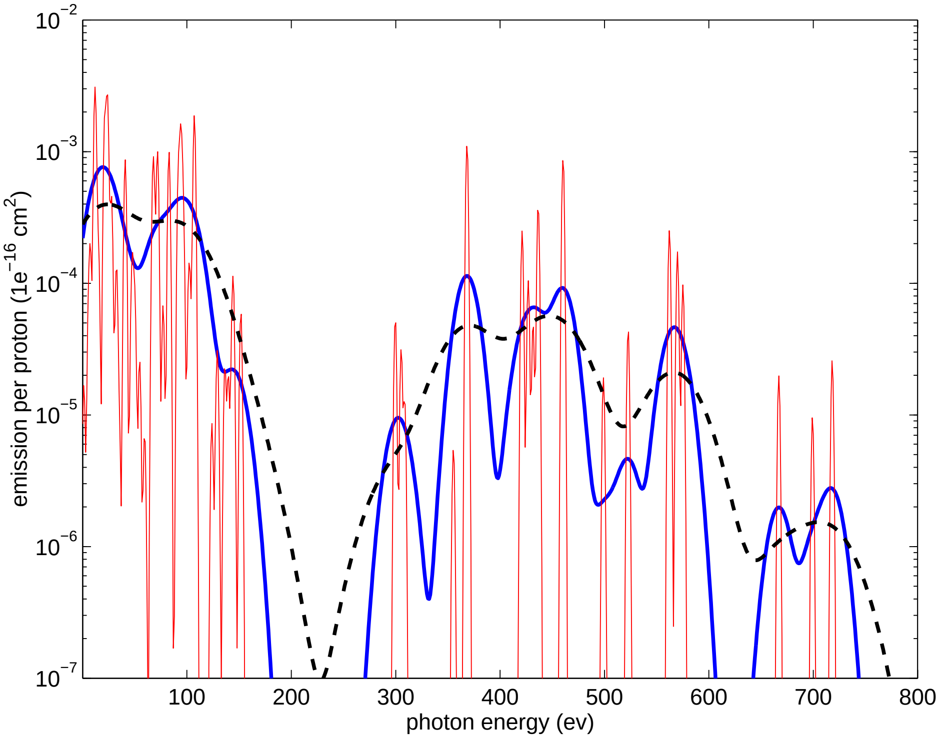

Figure 5.2: Slow solar wind spectrum for different observational resolutions. Red 1 eV; blue 10 eV; black dashed line 25 eV.

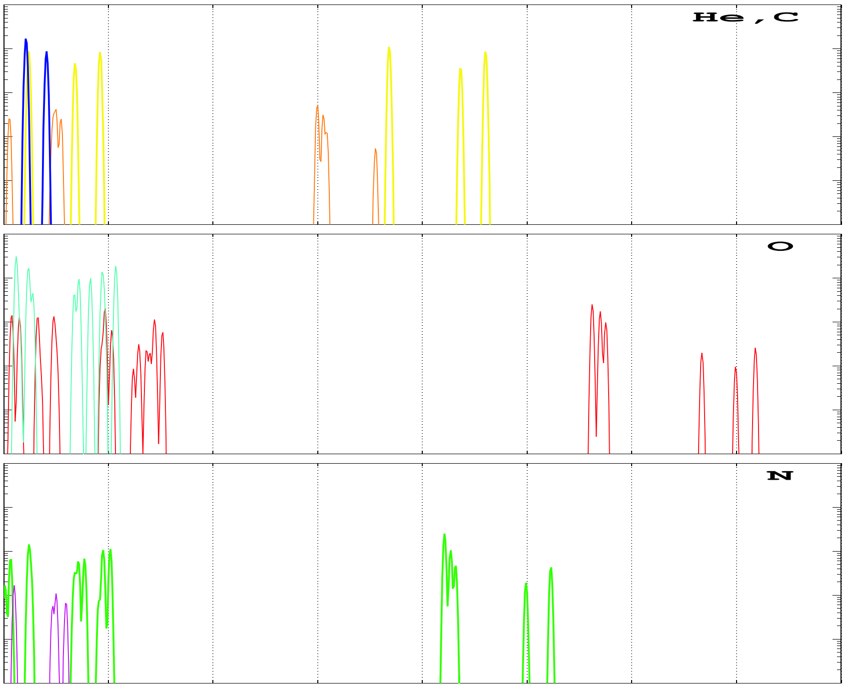

Figure 5.3: Contribution of different ions to a slow spectrum with 1 eV resolution. Blue: helium, yellow: CVI, orange: CV, red: OVII, cyan: OVI, green: NVI, magenta: NV. The scaling of the axes is similar to the previous figure.

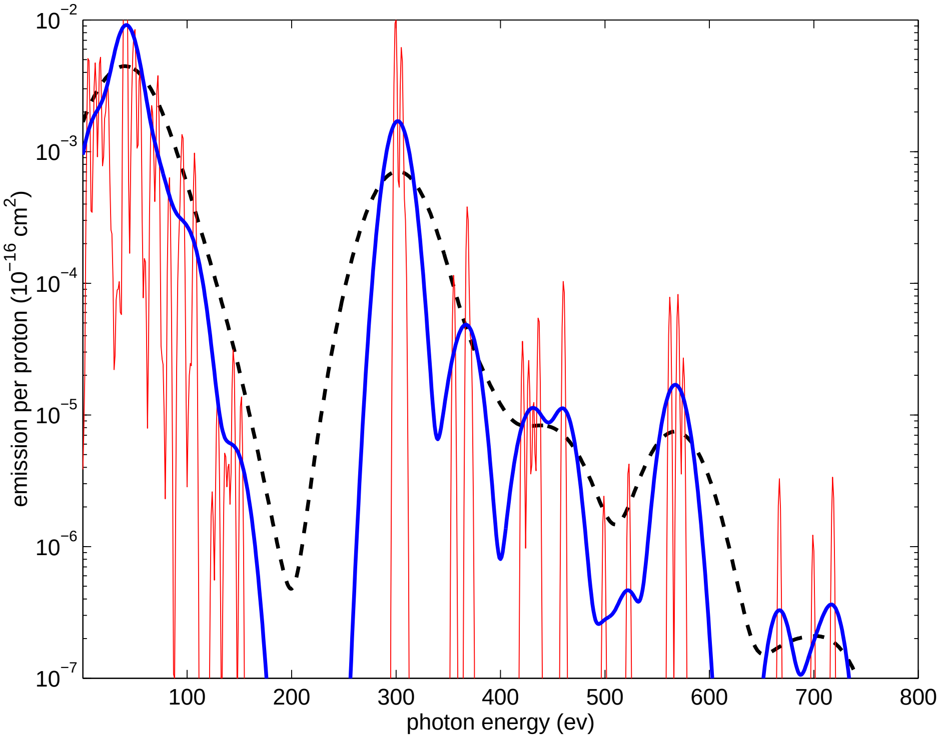

Figure 5.4: Fast solar wind spectrum for different observational resolutions. Red 1 eV; blue 10 eV; black dashed line 25 eV.

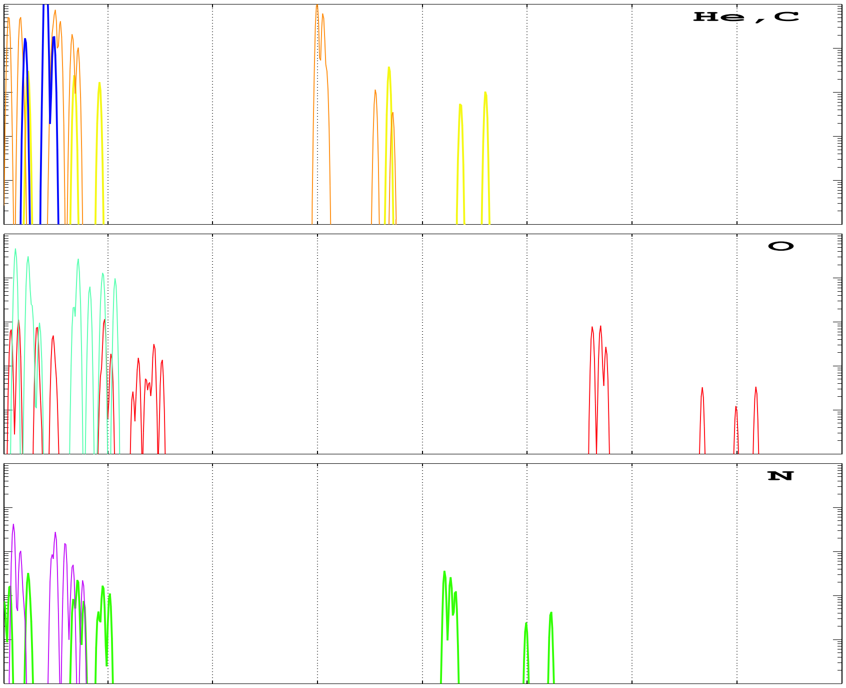

Figure 5.5: Contribution of different ions to a fast spectrum with 1 eV resolution. Blue: helium, yellow: CVI, orange: CV, red: OVII, cyan: OVI, green: NVI, magenta: NV. The scaling of the axes is similar to the previous figure.

Ion	Transition	λ (nm)	E (eV)	τ (ms)
CV	^{3}S - ^{1}S	4.15	298	21.0
CV	^{3}P - ^{1}S	4.07	304	$3.80 \cdot 10^{-2}$
NVI	^{3}S - ^{1}S	2.95	419	3.90
NVI	^{3}P - ^{1}S	2.91	425	$3.00 \cdot 10^{-3}$
OVII	^{3}S - ^{1}S	2.21	560	0.96
OVII	^{3}P - ^{1}S	2.18	568	$3.00 \cdot 10^{-3}$

Table 5.3: Forbidden lines included in the spectral model. Lifetimes are indicated by τ.

denoted as 'decelerated wind'. This wind was initially fast but by interaction with the cometary gas it is decelerated. It therefore has the composition of fast solar wind, while the cross sections used are for slow collisions.

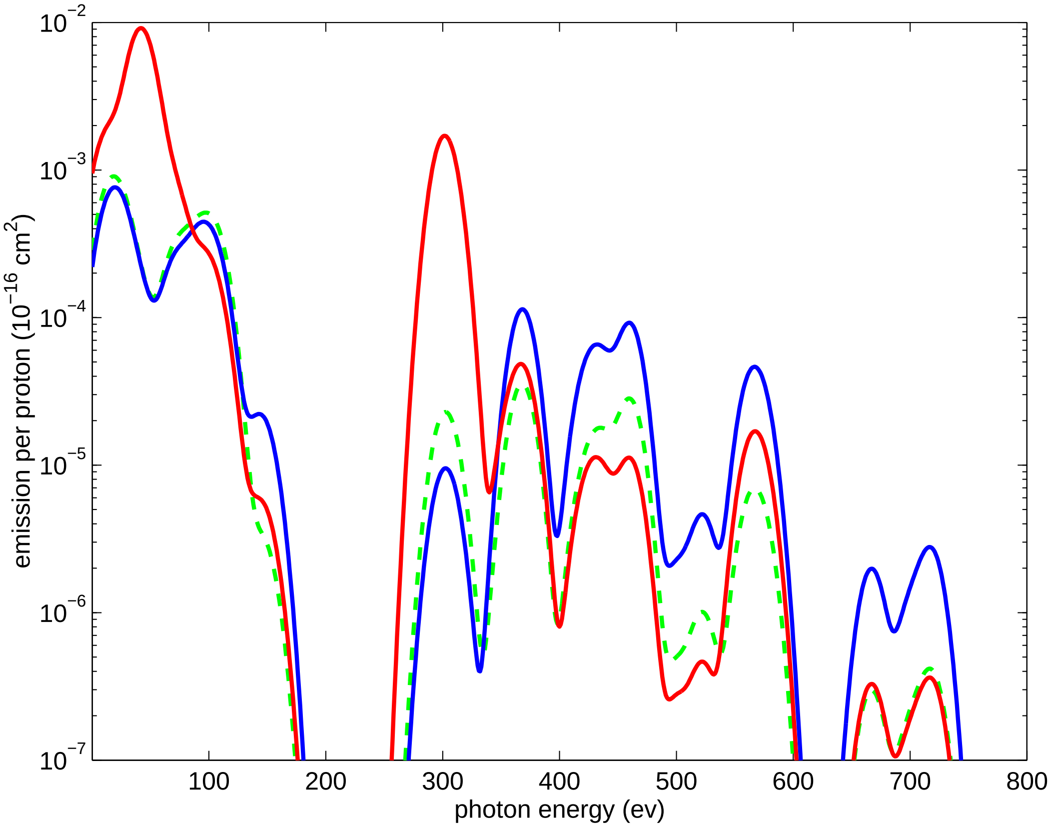

Figure 5.6: Comparison between slow (blue line), fast (red line) and decelerated (dashed green line) wind models with an observational resolution of 10 eV.

A comparison between slow, fast and decelerated wind with the observational

Comet	Instrument	Date	D (A.U.)	Δ (A.U.)	Q (s^{-1})
C/1999 T1	CXO	Jan. 8-14, 2001	1.26	1.37	10^{29}
C/1999 T1	FUSE	Feb. 3-4, 2001	1.43	1.29	$5 \cdot 10^{28}$
C/1995 O1	BeppoSAX	Sep. 10-11, 1996	3.13	2.87	?

Table 5.4: Cometary observations used in this section. D is the comet's heliocentric distance, Δ is the comet's geocentric distance and Q is the gas production rate during the observations.

resolution that is currently available (10 eV) is shown in Figure 5.6. This figure gives a clear insight in the separate velocity effects of cross sections and composition:

- fast and decelerated wind have the same composition, but different cross sections;
- slow and decelerated wind have different compositions but equal cross sections.

At low energies, below 150 eV and around 300 eV, the slow and the decelerated spectra coincide. The much higher emission cross section of the fast wind is therefore an effect of the velocity dependence of state selective cross sections.

The inverse effect can be seen at energies around 650-750 eV where the fast and the decelerated wind spectra are similar: here, the difference between slow and fast wind is made by the different compositions used. For energies in between, the differences between fast and slow wind spectra are caused by a combination of the effects of both the cross sections and the compositional changes.

It can therefore be concluded that in order to investigate the effect of state selective cross sections on the cometary spectrum, the low energy end ($\leq$ 180 eV) is best suited; in order to explore compositional effects, the high end of the spectrum is best suited ($\geq$ 650 eV).

5.4 Comparison with X-Ray Observations

In section 5.3, different calculated spectra were presented for different solar wind velocities. In this section these spectra will be compared with observational spectra from different comets. X-Ray spectra are available for the comets Hale-Bopp, Hyakutake, Linear S4 and McNaught-Hartley (and comet Encke). The observations are summarized in Table 5.4.

5.4.1 McNaught-Hartley

Comet McNaught-Hartley (C/1999 T1) was observed from January 8 to 14, 2001 by Krasnopolsky *et al.* [4] using the Chandra X-Ray telescope.

The deconvolved observations are shown in Figure 5.8. Because the observational data was not available, the spectrum was read out from the original article and these points are indicated in the Figure. Several features are visible, which allow for the identification of various groups of lines. The cometary data can be approximated with the slow wind model, using five times more O^{6+} relative to carbon and nitrogen ions than was used in the original model (Table 2.3).

There are some differences between the cometary data and the spectral model. First, the models shows a gap around 200 eV, where a clear feature is visible in the cometary data. Krasnopolsky identified these lines as MgVIII-X, SiIX and NeVIII emission.

Another important difference between model and data is the emission at energies larger than 600 eV. The observed feature around 600-700 eV cannot be explained by the OVII $(1s3p - 1s^2)$ emission predicted by the model. At the same time, the model predicts strong emission from the OVII $(1s4p - 1s^2)$ and $(1s5p - 1s^2)$ states between 700-750 eV, a feature that is not present in the observations. It is very tempting to relate the relatively high emission at 666 eV and the relatively low emission around 725 eV. Apparently, the $(1s4p)$ and the $(1s5p)$ are populated less than was to be expected from the ionic data use; Kharchenko *et al.* [37] attributed the emission around 650 eV mainly to the strong OVIII $(2p - 1s)$ transition; recall that O^{8+} was not included in this model. The transition from the 5p state to the ground state was not included in the model by Kharchenko.

For an ion with charge 7 colliding on a typical cometary molecule, the Classical Over-the-Barrier predicted that electron capture is preferentially into the $n = 5$ state (Table 3.1). Capture into the $(1s5f)$ or $(1s5g)$ states would decrease the emission due to relaxation from the $(1s4p)$. The net effect would be an increased population of the $(1s3p)$ and $(1s2p)$ states, respectively and the emission from relaxation from these states to the ground states would thus be enhanced.

No measurements were available for the angular momentum distribution for electron capture in slow collisions between O^{7+} and molecular targets. Therefore, two different distributions were assumed in the model. At higher velocities, the charge state distribution from state selective electron captures becomes statistical as was assumed in the fast solar wind model (Table C.1). Calculations using the spectral model show that when a statistical distribution for the $(5l)$ states is assumed, the relative intensity of the 720 eV feature

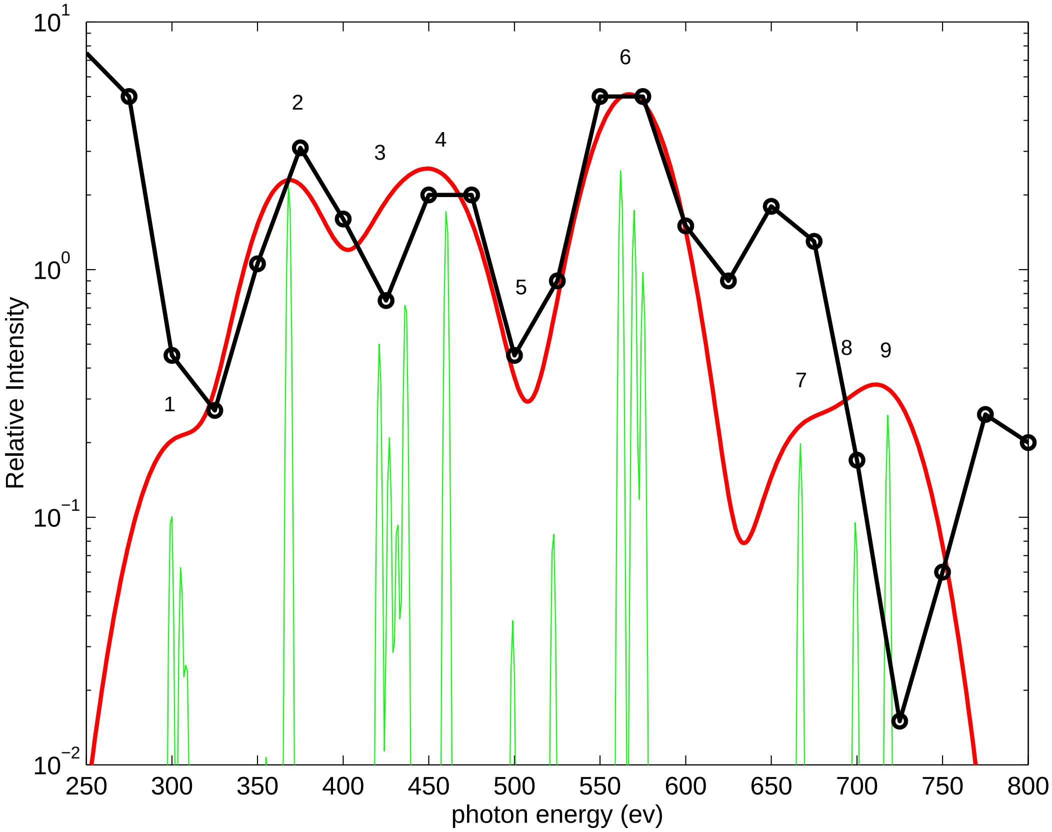

Figure 5.7: Model for the X-Ray spectrum of McNaught-Hartley using a resolution of 20 eV. For comparison, all data is normalized at 560 eV. A model for fast wind (red line) is compared with observations (black dots) by Krasnopolsky *et al.* [4]. The numbers refer to specific emission features, see Table 5.8 below. The green lines are only shown to indicate the position of the lines and are not to scale.

No.	E (eV)	Species	Transition
1	298-310	CV	[1s2s-1s^2], [1s2p-1s^2], 1s2p-1s^2
2	367	CVI	2p-1s
3	419-430	NVI	[1s2s-1s^2], [1s2p-1s^2], 1s2p-1s^2
	435	CVI	3p-1s
4	459	CVI	4p-1s
5	497, 520	NVI	1s3p-1s^2, 1s4p-1s^2
6	560-573	OVII	[1s2s-1s^2], [1s2p-1s^2], 1s2p-1s^2
7	664	OVII	1s3p-1s^2
8	699	OVII	1s4p-1s^2
9	715	OVII	1s5p-1s^2

Figure 5.8: Emission features in Figure 5.7. Forbidden lines are indicated between brackets.

can be reduced by at least a factor of two. This is still not enough to explain the difference between the model and the observations. These results suggest that capture into shells lower than $n = 5$ is the preferred channel for charge exchange between O^{7+} and molecules.

A third possibility would be the ratio between triplet and singlet capture cross sections. Experiments by Lubinski with OVI and NV colliding on H_2 suggest that this ratio is below the statistical value of 3 for the velocities relevant here [46]. Assuming equal cross sections for capture into the triplet and singlet states increases the relative contribution of the 700 eV feature of the spectrum, which is due to singlet transitions only. The choice of the value of the triplet/singlet ratio cannot account for the lack of emission due to the $(5p - 1s)$ transition.

5.4.2 Hale-Bopp

Comet C/1995 01 (Hale-Bopp) was observed by Owens *et al.* [70] using the X-Ray spectrometer LECS on board BeppoSAX on September 10-11 1996 (four days before it was observed with EUVE). At the time of the observations, it was 3.13 A.U. from the Sun and 2.87 A.U. from the Earth.

Figure 5.9 shows a comparison between the spectrum and modelled spectra for different solar wind velocities. The spectrum obtained has an energy resolution of 32% at 0.28 keV and a gaussian curve was used to simulate an observational resolution of 90 eV. The data and the different models are normalized at 400 eV to allow for comparison.

Both the slow and the decelerated wind model match the observations reasonably well. From the discussion for McNaught-Hartley, it was already mentioned that the model does not account for emission between 150-250 eV because of the exclusion of ions heavier than oxygen. Notice that the decelerated wind model would relatively overestimate the emission around 100 eV if emission features were added in the gap. The other interesting feature is the presence of emission at energies $\geq$ 800 eV, which is related to emission by O^{8+}. The fast solar wind contains a neglible fraction of this ion and the feature is therefore characteristic for the slow wind.

The X-Ray radiation observed from comet Hale-Bopp is therefore most probably due to slow wind. The helium line ratio analysis of observations by EUVE performed three dates later indicated a fast wind. An extensive comparison between the two observations has been made by Krasnopolsky *et al.* [71]. In this article, it is also concluded that the observed differences in FUV and X-Ray flux are the effect of highly variable solar wind conditions.

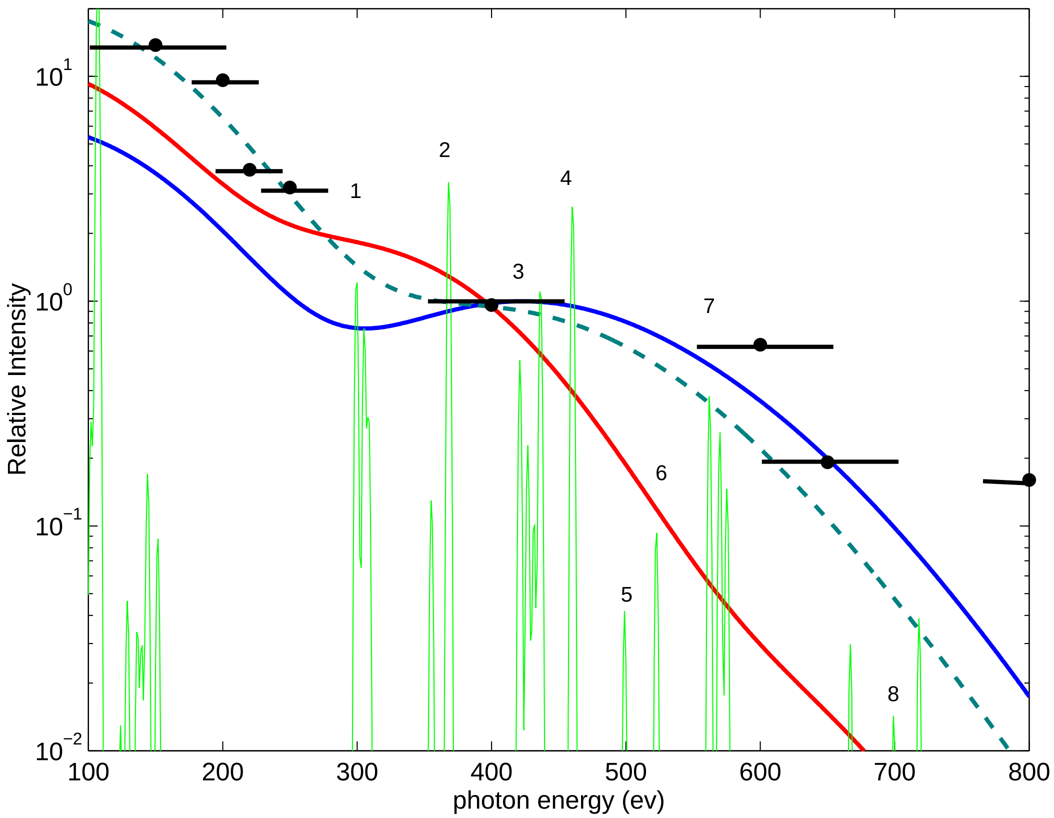

Figure 5.9: Model for the X-Ray spectrum of Hale-Bopp using a resolution of 90 eV. For comparison, all data is normalized at 400 eV. Fast (red line), slow (blue) and decelerated wind (dashed green line) models are compared with observations (black dots) by Owens *et al.* [70]. The numbers refer to emission features, see Table 5.10 below.

No.	Energies	Species
1	300-310	CV
2	350-370	CVI + CV
3	420-440	CVI, NVI
4	450	CVI
5,6	500-520	NVI
7,8	≥550	OVII

Figure 5.10: Emission features in Figure 5.9. More detailed information regarding the transitions involved can be found in Appendix C

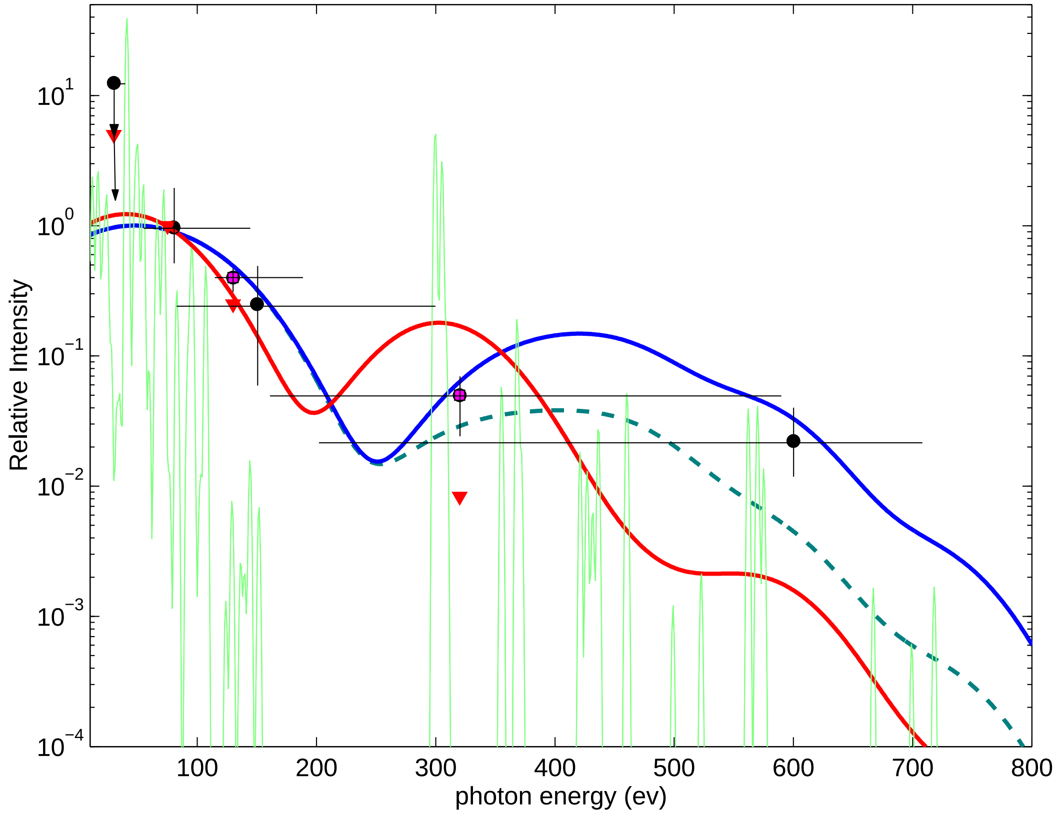

Figure 5.11: Fast (red), slow (blue) and decelerated wind (dotted green) models compared with observational spectra of Linear S4 (black dots, Lisse *et al.* [3]), Encke (red triangles, Lisse *et al.* [29]) and Hyakutake (magenta squares, Lisse *et al.* [1]). Error bars for Encke observations are similar to uncertainties in the other observations.

5.4.3 Hyakutake, Linear S4 and Encke

Spectra of Hyakutake, Linear S4 and Encke are shown in Figure 5.11. As the resolution of the different spectra is very low, it is of no use to extensively compare them with the predicted spectra; what can be seen is that the observations seem to agree well with the predicted model.

5.5 Discussion

The specific characteristics of the slow and fast solar wind allow for a clear distinction between the cometary spectra resulting from the two types of wind. The model shows that both the composition and the velocity dependence of state selective electron capture play an important role in the resulting X-Ray spectrum.

The presence of lines in the high energy region ($\geq 650eV$) of the spectrum is a clear indicator of slow solar wind because ions that can emit in this region have very low abundances in fast solar wind; classification of the wind type is therefore relatively straightforward. A clear improvement of the model would be the inclusion of the rest of the highly charged ions that can emit in this high energy end of the spectrum such as O^{8+} and highly charged neon.

At energies larger than 400 eV, the difference between slow and fast spectra was shown to dependent more strongly on the composition than on the velocity. Because various cascades can be used to produce similar transitions, the spectra are not very sensitive to the original state the electron was captured in. However, in order to compare emission lines of different species it is important to use accurate cross sections.

At lower energies, the emission comes from a large forest of lines and the similarity between the model and the observation is therefore not surprising. To describe this energy regime, both multiple- and sequential electron capture should be included in the model - as was done for the helium ions from the previous section. All these reactions will result in the emission of soft X-Ray and/or FUV photons. Because so many lines are available, this energy regime might be used to check the total intensity of a model with observations in future work.

Concluding, in order to investigate the detailed properties of the solar wind both the available spectra and the model are too crude. Because of the low observational resolution, the models can be fitted to the spectra in various ways. The high resolution spectra that will become available in the near future will allow for more detailed study of the observations using computer models as the one presented here. For such a model, it will be absolutely necessary to include accurate state selective cross sections.

It should be remarked that in X-Ray spectrometry it is favourable to compare the outcome of any model with an original spectrum rather than with a deconvolved spectrum as was done here, because of the high complexity of the instrument response functions of the X-Ray detectors. This procedure was not followed here because the original spectral data was not available to the author.

Chapter 6

Conclusion and Outlook

In this thesis, the interaction between comet and the solar wind by means of charge exchange is studied. The probability that one or more electrons are captured by a highly charged ion is expressed by the cross section of the process. It is important to distinguish between two different cross sections. First, the total cross section of the process, which includes all possible electron capture processes. Second, the state selective cross section that describes the probability of electron capture into one specific state.

With the experimental setup 'AGORA' at the KVI, the dependence of state selective electron capture processes on the collisional velocity is measured using the technique of Photon Emission Spectroscopy. Here, the light emitted after a charge transfer reaction is collected in a FUV spectrometer. These experiments have been performed for a large variety of projectiles and target gases.

Of special interest are collisions between fully stripped helium and molecular targets because double electron capture becomes dominating over single electron capture at velocities below ca. 1 keV/amu. These processes result in two characteristic lines, at 58.4 nm and 30.4 nm respectively.

This experimental data was combined with a simple 2D model for the cometary environment. For comet Halley, the distribution of He^{2+} and He^{+} was modelled along the trajectory of Giotto, the probe that passed the comet in 1986. It was shown that the charge state distribution in the outer regions of the comet can be understood in terms of the simple model but that for the more inner regions, a more detailed cometary model is required as plasma effects become more important.

The model was also used to predict cometary FUV emission due to state selective electron capture by helium. It was shown that the ratio between the two helium lines depends almost solely on the velocity of the solar wind, while the absolute intensity of the lines is a measure of the characteristics of the comet involved. Emission from both Hale-Bopp and Hyakutake was analyzed with the model and solar wind velocities of 220 km/s (Hale-Bopp) and 425 km/s (Hyakutake) were found.

The next step was to use the available state selective data to model the X-Ray spectra available for various, different comets. The spectra produced by the model showed a clear dependence on the solar wind velocity, both by means of the composition and by means of the state selective cross sections. It was concluded that currently, only limited conclusions can be drawn on the composition of the solar wind because of both experimental and observational uncertainties.

The next goal will be to extend the helium emission line to a 3D model, so that absolute intensities can be calculated. This allows for investigating the cometary environment.

A challenge for future work is obviously the combination of the two models presented in this work. The best candidate to do this would be oxygen, because first, it is the next most abundant element in the solar wind and second, electron capture by highly charged oxygen has some very distinct lines in the high end of the X-Ray spectrum. It would be very interesting to follow a highly charged oxygen ion along its trajectory through the coma, slowly being neutralized by subsequent charge exchange reactions. The photons emitted after these reactions will allow for a detailed probing of the comet, as each reaction is a product of both the cometary environment and the ionic velocity. To allow for such a thorough study of the interaction system, collisions between all the oxygen charge states and molecules should be explored in the laboratory, while the astronomers should work on detailed maps of the spatial distributions of the oxygen emission.

Bibliography

[1] C.M. Lisse, K. Dennerl, J. Englhauser, M. Harden, F.E. Marshall, M.J. Mumma, R. Petre, J.P Pye, M.J. Ricketts, J. Schmitt, J. Trumper, and R.G. West. *Science*, 274:205, 1996.

[2] T.E. Cravens. *Geophys. Res. L.*, 24(1):105, 1987.

[3] C.M. Lisse, D.J. Christian, K. Dennerl, K.J. Meech, R. Petre, H.A. Weaver, and S.J. Wolk. *Science*, 292:1343, 2001.

[4] V. Krasnopolsky, D. Christian, V. Kharchenko, A. Dalgarno, S. Wolk, C. Lisse, and A. Stern. *Icarus*, 160:437, 2002.

[5] K. Dennerl, V. Burwitz, J. Englhauser, C. Lisse, and S. Wolk. *Astron. Astrophys.*, 386:319, 2002.

[6] K. Dennerl. *Astron. Astrophys.*, 394:1119, 2002.

[7] R.F. Elsner, G. R. Gladstone, J.H. Waite, F.J. Crary, R.R. Howell, R.E. Johnson, P.G. Ford, A.E. Metzger, K.C. Hurley, E.D. Feigerlson, G.P. Garmire, A. Bhardwaj, D.C. Grodent, T. Majeed, A.F. Tennant, and M.C. Weisskopf. *Ap.J.*, 572:1077, 2002.

[8] N. Biver, D. Bockelee-Morvan, P. Colom, J. Crovisier, J.K. Davies, W.R.F. Dent, D. Despois, E. Gerard, E. Lellouch, H. Rauer, R. Moreno, and G. Paubert. *Science*, 275:1915, 1997.

[9] D. Krankowsky. *Comets in the Post-Halley Era*, volume 2. Kluwer Academic Publishers, 1990.

[10] W.F. Huebner, J.J. Keady, and S.P. Lyon. *ApSS*, 195(1):291, 1992.

[11] K. Jockers and T. Bonev. *Astron. Asrophys.*, 319:617, 1997.

[12] K. Jockers, T. Bonev, and T. Credner. *ApSS*, 264:227, 1999.

[13] W.-H. Ip and W.I. Axford. *Comets*. University of Arizona Press, 1982.

[14] W.-H. Ip. *Astron. Astrophys.*, 92:95, 1980.

[15] T.E. Cravens. *Science*, 296(2):1042, 2002.

[16] M. Neugebauer. *Rev. Geoph.*, 28(2):231, 1990.

[17] R. Wegmann, K. Jockers, and T. Bonev. *Plan.Space Sci.*, 47:745, 1999.

[18] K.R. Flammer. *Comets in the Post-Halley Era*, volume 2. Kluwer Academic Publishers, 1990.

[19] S.A. Fuselier, E.G. Shelley, B.E. Goldstein, R. Goldstein, M. Neugebauer, W.-H. Ip, H. Balsiger, and H. Reme. *Ap.J.*, 379:734, 1991.

[20] R.M. Haeberli, K. Altwegg, H. Balsiger, and J. Geiss. *Astron.Astrophys.*, 297:881, 1995.

[21] W.F. Huebner, J.J. Keady, D.C. Boice, H.U. Schmidt, and R. Wegmann. *IAU symp.*, 120(2):431, 1987.

[22] R. von Steiger, T.H. Zurbuchen, J. Geiss, G. Gloeckler, L.A. Fisk, and N.A. Schwadron. *Sp.Sc.Rev.*, 72:71, 1995.

[23] J. Geiss, G. Gloeckler, R. von Steiger, H. Balsiger, L.A. Fisk, A.B. Galvin, F.M. Ipavich, S. Livi, J.F. McKenzie, K.W. Ogilvie, and B. Wilken. *Science*, 268:1033, 1995.

[24] M. Neugebauer, R.J. Forsyth, A.B. Galvin, K.L Harvey, J.T. Hoeksema, A.J. Lazarus, R.P. Lepping, J.A. Linker, Z. Mikix, J.T. Steinberg, R. von Steiger, Y.-M. Wang, and R.F. Wimmer-Schweingruber. *JGR*, 103(A8):14587, 1998.

[25] N.A. Schwadron and T.E. Cravens. *Ap.J.*, 544:558, 2000.

[26] M.R. Aellig, A.J. Lazarus, and J.T. Steinberg. *Geoph. Res. Lett.*, 28(14):2767, 2001.

[27] P. Boschler, J. Geiss, and S. Kunz. *Solar Physics*, 103:177, 1986.

[28] L. Villenueva, R.L. McNutt Jr., A.J. Lazarus, and J.T. Steinberg. *JGR*, 99(A2):2553, 1994.

[29] C.M. Lisse, K. Dennerl, and J. Englhauser et al. *EMP*, 77:283, 1999.

[30] V.A. Krasnopolsky, M.J. Mumma, M. Abott, B.C. Flynn, K.J. Meech, D.K. Yeomans, P.D. Feldman, and C.B. Cosmovici. *Science*, 277:1488, 1997.

[31] V. Krasnopolsky and M.J. Mumma. *Ap.J.*, 549:629, 2001.

[32] R.M. Haeberli, T.I. Gombosi, D.L. De Zeeuw, M.R. Combi, and K.G. Powell. *Science*, 276:939, 1997.

[33] R. Wegmann, H.U. Schmidt, C.M. Lisse K. Dennerl, and J. Englhauser. *Plan.Space Sci.*, 5:603, 1998.

[34] V. Kharchenko and A. Dalgarno. *J.Geophys.Res.*, 105(A8):18351, 2000.

[35] V. Kharchenko and A. Dalgarno. *Ap.J.*, 557:L99, 2001.

[36] K. Dennerl, J. Englhauser, and J.Trumper. *Science*, 277:1625, 1997.

[37] V. Kharchenko, M. Rigazio, A. Dalgarno, and V.A. Krasnopolsky. *Ap.J.*, 585:L73, 2003.

[38] P. Beiersdorfer, C.M. Lisse, R.E. Olson, G.V. Brown, and H. Chen. *ApJ*, 549:L147, 2001.

[39] N. Bohr and J. Lindhard. *K. Dan. Vidensk. Selsk. Mat. Fys. Medd.*, 28:7, 1954.

[40] D. Dijkkamp. *Electron Capture into Excited States of Multi-Charged Ions.* PhD thesis, Universitíteit Utrecht, 1985.

[41] A. Barany, G. Astner, H. Cederquist, H. Danared, S. Huldt, A. Johnson P. Hvelplund, H. Knudsen, L. Liljeby, and K.G. Rensfelt. *Nucl. Instr. Meth. B*, 9:397, 1985.

[42] H. Ryufuku, K. Sasaki, and T. Watanabe. *Phys. Rev. A*, 21:745, 1980.

[43] A. Niehaus. *J. Phys. B.*, 19:2925, 1986.

[44] S.S. Gershtein. *Sov. Phys.- JETP*, 16:501, 1962.

[45] R. Hoekstra. *Photons Shedding Light on Electron Capture by Highly Charged Ions.* PhD thesis, RijksUniversiteit Groningen, 1990.

[46] G. Lubinski. *Light - A Fingerprint of Astrophysical Processes.* PhD thesis, RijksUniversiteit Groningen, 2001.

[47] G. Lubinski, Z. Juhasz, R. Morgenstern, and R. Hoekstra. *Phys. Rev. Lett.*, 86(4):616, 2001.

[48] R. Hoekstra and R. Morgenstern. *Highly Charged Ions Book: Photon Emission Spectroscopy of Electron Capture and Excitation by Multiply Charged Ions.* (to be published).

[49] M.B. Shah and H.B. Gilbody. *J. Phys. B.*, 23:1494, 1990.

[50] D.M. Kearns, D.R. Gillen, D. Voulot, J.B. Greenwood, R.W. McCullough, and H.B. Gilbody. *J. Phys. B.*, 34:3401, 2001.

[51] J.W. Turkstra, R. Hoekstra, S. Knoop, D. Meyer, R. Morgenstern, and R.E. Olsen. *Phys. Rev. Lett*, 87:123202, 2001.

[52] J.W. Turkstra. *Hot Recoils from Cold Atoms.* PhD thesis, RijksUniversiteit Groningen, 2001.

[53] P. Sobocinski, J. Rangama, J.Y. Chesnel, M. Tarisien, L. Adoui, A. Cassimi, X. Husson, and F. Fremont. *J. Phys. B*, 34:L367, 2001.

[54] J.B. Greenwood, I.D. Williams, S.J. Smith, and A. Chutjian. *ApJ*, 533:L175, 2000.

[55] I. Cadez, J.B. Greenwood, A. Chutjian, R.J. Mawhorter, S.J. Smith, and M. Niimura. *J. Phys. B. (submitted)*, 2003.

[56] A.G. Drentje. *Nucl. Instr. Meth. Phys. Res.*, B9:526, 1985.

[57] F.W. Bliek. *State Selective Electron Capture at Low Energies.* PhD thesis, RijksUniversiteit Groningen, 1997.

[58] K. Ishii, K. Okuno, and N. Kobayashi. *Phys. Scr*, T80:176, 1999.

[59] M.E. Rudd, T.V. Goffe, and A. Itoh. *J. Phys. A.*, 28:3244, 1985.

[60] H.O. Folkerts, R. Hoekstra, and R. Morgenstern. *Phys. Rev. Lett.*, 77(16):3339, 1997.

[61] T.F. Moran. *J. Chem. Phys.*, 58(9):3793, 1973.

[62] W.-H. Ip and L. Jorda. *ApJ.*, 496:L47, 1998.

[63] W.R. Thompson, M.B. Shah, and H.B. Gilbody. *J. Phys. B.*, 29(13):2847, 1996.

[64] I. de Pater and J.J. Lissauer. *Planetary Sciences.* Cambridge University Press, 2001.

[65] B.E. Goldstein, M. Neugebauer, H. Balsiger, J. Drake, S.A Fuselier, R. Goldstein, W.-H. Ip, U. Rettenmund, H. Rosenbauer, R. Schwenn, and E.G. Shelley. *Astron. Astrop.*, 187:175, 1987.

[66] E.G. Shelley, S.A. Fuselier, H. Balsiger, J.F. Drake, J. Geiss, B.E. Goldstein, R. Goldstein, W.-H. Ip, A.J. Lazarus, and M. Neugebauer. *Astron. Astrophys.*, 187:304, 1987.

[67] M.J. Mumma, M.A. Disanti, N. dello Russo, M. Fomenkova, K. Magee-Sauer, C.D. Kaminski, and D.X. Xie. *Science*, 272(5266):1310, 1996.

[68] W.L. Wiese, J.R. Fuhr, and T.M. Deters. *Atomic Transition Probabilities of Carbon, Nitrogen and Oxygen.* Journal of Physical and Chemical Reference Data, 1996.

[69] S. Bashkin and J.O. Stoner. *Atomic Energy Levels and Grotrian Diagrams 1.* American Elsevier Publishing Company, Inc., 1975.

[70] A. Owens, N. Parmar, T. Oosterbroek, A. Orr, L.A. Antonelli, F. Fiore, R. Schulz, G.P. Tozzi, M.C. Maccarone, and L. Piro. *Ap.J.*, 493:L47, 1998.

[71] V. Krasnopolsky, M.J. Mumma, and M.J. Abott. *Icarus*, 146:152, 2000.

[72] W.L. Nutt, R.W. McCullough, K. Brady, M.B. Shah, and H.B. Gilbody. *J. Phys. B.*, 11(8):1457, 1978.

[73] M.C. van Hemert, E.F. van Dishoeck, J.A. van der Hart, and F. Koike. *Phys. Rev. A*, 31(4):2227, 1985.

[74] L.F. Errea, L. Mendez, and A. Riera. *Z. Phys. D.*, 14:229, 1989.

[75] B. Zygelman, A. Dalgarno, M. Kimura, and N.F Lane. *Phys. Rev. A*, 40(5):2340, 1989.

[76] M.B. Shah and H.B. Gilbody. *J. Phys. B.*, 9(15):2685, 1990.

[77] C.D. Lin, W.R. Johnson, and A. Dalgarno. *J. Phys. A.*, 15(1):154, 1977.

[78] R.A. Phaneuf, R.K. Janev, and M.S. Pindzola. *Collisions of Carbon and Oxygen ions with Electrons, H, H2 and He.* ONRL 6090, 1987.

[79] J.B. Greenwood, I.D. Williams, S.J. Smith, and A. Chutjian. *Phys. Rev. A*, 63:0627071, 2001.

[80] M.G. Suraud, R. Hoekstra, F.J. de Heer, J.J. Bonnet, and R. Morgenstern. *J. Phys. B.*, 24:2543, 1991.

Appendix A

Helium Electron Capture Data

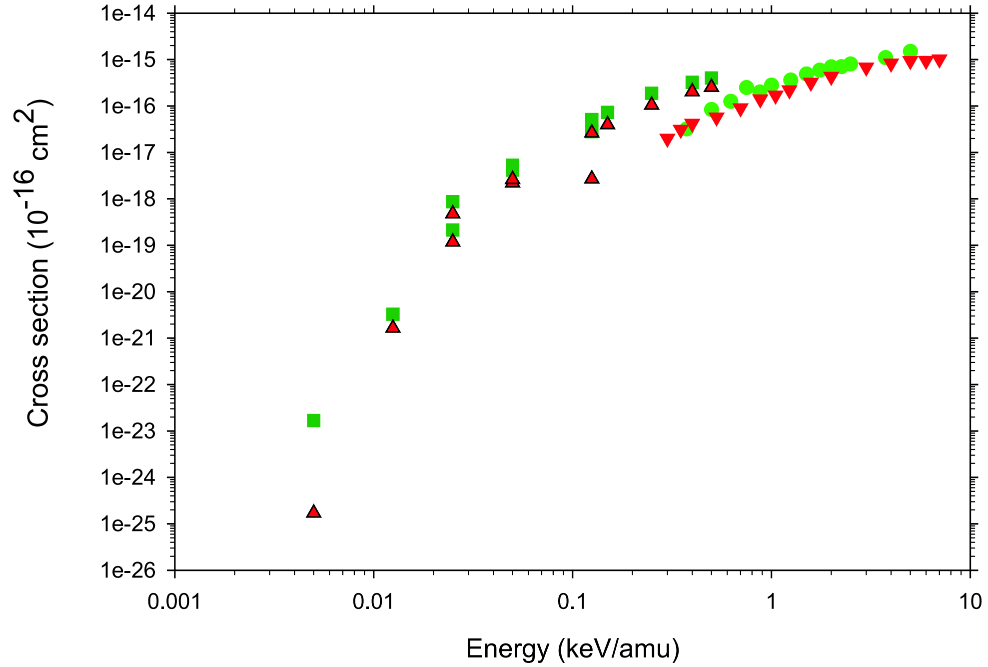

Figure A.1: Total and state selective cross sections for HeIII colliding on atomic H. Experimental values: red circles: total cross sections, Nutt *et al.* [72]; reverse red triangles: ($2p$) state selective cross sections by Hoekstra *et al.* [45]. Theoretical predictions; green squares: total cross sections, red triangles: ($2p$) cross sections, Van Hemert *et al.* [73]

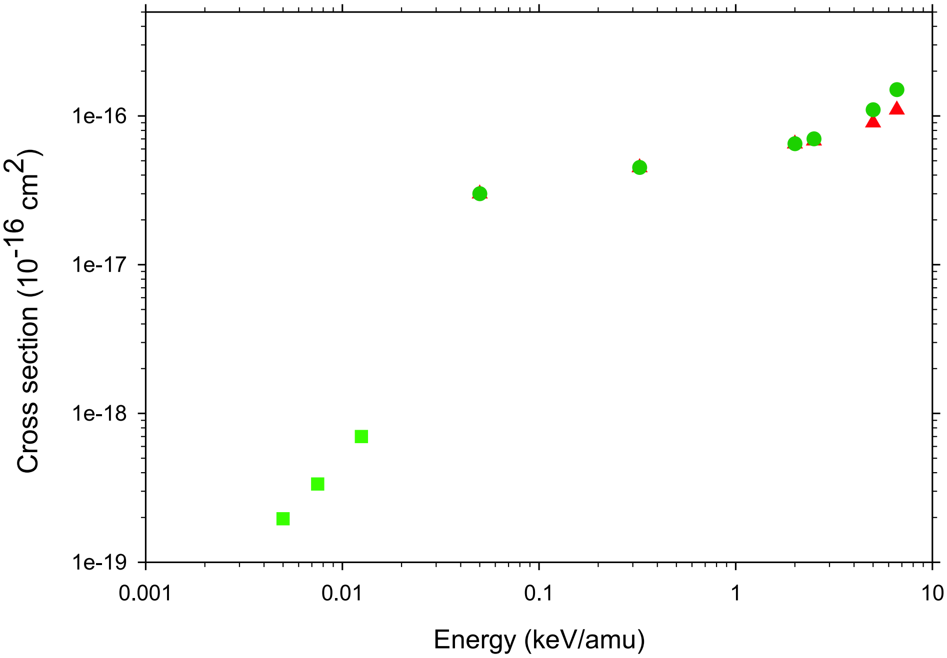

Figure A.2: Total and state selective cross sections for HeII colliding on atomic H. Experimental values: green dots, total cross sections; red triangles, capture into ($1s2p$). Both taken from an overview article by Errea *et al.* [74]. Theory: green squares for total cross sections by Zygelman *et al.* [75].

v (keV/amu)	Collisions with CO			Collisions with H	
	He^{2+} SEC	He^{2+} DEC	He^{+} SEQ	He^{2+} SEC	He^{+} SEQ
0.01	0.90	25.00	5.00	2.00E-06	4.50E-03
0.05	1.60	10.10	6.00	0.03	0.30
0.12	3.20	9.00	6.50	0.30	0.35
0.25	5.00	6.00	7.20	0.32	0.37
0.30	5.00	5.50	7.50	0.32	0.40
0.50	5.00	5.30	7.50	2.50	0.50
1.00	6.00	5.00	7.50	5.00	0.50
3.00	8.00	4.00	8.20	10.50	0.80
5.00	10.20	3.00	8.50	12.00	1.50
6.00	10.50	3.00	9.00	15.00	1.50

Table A.1: Total cross section used in the models for capture by helium ions

v (keV/amu)	Collisions with CO			Collisions with H	
	He^{2+} SEC	He^{2+} DEC	He^{+} SEQ	He^{2+} SEC	He^{+} SEQ
0.01	0.00	0.50	0.15	1.00E-06	4.50E-03
0.05	0.00	0.50	0.12	0.02	0.31
0.12	0.00	0.50	0.20	0.15	0.35
0.25	0.20	0.50	0.19	0.16	0.37
0.30	0.40	0.50	0.25	0.16	0.40
0.50	0.90	0.50	0.27	0.50	0.60
1.00	3.00	0.50	0.25	1.70	0.60
3.00	8.00	0.50	0.32	6.80	0.80
5.00	10.50	0.50	0.35	9.00	1.00
6.00	10.50	0.50	0.35	10.00	1.00

Table A.2: State selective cross section used in the models for capture by helium ions

Appendix B

Giotto Geometry

In March 1986, comet Halley was probed by several small satellites. Giotto was the name of the probe that came nearest to the cometary nucleus; it passed the nucleus at 536 km.

Figure B.1 shows Giotto's rendez-vous with comet Halley assuming symmetry in both the horizontal and vertical direction. The angle α between the probe's trajectory and the comet-Sun axis was 73°. The minimum distance to the nucleus is denoted by β; the impact parameter of the ionic trajectory is given by b.

The model calculates the charge state distribution along parallel ionic tra-

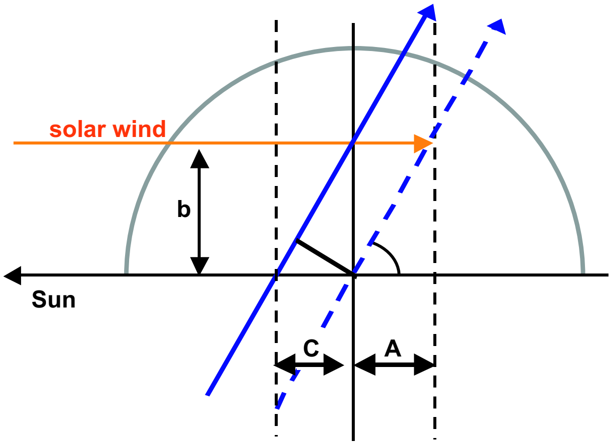

Figure B.1: Schematic drawing of the geometry of Giotto's trajectory through comet Halley. The probe's trajectory is indicated by a blue arrow; a solar wind tracjectory is indicated by an orange arrow.

jectories with different impact parameters b. To compare the model with the measurements, the charge state should be calculated for the positions where these ionic trajectories cross with Giotto's trajectory.
To do this, we first shift the Giotto trajectory over the comet-Sun axis so that it runs through the origin. This shift is given by C:

$$C = \frac{\beta}{\tan \alpha} \tag{B.1}$$

Since the ion crossed the y-axis, it has travelled a distance A through the coma before it crosses the shifted trajectory:

$$A = \frac{b}{\tan \alpha} \tag{B.2}$$

Subtraction of the shift yields the distance an ion has travelled (after crossing the y-axis) through the coma before it is picked up by Giotto. What is left, is to calculate Giotto's distance to the nucleus, given by r:

$$r^2 = b^2 + (A - C)^2 \tag{B.3}$$

Using this relations, the model can be used to calculate the charge state distribution along the trajectory of Giotto.

Appendix C

Ionic Data

In this appendix, all data and all assumptions used in the X-Ray spectral model is summarized.

C.1 Helium

All helium ions in the solar wind are fully stripped. Both single- and double electron capture is allowed. For the slow wind, state selective cross section were taken from Lubinski *et al.* [46]. Fast SEC cross sections were taken from Hoekstra *et al.* [45] and Shah *et al.* [76]; fast DEC cross sections were taken from Shah *et al.* [49] and Lubinski *et al.* [46].

C.2 OVIII

Electron capture by OVIII can lead to both triplet and singlet OVII ions. It was assumed that these processes show the same state selective behaviour, but that capture into the triplet state has a cross section that is three times as large as the cross section of capture into the singlet state. The 'forbidden' transitions ^{3}P to ^{1}S and ^{3}S to ^{1}S were included in the branching matrix using branching ratio's from Lin *et al.* [77].

For slow collisions, no state selective cross sections were available. Using the Over-the-Barrier model, it is to be expected that all capture occurs in the $n = 5$ state (Table 3.1). For the angular momentum distribution, it was assumed that all $(5l)$ states are equally populated. Total cross sections by [78] were used.

There was also no state selective data available for fast OVIII. State selective cross sections were estimated using the total cross section by [78] and

Transition	E (eV)	Slow (%)	Fast (%)	2.7 keV/amu (%)
2p-1s	574	63.8	77.5	70
3p-1s	666	8.4	9.3	13
4p-1s	698	6.3	3.5	17
5p-1s	713	16.9	9.6	

Table C.1: Relative contributions for X-Ray emission from collisions of OVIII with water. Slow and fast are the results of the two spectral models; in the last column, the results of experiments performed by Greenwood *et al.* [79] are shown . For the experiments, the value for $(4p-1s)$ also includes emission by the $(5p-1s)$ transition.

the assumption that electron capture by fast ions leads to a statistical distribution over the $(5l)$ states, corrected for an underpopulation of the $(5s)$ state. Comparison of the results of the model with X-Ray measurements done on collisions between OVIII and H_2O by Greenwood *et al.* [79] confirm the validity of this assumption, see Table C.1.

C.3 OVII

Slow state selective cross sections were taken from Lubinski *et al.* [46], data for fast collisions from Dijkkamp *et al.* [40].

C.4 NVII

Electron capture by NVII can lead to both triplet and singlet NVI ions. The ratio 1:3 was again used for the cross sections and again, capture into a singlet state yields the same (nl) distribution as capture into the triplet state. The 'forbidden' transitions ^{3}P to ^{1}S and ^{3}S to ^{1}S were included in the branching matrix using branching ratio's from Lin *et al.* [77].

Because no state selective data was available for slow NVII, the cross sections for OVII by Lubinski *et al.* [46] were used instead. For fast NVII, state selective cross sections by Dijkkamp *et al.* [40] were used.

C.5 NVI

Slow state selective cross sections were taken from Lubinski *et al.* [46], data for fast collisions from Dijkkamp *et al.* [40].

C.6 CVII

Because no state selective data was available for slow CVII, the cross sections for OVII by Lubinski *et al.* [46] were used instead. For fast collisions, the average of state selective cross sections of NVII and OVII was used *et al.* [40].

C.7 CVI

Electron capture into the CV singlet and triplet state is allowed. Similar (nl) distributions and statistically scaled cross sections were assumed. The 'forbidden' transitions ^{3}P to ^{1}S and ^{3}S to ^{1}S were included in the branching matrix using branching ratio's from Lin *et al.* [77]. Cross sections for slow NVI were used as no state selective data was available. For fast collisions, measurements by Suraud *et al.* [80] were used.

Appendix D

X-Ray Line List

In the following tables, the transitions can be found that were used in the model for the X-Ray spectra from Chapter 5. All data is taken from Wiese *et al* [68] and Bashkin and Stoner [69].

Ion	λ (nm)	E (ev)	Transition	Multiplet	Ion	λ (nm)	E (ev)	Transition	Multiplet
OVII	1.7	715.3	1s^2 - 1s5p	^{1}S - ^{1}P	CVI	13.5	91.7	2p - 4s	^{1}P - ^{1}S
OVII	1.8	696.5	1s^2 - 1s4p	^{1}S - ^{1}P	CVI	13.5	91.7	2s - 4p	^{1}S - ^{1}P
OVII	1.9	664.4	1s^2 - 1s3p	^{1}S - ^{1}P	CVI	13.5	91.7	2p - 4d	^{1}P - ^{1}D
OVII	2.2	572.9	1s^2 - 1s2p	^{1}S - ^{1}P	NVI	13.7	90.6	1s2p - 1s4d	^{1}P - ^{1}D
OVII	2.2	567.7	1s^2 - 1s2p	^{1}S - ^{3}P	OVI	15.0	82.5	1s^{2}2s - 1s^{2}3p	^{2}S - ^{2}P
OVII	2.2	560.0	1s^2 - 1s2s	^{1}S - ^{3}S	NVI	16.1	76.9	1s2s - 1s3p	^{3}S - ^{3}P
NVI	2.4	520.6	1s^2 - 1s4p	^{1}S - ^{1}P	NVI	16.1	76.8	1s2s - 1s3p	^{1}S - ^{1}P
NVI	2.5	497.0	1s^2 - 1s3p	^{1}S - ^{1}P	OVI	17.3	71.5	1s^{2}2p - 1s^{2}3d	^{2}P - ^{2}D
CVI	2.7	458.5	1s - 4p	^{1}S - ^{1}P	NVI	17.4	71.1	1s2p - 1s3d	^{3}P - ^{3}D
CVI	2.8	434.7	1s - 3p	^{1}S - ^{1}P	NVI	18.1	68.5	1s2p - 1s3s	^{1}P - ^{1}S
NVI	2.9	429.9	1s^2 - 1s2p	^{1}S - ^{1}P	NVI	18.1	68.4	1s2p - 1s3s	^{3}P - ^{3}S
NVI	2.9	425.3	1s^2 - 1s2p	^{1}S - ^{3}P	CVI	18.2	68.0	2s - 3p	^{1}S - ^{1}P
NVI	3.0	419.5	1s^2 - 1s2s	^{1}S - ^{3}S	CVI	18.2	67.9	2p - 3d	^{1}P - ^{1}D
CVI	3.4	366.8	1s - 2p	^{1}S - ^{1}P	CVI	18.2	67.9	2p - 3s	^{1}P - ^{1}S
CV	3.5	353.9	1s^2 - 1s3p	^{1}S - ^{1}P	OVI	18.4	67.3	1s^{2}2p - 1s^{2}3s	^{2}P - ^{2}S
CV	4.0	307.3	1s^2 - 1s2p	^{1}S - ^{1}P	NVI	18.5	66.9	1s2p - 1s3d	^{1}P - ^{1}D
CV	4.1	304.1	1s^2 - 1s2p	^{1}S - ^{3}P	NV	20.9	59.2	1s^{2}2s - 1s^{2}3p	^{2}S - ^{2}P
CV	4.1	298.4	1s^2 - 1s2s	^{1}S - ^{3}S	CV	22.7	54.5	1s^2 - 1s3p	^{1}S - ^{3}P
OVII	8.2	151.1	1s2s - 1s5p	^{3}S - ^{3}P	OVII	24.6	50.3	1s3s - 1s5p	^{3}S - ^{3}P
OVII	8.6	143.9	1s2s - 1s5p	^{1}S - ^{1}P	CV	24.7	50.0	1s2s - 1s3p	^{1}S - ^{1}P
OVII	8.6	143.7	1s2p - 1s5d	^{3}P - ^{3}D	NV	24.8	49.9	1s^{2}2p - 1s^{2}3d	^{2}P - ^{2}D
OVII	8.6	143.6	1s2p - 1s5s	^{3}P - ^{3}S	CV	24.9	49.8	1s2p - 1s3d	^{3}P - ^{3}D
OVII	8.7	142.2	1s2p - 1s5s	^{1}P - ^{1}S	OVII	25.5	48.5	1s3s - 1s5p	^{1}S - ^{1}P
OVII	8.9	139.0	1s2p - 1s5d	^{1}P - ^{1}D	OVII	25.5	48.5	1s3d - 1s5p	^{1}D - ^{1}P
OVII	9.1	135.9	1s2s - 1s4p	^{3}S - ^{3}P	OVII	25.5	48.5	1s3p - 1s5d	^{3}P - ^{3}D
OVII	9.1	135.9	1s2s - 1s4p	^{1}S ^{1}P	OVII	25.6	48.3	1s3p - 1s5s	^{3}P - ^{3}S
OVII	9.6	128.7	1s2p - 1s4d	^{3}P - ^{3}D	CV	26.0	47.6	1s2p - 1s3s	^{3}P - ^{3}S
OVII	9.7	127.5	1s2p - 1s4s	^{3}P - ^{3}S	CV	26.0	47.6	1s2p - 1s3s	^{1}P - ^{1}S
OVII	9.7	127.5	1s2p - 1s4s	^{1}P - ^{1}S	OVII	26.1	47.4	1s3d - 1s5f	^{3}D - ^{3}F
OVII	10.0	123.4	1s2p - 1s4d	^{1}P - ^{1}D	OVII	26.2	47.3	1s3d - 1s5f	^{1}D - ^{1}F
OVII	11.4	108.3	1s3p - 1s3d	^{3}P - ^{3}D	OVII	26.2	47.2	1s3p - 1s5s	^{1}P - ^{1}S
OVI	11.6	106.7	1s^{2}2s - 1s^{2}4p	^{2}S - ^{2}P	OVII	26.2	47.2	1s3d - 1s5p	^{3}D - ^{3}P
OVII	12.0	102.8	1s2s - 1s3p	^{3}S - ^{3}P	OVII	26.3	47.1	1s3p - 1s5d	^{1}P - ^{1}D
OVII	12.0	102.8	1s2s - 1s3p	^{1}S - ^{1}D	NV	26.6	46.5	1s^{2}2p - 1s^{2}3s	^{2}P - ^{2}S
NVI	12.2	101.4	1s2s - 1s4p	^{3}S - ^{3}P	CV	26.7	46.3	1s2p - 1s3d	^{1}P - ^{1}D
NVI	12.2	101.1	1s2s - 1s4p	^{1}S - ^{1}P	HeII	30.4	40.7	1s - 2p	^{1}S - ^{1}P
OVII	12.8	96.3	1s2p - 1s3d	^{1}P - ^{1}S	OVII	35.2	35.1	1s3s - 1s4p	^{1}S - ^{1}P
OVII	12.8	96.3	1s2p - 1s3d	^{3}P - ^{3}D	OVII	35.2	35.1	1s3s - 1s4p	^{3}S - ^{3}P
NVI	13.0	95.2	1s2p - 1s4d	^{3}P - ^{3}D	OVII	37.0	33.5	1s3p - 1s4d	^{3}P - ^{3}D
OVI	13.0	95.2	1s^{2}2p - 1s^{2}4d	^{2}P - ^{2}D	OVII	38.2	32.4	1s3d - 1s4f	^{3}D - ^{3}F
NVI	13.1	94.5	1s2p - 1s4s	^{3}P - ^{3}S	OVII	38.3	32.3	1s3d - 1s4f	^{1}D - ^{1}F
NVI	13.2	93.8	1s2p - 1s4s	^{1}P - ^{1}S	OVII	38.4	32.3	1s3p - 1s4s	^{1}P - ^{1}S
OVI	13.2	93.8	1s^{2}2p - 1s^{2}4s	^{2}P - ^{2}S	OVII	38.4	32.3	1s3p - 1s4s	^{3}P - ^{3}S
OVII	13.3	93.2	1s2p - 1s3s	^{1}P - ^{1}P	OVII	38.7	31.9	1s3d - 1s4p	^{1}D - ^{1}P
OVII	13.3	93.2	1s2p - 1s3s	^{3}P - ^{3}S	OVII	38.7	31.9	1s3d - 1s4p	^{3}D - ^{3}P

continued on the next page

Table D.1: Transitions included in the slow solar wind model

continued from the previous page

Ion	λ (nm)	E (ev)	Transition	Multiplet	Ion	λ (nm)	E (ev)	Transition	Multiplet
OVII	38.7	31.9	1s3p - 1s4d	^{1}P - ^{1}D	HeI	58.4	21.2	1s^2 - 1s2p	^{1}S - ^{1}P
OVI	44.8	27.6	1s^{2}3s - 1s^{2}4p	^{2}S - ^{2}P	OVII	77.5	16.0	1s4s - 1s5p	^{3}S - ^{3}P
NVI	47.4	26.1	1s3s - 1s4p	^{3}S - ^{3}P	OVII	79.7	15.5	1s4s - 1s5p	^{1}S - ^{1}P
NVI	49.8	24.9	1s3s - 1s4p	^{1}S - ^{1}P	OVII	80.1	15.5	1s4p - 1s5d	^{3}P - ^{3}D
OVI	49.8	24.8	1s^2 3p - 1s^{2}4d	^{2}P - ^{2}D	OVII	82.0	15.1	1s4f - 1s5d	^{3}F - ^{3}D
NVI	50.1	24.7	1s3p - 1s4d	^{1}P - ^{1}D	OVII	82.1	15.1	1s4d - 1s5p	^{1}D - ^{1}P
NVI	50.1	24.7	1s3p - 1s4d	^{3}P - ^{3}D	OVII	82.9	14.9	1s4f - 1s5d	^{1}F - ^{1}D
NVI	50.9	24.3	1s3p - 1s4s	^{3}P - ^{3}S	OVII	83.0	14.9	1s4p - 1s5s	^{1}P - ^{1}S
NVI	52.0	23.8	1s3d - 1s4f	^{3}D - ^{3}F	OVII	83.0	14.9	1s4f - 1s5g	^{1}F - ^{1}G
OVI	52.0	23.8	1s^{2}3d - 1s^{2}4f	^{2}D - ^{2}F	OVII	83.0	14.9	1s4f - 1s5g	^{3}F - ^{1}G
CVI	52.0	23.8	3s - 4p	^{1}S - ^{1}P	OVII	83.0	14.9	1s4d - 1s5f	^{3}D - ^{3}F
CVI	52.1	23.8	3p - 4d	^{1}P - ^{1}D	OVII	83.0	14.9	1s4d - 1s5f	^{1}D - ^{1}F
CVI	52.1	23.8	3d - 4f	^{1}D - ^{1}F	OVII	83.2	14.9	1s4p - 1s5d	^{1}P - ^{1}D
CVI	52.1	23.8	3p - 4s	^{1}P - ^{1}S	OVII	83.3	14.9	1s4p - 1s5s	^{3}D - ^{3}S
CVI	52.1	23.8	3d - 4p	^{1}D - ^{1}P	OVII	83.9	14.8	1s4d - 1s5p	^{3}D - ^{3}P
NVI	52.5	23.6	1s3p - 1s4s	^{1}P - ^{1}S	OVI	103.4	12.0	1s^{2}2s - 1s^{2}2p	^{2}S - ^{2}P
NVI	52.9	23.4	1s3d - 1s4p	^{1}D - ^{1}P	NV	123.9	10.0	1s^{2}2s - 1s^{2}2p	^{2}S - ^{2}P
NVI	52.9	23.4	1s3d - 1s4p	^{3}D - ^{3}P	OVII	163.0	7.6	1s2s - 1s2p	^{3}S - ^{3}P
OVI	53.0	23.3	1s^{2}3d - 1s^{2}4p	^{2}D - ^{2}P	NVI	189.7	6.5	1s2s - 1s2p	^{3}S - ^{3}P
OVI	53.6	23.1	1s^{2}3p - 1s^{2}4s	^{2}P - ^{2}S	CV	227.5	5.4	1s2s - 1s2p	^{3}S - ^{3}P

Table D.2: Transitions included in the slow solar wind model

Ion	λ (nm)	E (ev)	Transition	Multiplet	Ion	λ (nm)	E (ev)	Transition	Multiplet
OVII	1.7	715.3	1s^2 - 1s 5p	^{1}S - ^{1}P	CVI	13.5	91.7	2p - 4s	^{1}P - ^{1}S
OVII	1.8	696.5	1s^2 - 1s 4p	^{1}S - ^{1}P	CVI	13.5	91.7	2s - 4p	^{1}S - ^{1}P
OVII	1.9	664.4	1s^2 - 1s 3p	^{1}S - ^{1}P	CVI	13.5	91.7	2p - 4d	^{1}P - ^{1}D
OVII	2.2	572.9	1s^2 - 1s 2p	^{1}S - ^{1}P	NVI	13.7	90.6	1s 2p - 1s 4d	^{1}P - ^{1}D
OVII	2.2	567.7	1s 1s - 1s 2p	^{1}S - ^{3}P	OVI	15.0	82.5	1s^2 2s - 1s^2 3p	^{2}S - ^{2}P
OVII	2.2	560.0	1s 1s - 1s 2s	^{1}S - ^{3}S	NVI	16.1	76.9	1s 2s - 1s 3p	^{3}S - ^{3}P
NVI	2.4	520.6	1s^2 - 1s 4p	^{1}S - ^{1}P	NVI	16.1	76.8	1s 2s - 1s 3p	^{1}S - ^{1}P
NVI	2.5	497.0	1s^2 - 1s 3p	^{1}S - ^{1}P	NV	16.3	75.9	1s^2 2s - 1s^2 4p	^{2}S - ^{2}P
CVI	2.7	458.5	1s - 4p	^{1}S - ^{1}P	OVI	17.3	71.5	1s^2 2p - 1s^2 3d	^{2}P - ^{2}D
CVI	2.8	434.7	1s - 3p	^{1}S - ^{1}P	CV	17.3	71.4	1s 2s - 1s 4p	^{3}S - ^{3}P
NVI	2.9	429.9	1s^2 - 1s 2p	^{1}S - ^{1}P	NVI	17.4	71.1	1s 2p - 1s 3d	^{3}P - ^{3}D
NVI	2.9	425.3	1s 1s - 1s 2p	^{1}S - ^{3}P	NVI	18.1	68.5	1s 2p - 1s 3s	^{1}P - ^{1}S
NVI	3.0	419.5	1s 1s - 1s 2s	^{1}S - ^{3}S	NVI	18.1	68.4	1s 2p - 1s 3s	^{3}P - ^{3}S
CV	3.3	370.2	1s^2 - 1s 4p	^{1}S - ^{3}P	CVI	18.2	68.0	2s - 3p	^{1}S - ^{1}P
CVI	3.4	366.8	1s - 2p	^{1}S - ^{1}P	CVI	18.2	67.9	2p - 3d	^{1}P - ^{1}D
CV	3.5	353.9	1s^2 - 1s 3p	^{1}S - ^{3}P	CVI	18.2	67.9	2p - 3s	^{1}P - ^{1}S
CV	4.0	307.3	1s^2 - 1s 2p	^{1}S - ^{3}P	OVI	18.4	67.3	1s^2 2p - 1s^2 3s	^{2}P - ^{2}S
CV	4.1	304.1	1s^2 - 1s 2p	^{1}S - ^{3}P	NVI	18.5	66.9	1s 2p - 1s 3d	^{1}P - ^{1}D
CV	4.1	298.4	1s^2 - 1s 2s	^{1}S - ^{3}S	NV	18.6	66.5	1s^2 2p - 1s^2 4d	^{2}P - ^{2}D
OVII	8.2	151.1	1s 2s - 1s 5p	^{3}S - ^{3}P	CV	18.6	66.4	1s 2s - 1s 4p	^{1}S - ^{1}P
OVII	8.6	143.9	1s 2s - 1s 5p	^{1}S - ^{1}P	CV	18.7	66.3	1s 2p - 1s 4d	^{3}P - ^{3}D
OVII	8.6	143.7	1s 2p - 1s 5d	^{3}P - ^{3}D	CV	18.9	65.4	1s 2p - 1s 4s	^{3}P - ^{3}S
OVII	8.6	143.6	1s 2p - 1s 5s	^{3}P - ^{3}S	CV	18.9	65.4	1s 2p - 1s 4s	^{1}P - ^{1}S
OVII	8.7	142.2	1s 2p - 1s 5s	^{1}P - ^{1}S	CV	18.9	65.4	1s 2p - 1s 4d	^{1}P - ^{1}D
OVII	8.9	139.0	1s 2p - 1s 5d	^{1}P - ^{1}D	NV	19.0	65.1	1s^2 2p - 1s^2 4s	^{2}P - ^{2}S
OVII	9.1	135.9	1s 2s - 1s 4p	^{3}S - ^{3}P	NV	20.9	59.2	1s^2 2s - 1s^2 3p	^{2}S - ^{2}P
OVII	9.1	135.9	1s 2s - 1s 4p	^{1}S - ^{1}P	CV	22.7	54.5	1s 2s - 1s 3p	^{3}S - ^{3}P
OVII	9.6	128.7	1s 2p - 1s 4d	^{3}P - ^{3}D	OVII	24.6	50.3	1s 3s - 1s 5p	^{3}S - ^{3}P
OVII	9.7	127.5	1s 2p - 1s 4s	^{3}P - ^{3}S	CV	24.7	50.0	1s 2s - 1s 3p	^{1}S - ^{1}P
OVII	9.7	127.5	1s 2p - 1s 4s	^{1}P - ^{1}S	NV	24.8	49.9	1s^2 2p - 1s^2 3d	^{2}P - ^{2}D
OVII	10.0	123.4	1s 2p - 1s 4d	^{1}P - ^{1}D	CV	24.9	49.8	1s 2p - 1s 3d	^{3}P - ^{3}D
OVII	11.4	108.3	1s 3p - 1s 3d	^{3}P - ^{3}D	OVII	25.5	48.5	1s 3s - 1s 5p	^{1}S - ^{1}P
OVI	11.6	106.7	1s^2 2s - 1s^2 4p	^{2}S - ^{2}P	OVII	25.5	48.5	1s 3d - 1s 5p	^{1}D - ^{1}P
OVII	12.0	102.8	1s 2s - 1s 3p	^{3}S - ^{3}P	OVII	25.5	48.5	1s 3p - 1s 5d	^{3}P - ^{3}D
OVII	12.0	102.8	1s 2s - 1s 3p	^{1}S - ^{1}P	OVII	25.6	48.3	1s 3p - 1s 5s	^{3}P - ^{3}S
NVI	12.2	101.4	1s 2s - 1s 4p	^{3}S - ^{3}P	HeII	25.6	48.3	1s - 3p	^{1}S - ^{1}S
NVI	12.2	101.1	1s 2s - 1s 4p	^{1}S - ^{1}P	CV	26.0	47.6	1s 2p - 1s 3s	^{3}P - ^{3}S
OVII	12.8	96.3	1s 2p - 1s 3d	^{1}P - ^{1}D	CV	26.0	47.6	1s 2p - 1s 3s	^{1}P - ^{1}S
OVII	12.8	96.3	1s 2p - 1s 3d	^{3}P - ^{3}D	OVII	26.1	47.4	1s 3d - 1s 5f	^{3}D - ^{3}F
NVI	13.0	95.2	1s 2p - 1s 4d	^{3}P - ^{3}D	OVII	26.2	47.3	1s 3d - 1s 5f	^{1}D - ^{1}F
OVI	13.0	95.2	1s^2 2p - 1s^2 4d	^{2}P - ^{2}D	OVII	26.2	47.2	1s 3p - 1s 5s	^{1}P - ^{1}S
NVI	13.1	94.5	1s 2p - 1s 4s	^{3}P - ^{3}S	OVII	26.2	47.2	1s 3d - 1s 5p	^{3}D - ^{3}P
NVI	13.2	93.8	1s 2p - 1s 4s	^{1}P - ^{1}S	OVII	26.3	47.1	1s 3p - 1s 5d	^{1}P - ^{1}D
OVI	13.2	93.8	1s^2 2p - 1s^2 4s	^{2}P - ^{2}S	NV	26.6	46.5	1s^2 2p - 1s^2 3s	^{2}P - ^{2}S
OVII	13.3	93.2	1s 2p - 1s 3s	^{1}P - ^{1}S	CV	26.7	46.3	1s 2p - 1s 3d	^{1}P - ^{1}D
OVII	13.3	93.2	1s 2p - 1s 3s	^{3}P - ^{3}S	HeII	30.4	40.7	1s - 2p	^{1}S - ^{1}P

continued on the next page

Table D.3: Transitions included in the fast solar wind model

continued from the previous page

Ion	λ (nm)	E (ev)	Transition	Multiplet	Ion	λ (nm)	E (ev)	Transition	Multiplet
OVII	35.2	35.1	1s3s - 1s4p	^{1}S - ^{1}P	CV	67.2	18.4	1s3s - 1s4p	^{3}S - ^{3}P
OVII	35.2	35.1	1s3s - 1s4p	^{3}S - ^{3}P	CV	67.2	18.4	1s3s - 1s4p	^{1}S - ^{1}P
OVI	35.5	34.9	1s^{2}3d - 1s^{2}5f	^{2}D - ^{2}F	NV	71.4	17.3	1s^2 3p - 1s^{2}4d	^{2}P - ^{2}D
OVII	37.0	33.5	1s3p - 1s4d	^{3}P - ^{3}D	CV	71.7	17.2	1s3p - 1s4d	^{3}P - ^{3}D
OVII	38.2	32.4	1s3d - 1s4f	^{3}D - ^{3}F	CV	74.7	16.6	1s3d - 1s4f	^{1}D - ^{1}F
OVII	38.3	32.3	1s3d - 1s4f	^{1}D - ^{1}F	NV	74.8	16.5	1s^2 3d - 1s^{2}4f	^{2}D - ^{2}F
OVII	38.4	32.3	1s3p - 1s4s	^{1}P - ^{1}S	CV	74.9	16.5	1s3d - 1s4f	^{3}D - ^{3}F
OVII	38.4	32.3	1s3p - 1s4s	^{3}P - ^{3}S	CV	75.7	16.3	1s3p - 1s4s	^{3}P - ^{3}S
OVII	38.7	31.9	1s3d - 1s4p	^{1}D - ^{1}P	CV	76.2	16.2	1s3p - 1s4d	^{1}P - ^{1}D
OVII	38.7	31.9	1s3d - 1s4p	^{3}D - ^{3}P	CV	76.3	16.2	1s3d - 1s4p	^{3}D - ^{3}P
OVII	38.7	31.9	1s3p - 1s4d	^{1}P - ^{1}D	NV	76.5	16.2	1s^{2}3d - 1s^{2}4p	^{2}D - ^{2}P
OVI	44.8	27.6	1s^{2}3s - 1s^{2}4p	^{2}S - ^{2}P	OVII	77.5	16.0	1s4s - 1s5p	^{3}S - ^{3}P
NVI	47.4	26.1	1s3s - 1s4p	^{3}S - ^{3}P	NV	77.8	15.9	1s^{2}3p - 1s^{2}4s	^{2}P - ^{2}S
NVI	49.8	24.9	1s3s - 1s4p	^{1}S - ^{1}P	OVII	79.7	15.5	1s4s - 1s5p	^{1}S - ^{1}P
OVI	49.8	24.8	1s^{2}3p - 1s^{2}4d	^{2}P - ^{2}D	OVII	80.1	15.5	1s4p - 1s5d	^{3}P - ^{3}D
NVI	50.1	24.7	1s3p - 1s4d	^{1}P - ^{1}D	OVII	82.0	15.1	1s4f - 1s5d	^{3}F - ^{3}D
NVI	50.1	24.7	1s3p - 1s4d	^{3}P - ^{3}D	OVII	82.1	15.1	1s4d - 1s5p	^{1}D - ^{1}P
NVI	50.9	24.3	1s3p - 1s4s	^{3}P - ^{3}S	OVII	82.9	14.9	1s4f - 1s5d	^{1}F - ^{1}D
NVI	52.0	23.8	1s3d - 1s4f	^{3}D - ^{3}F	OVII	83.0	14.9	1s4p - 1s5s	^{1}P - ^{1}S
OVI	52.0	23.8	1s^{2}3d - 1s^{2}4f	^{2}D - ^{2}F	OVII	83.0	14.9	1s4f - 1s5g	^{1}F - ^{1}G
CVI	52.0	23.8	3s - 4p	^{1}S - ^{1}P	OVII	83.0	14.9	1s4f - 1s5g	^{3}F - ^{3}G
CVI	52.1	23.8	3p - 4d	^{1}P - ^{1}D	OVII	83.0	14.9	1s4d - 1s5f	^{3}F - ^{3}F
CVI	52.1	23.8	3d - 4f	^{1}D - ^{1}F	OVII	83.0	14.9	1s4d - 1s5f	^{1}D - ^{1}F
CVI	52.1	23.8	3p - 4s	^{1}P - ^{1}S	OVII	83.2	14.9	1s4p - 1s5d	^{1}P - ^{1}D
CVI	52.1	23.8	3d - 4p	^{1}D - ^{1}P	OVII	83.3	14.9	1s4p - 1s5s	^{3}P - ^{3}S
NVI	52.5	23.6	1s3p - 1s4s	^{1}P - ^{1}S	OVII	83.9	14.8	1s4d - 1s5p	^{3}D - ^{3}P
NVI	52.9	23.4	1s3d - 1s4p	^{1}D - ^{1}P	OVI	103.4	12.0	1s^{2}2s - 1s^{2}2p	^{2}S - ^{2}P
NVI	52.9	23.4	1s3d - 1s4p	^{3}D - ^{3}P	OVI	112.2	11.0	1s^{2}4d - 1s^{2}5f	^{2}D - ^{2}F
OVI	53.0	23.3	1s^{2}3d - 1s^{2}4p	^{2}D - ^{2}P	NV	123.9	10.0	1s^{2}2s - 1s^{2}2p	^{2}S - ^{2}P
OVI	53.6	23.1	1s^{2}3p - 1s^{2}4s	^{2}P - ^{2}S	OVII	163.0	7.6	1s2s - 1s2p	^{3}S - ^{3}P
HeI	58.4	21.2	1s^2 - 1s2p	^{1}S - ^{1}P	NVI	189.7	6.5	1s2s - 1s2p	^{3}S - ^{3}P
NV	62.9	19.7	1s^{2}3s - 1s^{2}4p	^{2}S - ^{2}P	CV	227.5	5.4	1s2s - 1s2p	^{3}S - ^{3}P
CV	65.5	18.9	1s3p - 1s4s	^{1}P - ^{1}S	OVII	593.5	2.1	1s3s - 1s3p	^{3}S - ^{3}P
CV	67.0	18.5	1s3d - 1s4p	^{1}D - ^{1}P					

Table D.4: Transitions included in the fast solar wind model

Dankwoord

Dit werk kon alleen tot stand komen dankzij de hulp en steun van een groot aantal personen. Deze mensen wil ik hier graag bedanken. In de eerste plaats wil ik Ronnie Hoekstra bedanken voor zijn enthousiasme en voor het onderwerp van mijn afstudeeronderzoek, dat mij zodanig in zijn ban heeft gekregen dat ik met plezier begin aan een promotie-onderzoek op hetzelfde onderwerp. Ook wil ik hem, en natuurlijk Reinhard Morgenstern bedanken voor de mogelijkheden die ze mij gegeven hebben kennis te maken met de Atoomfysica.

De andere belangrijke persoon achter mijn onderzoek was Xander Tielens. In de eerste plaats wil ik Xander bedanken voor zijn steun bij het opzetten van het onderzoek. Door een brede interesse te combineren met een kritische geest wist je mij steeds te verrassen met mijn eigen onderzoek, en ik hoop dat ik ook de komende jaren nog op deze frisse blik kan blijven rekenen.

Zoltán Juhász bedanken voor de samenwerking en alle discussies over kometen en ionen.

Verder wil ik graag iedereen van de Atoomfysica groep bedanken voor alle steun, adviezen en de leuke tijd die ik gehad heb: Abel, Steven, Mirko, Danyal, Annemieke, Jur, Thomas, Steven en Carolijn bedankt!

Twee mensen met wie ik niet direct heb samengewerkt, maar aan wie ik toch grote dank verschuldigd ben wil ik hier graag noemen: Peter van der Straten, voor de posterprijs op de NNV bijeenkomst te Lunteren; ik heb dit ervaren als een grote stimulans! Hetzelfde geldt voor Ewine van Dishoeck; ik wil haar graag bedanken voor de mogelijkheid de Oort-conferentie bij te wonen.

Mijn ouders wil ik bedanken voor de mogelijkheid die ze mij hebben geboden om te studeren. En bovenal wil ik Jenny noemen, dank je wel voor al je geduld en steun!